Electromagnetic interactions in one-dimensional metamaterials

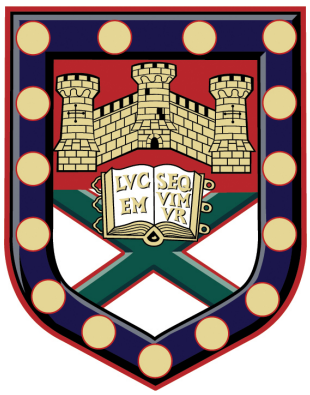

Sathya Sai Seetharaman

School of Physics

University of Exeter

A thesis submitted for the degree of

Doctor of Philosophy

June 2018

Electromagnetic interactions in one-dimensional metamaterials

Submitted by Sathya Sai Seetharaman to the University of Exeter as a thesis for the degree of Doctor of Philosophy in Physics
2018

I certify that all material in this thesis which is not my own work has been identified and that no material has previously been submitted and approved for the award of a degree by this or any other University.

Sathya Sai Seetharaman
2018

I acknowledge financial support from the Engineering and Physical Sciences Research Council (EPSRC) of the United Kingdom, via the EPSRC Centre for Doctoral Training in Metamaterials (Grant No. EP/L015331/1).

All data created during this research are available from the University of Exeters institutional repository at https://doi.org/10.24378/exe.630

Point of contact for any queries on the thesis/data and relevant code/software is Prof. William L. Barnes, email: w.l.barnes@exeter.ac.uk

To my beloved wife Nithya and my wonderful parents

Acknowledgements

My time working at the Electromagnetics and Acoustics Group at Exeter has been filled with excitement, enjoyment and enlightenment. I would like to take this opportunity to express my deepest gratitude to some very important people who have shaped the course of my journey.

Firstly, I'd like to thank my supervisors Prof. Bill Barnes and Dr. Ian Hooper, who have constantly guided me with their patience and encouragement. I sincerely thank them for pushing me to be my best and helping me be a good physicist. I would also like to thank Prof. Roy Sambles, whose useful feedback and continued motivation have always helped me better myself. I definitely need to thank Prof. Alastair Hibbins and Dr. Simon Horsley, whose comments on my work from time to time have helped my progress. I cannot thank the mechanical workshop technicians Nick, Peter and Paul enough for always ensuring that I had my samples delivered on time and at the best quality. And thanks to the Engineering and Physical Sciences Research Council for the PhD studentship, and to DARO (University of Exeter) and the CDT management for my scholarship, without all of which this PhD would have never happened.

Next, my thanks go to my friends - Erick, Gloria, Lauren, Adolfo, Chris, Alba, Sergio, Sam, Miguel, Santi, Jayesh, Henry, Connie, and Kishan who have shown me that life should be lived a day at a time and any day is good for a party! I thank them all for many insightful and soulful conversations without which I would have completed my thesis a month earlier but would have been a dull individual. I am eternally grateful to my landlords Peter and Dorinda for the warmth, love, all the cuppas and their timely wisdom.

Words cannot describe how thankful I am to my beloved wife Nithya, who has been my pillar of support, my motivator, my counsellor, my better half, my best friend, and without whom I wouldn't be the person I am. Last but not the least, I bow down with respect and gratitude before my beloved parents for nurturing me, educating me and teaching me how to walk in the world.

Abstract

Metamaterials offer the freedom to tune the rich electromagnetic coupling between the constituent meta-atoms to tailor their collective electromagnetic response. Therefore, a comprehensive understanding of the nature of electromagnetic interactions between meta-atoms is necessary for novel metamaterial design, which is provided in the first part of this thesis. The subsequent work in the thesis applies the understanding from the first part to design and demonstrate novel one-dimensional metamaterials that overcome the limitations of metamaterials proposed in literature or exhibit electromagnetic responses not previously observed.

Split-ring Resonators (SRRs) are a fundamental building block of many electromagnetic metamaterials. In the first part of the work in this thesis, it is shown that bianisotropic SRRs (with magneto-electric cross-polarisation) when in close proximity to each other, exhibit a rich coupling that involves both electric and magnetic interactions. The strength and nature of the coupling between two identical SRRs are studied experimentally and computationally as a function of their separation and relative orientation. The electric and magnetic couplings are characterised and it is found that, when SRRs are close enough to be in each other's near-field, the electric and magnetic couplings may either reinforce each other or act in opposition. At larger separations retardation effects become important.

The findings on the electromagnetic interactions between bianisotropic resonators are next applied to developing a one-dimensional ultra-wideband backward-wave metamaterial waveguide. The key concept on which the metamaterial waveguide is built is electro-inductive wave propagation, which has emerged as an attractive solution for designing backward-wave supporting metamaterials. Stacked metasurfaces etched with complementary SRRs (CSRRs) have also been shown to exhibit a broadband negative dispersion. It is demonstrated through experiment and numerical modeling, that the operational bandwidth of a CSRR metamaterial waveguide can be improved by restricting the cross-polarisation effects in the constituent meta-atoms. The metamaterial waveguide constructed using the modified non-bianisotropic CSRRs are found to have a fractional bandwidth of 56.3% which, based on a thorough search of relevant literature, is the broadest reported value for an electro-inductive metamaterial. A traditional coupled-dipole toy-model is presented as a tool to understand the field interactions in CSRR based

metamaterials, and to explain the origin of their negative dispersion response. This metamaterial waveguide should be of assistance in the design of broadband backward-wave metamaterial devices, with enhanced electro-inductive waveguiding effects.

In the final part of the thesis, a one-dimensional metamaterial prototype that permits simultaneous forward- and backward-wave propagation is designed. Such a metamaterial waveguide could act as a microwave analogue of nanoparticle chains that support electromagnetic energy transfer with a positive or a negative dispersion due to the excitation of their longitudinal or transverse dipole modes. The symmetry of the designed hybrid meta-atom permits the co-existence of two non-interfering resonances closely separated in frequency. It is experimentally and computationally shown that the metamaterial waveguide supports simultaneous non-interacting forward- and backward-wave propagation in an overlapping frequency band. The proposed metamaterial design should be suitable for realising bidirectional wireless power transfer applications.

Contents

List of Figures

Chapter 1

Introduction

Since the inception of the field of 'metamaterials', extensive research has revealed that their tailored electromagnetic responses are acquired from the precise geometric shape, size, and relative arrangement of their 'meta-atoms', which influence the electromagnetic interactions among the meta-atoms. The strength of this interaction can be tuned by changing the separation and the relative orientation between the meta-atoms. However, a full characterisation of the nature of electromagnetic coupling between meta-atoms as a function of both relative orientation and separation had yet to be performed.

One of the objectives of this thesis is to provide a better understanding of electromagnetic interactions between meta-atoms in microwave metamaterials, by using experimental findings validated through analytical and numerical models, and toy coupled-dipole models, as required. Such a complete characterisation would be a valuable asset to researchers designing metamaterials.

A simple coupled-dipole approach is employed for qualitative prediction and understanding of the nature of electromagnetic interactions between meta-atoms, and the numerical modelling tool for accurate quantitative determination of strength of the resonant modes resulting from the meta-atom interactions. The main goal of the thesis is then to apply the understanding gained from the meta-atom coupling study to design, analyse and demonstrate one-dimensional metamaterial systems that either improve over the limitations of similar systems proposed in literature or are the first of their kind.

1.1 Thesis outline

The contents of this thesis can be divided into three sections. The first section (chapters 2 and 3) introduces the theoretical background along with the experimental and modelling methods used in the thesis, necessary to understand the work undertaken in the subsequent chapters. The second section (chapter 4) lays the experimental groundwork in understanding the nature of electromagnetic coupling in bianisotropic split-ring resonators, on which the rest of the thesis is built. The third and final section (chapters 5 and 6) present the one-dimensional metamaterial designs for novel applications such as magneto- and electro-inductive waveguides, and power transfer devices.

Chapter 2 furnishes the historical developments in electromagnetics research that led to the inception of the field called 'Metamaterials'. The literature containing works on the electromagnetic coupling between split-ring resonator (SRR) meta-atoms in several relative orientations are reviewed and the findings summarised. The key concepts of magneto-inductive (MI) coupling between split-rings, complementary resonators along with the so-named electro-inductive (EI) coupling between them, are introduced. The theoretical dispersion relations of the MI and EI wave propagation in one-dimension is presented and reviewed. These dispersion relations are compared to those of one-dimensional coupled dipole chains in order to draw a parallelism between the concepts.

A detailed overview of the fabrication techniques used to make the microwave metamaterials are presented in chapter 3. The theoretical working mechanism of the experimental equipment such as the Vector Network Analyzer (VNA), coaxial antennas, and the rectangular waveguide used for experimental metamaterial characterisation are elaborated. The second half of the chapter presents the features and boundary conditions used in the finite element numerical modelling technique, and the derivation of necessary analytical formulation that are used in chapter 4 to characterise the electromagnetic interactions in a coupled SRR dimer.

The SRRs being one of the popular meta-atoms of choice to construct metamaterials are chosen as the prime candidate of study for chapter 4. A basic bianisotropic single-ring design is chosen. A single SRR is characterised in a rectangular waveguide at different orientations with respect to the electromagnetic propagating mode of the waveguide, so as to understand its resonant response and outline the physical limitations imposed by the waveguide. Two identical SRRs are then placed in the waveguide, with their scattered signals (reflection and transmission) recorded as a function of changing relative orientation and separation between them. The analytical model formulated in

chapter 3 is used to compute the resonance frequencies of the SRR dimer to validate the experimental results and the electric and magnetic coupling coefficients to show how the coupling strength of each type of interaction is tuned as a function of changing parameters.

In chapter 5, a specific example of a stacked complementary SRR (CSRR) design is used to demonstrate that the presence of cross-polarisation effects in CSRR meta-atoms can influence the inter-element coupling in the same way it does in regular SRRs. A design modification is suggested to enforce non-bianisotropy through symmetry. A one-dimensional metamaterial waveguide, constructed by stacking the non-bianisotropic CSRR meta-atoms is characterised and its performance compared with that of a similar 1D stacked metamaterial waveguide with bianisotropic CSRR meta-atoms. In the last section, further investigation on the sensitivities of the two metamaterial waveguides to changing longitudinal periodicity are numerically analysed.

Chapter 6 presents the results of an interesting challenge - to design a metamaterial waveguide that supports both positive and negative dispersing resonant modes in an overlapping frequency band, without having to change the lattice parameters of the metamaterial. A hybrid meta-atom design is presented, which is then used to construct a 1D metamaterial waveguide with non-interfering counter-propagating inductive modes.

In the concluding chapter (chapter 7), the summary of findings from all prior chapters is presented, with possible applications of the proposed metamaterial structures and future directions of the work.

Chapter 2

Background

2.1 Introduction

The term 'Metamaterials' comes from the combination of the Greek word 'meta' meaning beyond, and the word 'materials'. Metamaterials are structured or artificially designed to manipulate waves such as electromagnetic and sound waves. They offer a range of extraordinary properties that are beyond what is available from naturally occurring bulk materials, which has opened the door to many novel applications. Their tailored properties are derived from two important features 1) the inherent response of the individual 'meta-atoms' which constitute the material (just as naturally occurring materials that derive their properties from their constituent atoms), and 2) the specific periodic or aperiodic arrangement of these atoms in a lattice.

'Meta-atoms' are the artificial atoms/molecules that can be designed to shape the collective electromagnetic (or acoustic) response of the metamaterial. The dimensions of the atoms and the lattice separation between individual atoms are in general sub-wavelength, such that an incident electromagnetic wave experiences a homogeneous continuous medium with its own effective material parameters. However, it should be noted that the term metamaterial is frequently used to denote materials in which the meta-atoms are of comparable sizes to the wavelength of the incident electromagnetic wave and where the electromagnetic interactions between the meta-atoms play a key role in determining the metamaterial's response. Before reviewing some of the recent research in the field of metamaterials, a brief historical perspective of the research that played a pivotal role in the development of metamaterials is presented.

2.2 A historical perspective of metamaterials

Electromagnetic waves were initially used as a probe to study the properties of crystals in the 1800s and early 1900s, which resulted in valuable knowledge of the properties of both the materials and the electromagnetic waves. This knowledge of wave-matter interactions has been the basis for the development of a huge number of applications too numerous to mention, ranging from display technologies to the internet, from radio communication to Global Positioning Systems (GPS). The knowledge that the electric response of a material can be altered by periodically including or substituting new atoms in a host material may have existed beforehand, but the first of the works that applied this knowledge for commercial use was the intentional doping of semiconductors to alter their electrical properties [1]. This is one of the notable examples of the creation of a material with a previously unknown or unavailable response by combining two materials with drastically different properties.

The journey of electromagnetics research towards the development of metamaterials began more than a century ago. In the early 1900s, when it was popular practice to visualise wave phenomena through mechanical arrangements, Lamb [2] and Pocklington [3] observed the wave propagation in simple one-dimensional systems such as a long straight wire under the influence of a longitudinal force/thrust and even a stretched out bicycle chain. Their research objective was to investigate the possibility of negative group velocity. Their theoretical and experimental work along with Schuster's work in [4], showed that when the group velocity and the phase velocity have opposite signs in a medium (when the medium is capable of sustaining backward waves), light incident on the medium refracts negatively. Interestingly, they explored this possibility only out of interest but were "doubtful" if the concept of a negative group velocity would serve any application.

Much later, in 1968, Veselago published his detailed work on the study of wave propagation in a medium with a negative refractive index [5]. He identified that in a material with simultaneously negative values of dielectric permittivity and magnetic permeability ($\epsilon < 0,\ \mu < 0$) and hence a negative refractive index, the electric ($\mathbf{E}$), magnetic ($\mathbf{H}$) and the wave ($\mathbf{k}$) vectors of an electromagnetic wave all formed a left-handed triplet. Therefore, the group and phase velocities were directed oppositely. This is the reason that the negative index materials (NIMs) also popularly came to be known as left-handed media (LHM) or backward-wave media. Veselago found that in such a medium, an incident electromagnetic wave would refract negatively, resulting in the inversion of Snell's law. He also revealed that a NIM slab with parallel edges/surfaces

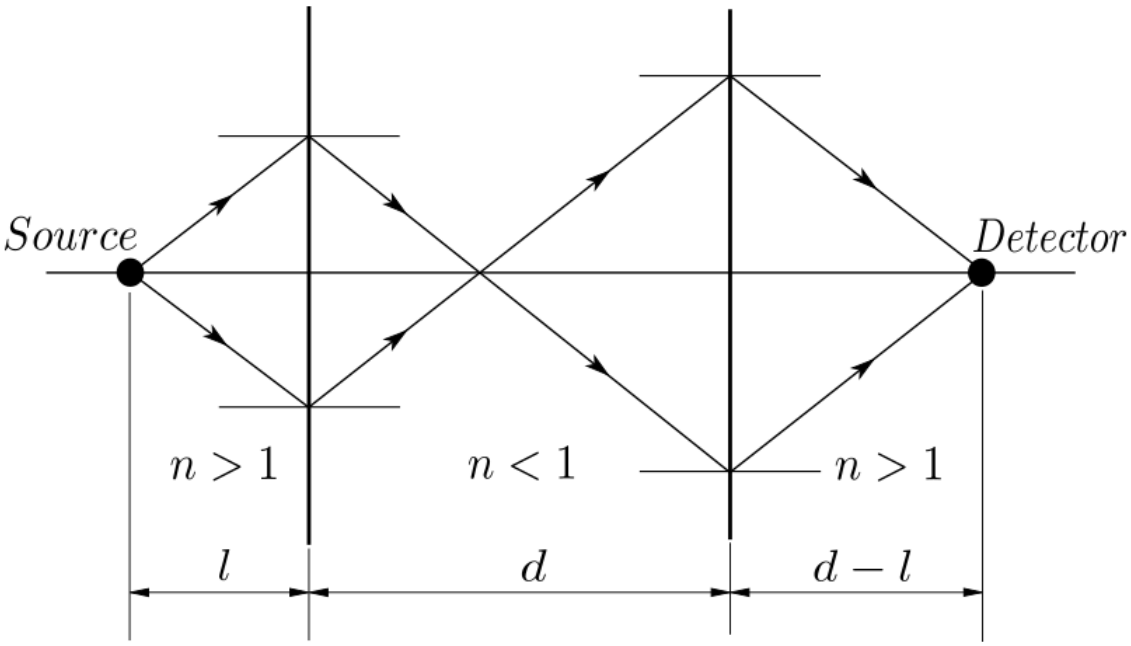

Figure 2.1: A ray-optics representation of how light from a source point is focussed by a thin slab of negative index material, as first suggested in [5].

could focus the radiation from a point source to a point focus, as if it were a lens (see figure 2.1).

Developing a sub-wavelength imaging device had already been a priority, because conventional lenses produced diffraction limited images, as Abbe showed much earlier [6]. Though Veselago's proposal was promising, a NIM did not occur in nature and the challenge was to build one.

In the early 1960s, research had been conducted on an artificial material composite with periodic inclusions of thin resistive metallic wires embedded in a dielectric such as air, to simulate a neutral plasma and study the microwave propagation through the ionosphere (see figure 2.2a) [7, 8]. Such a thin wire array (the plasma) exhibited a negative effective permittivity (ϵ_{eff}) below a plasma frequency, as also shown much later in [9, 10]. A similar artificial material which would exhibit a negative value of effective permeability (μ_{eff}) was not known in the 1960s and 70s.

Meanwhile, a different part of the research community was aiming to develop high frequency sensing devices for Nuclear Magnetic Resonance (NMR) experiments, that take advantage of the magnetic resonances of different atomic nuclei. Quite simply, successful designs from these experiments would be employed to develop Magnetic Res-

onance Imaging (MRI) machines, for medical applications. A unique geometry where slits were added to a cylindrical sample tube allowed the excitation of a magnetic resonance in the tube when the cylinder's axis aligned to a superconducting magnet [11, 12]. This design is a predecessor to the current split-ring resonators. However, this idea was identified and exploited only decades later.

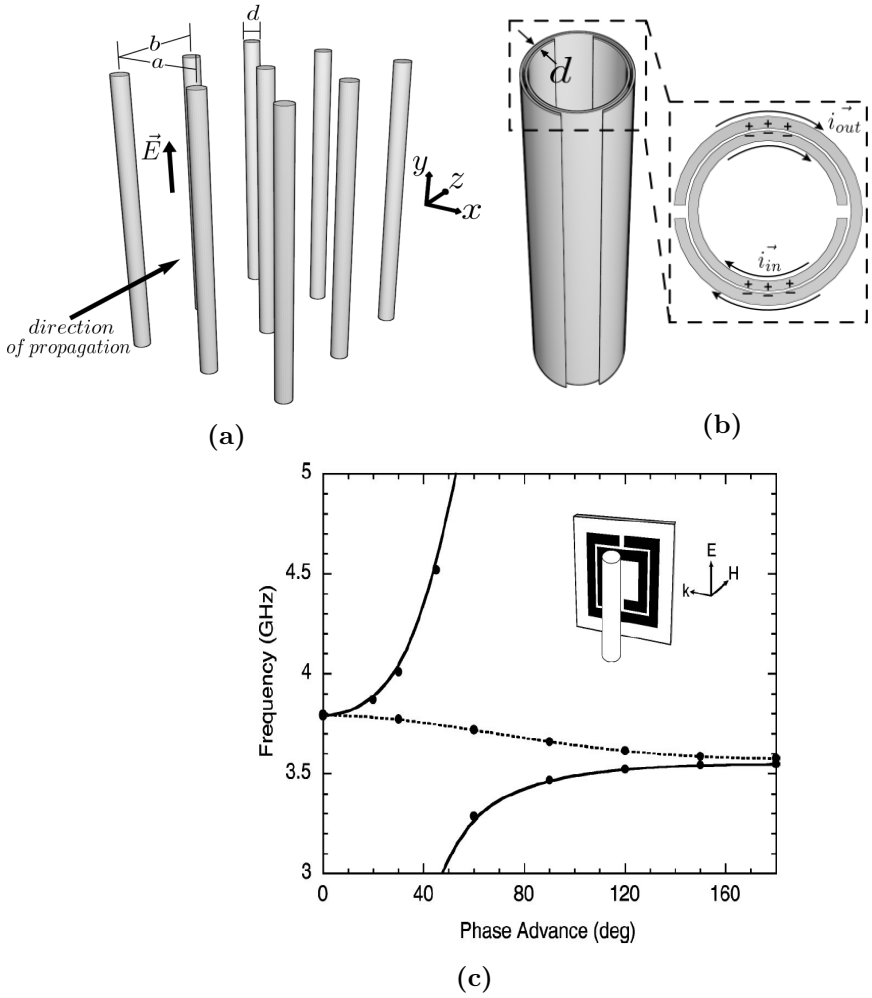

Figure 2.2: (a) Schematic of a wire array illuminated by an electromagnetic wave with electric field polarised along the axis of the wires, (b) 'Split rings' used in the experiments of [13], inset: a split-ring resonator sliced from the cylinder showing instantaneous electric currents and inter-ring capacitive action, (c) The dispersion relation of a SRR-wire composite medium - solid curves show SRR medium's dispersion alone, dashed curves show dispersion of the composite. Inset shows the orientation of a unit cell with respect to the incident electromagnetic wave. (c) has been reused with permission from [14].

Pendry et al. in [13] were studying the magnetic properties of arrays of cylinders

(along the cylinders' axial direction), similar to the ones explored in [7, 8]. The wire array had a very weak effective magnetic response. The challenge was to design an effective medium that would also possess a negative effective magnetic permeability. Pendry shaped each cylinder as two concentric single-split cylinders (called 'split rings'), with the splits positioned on opposite sides. The split-rings exhibited an enhanced effective magnetic permeability (μ_{eff}) close to resonance, especially with negative values just above the resonance. This modification widened the range of magnetic properties achievable by the wire array structure and was a first demonstration of magnetic resonance in the GHz frequency range. The split-ring cylinders height was reduced to make the split-ring resonator (SRR) as seen in figure 2.2b, a planar structure that could easily be fabricated on substrates and arranged either in a plane or as a stack in columns to form three-dimensional metamaterial structures.

It was only a matter of time before periodic arrays of thin wires and SRRs were combined in an interspersed arrangement to produce a negative index material composite, whose unit cell is shown in figure 2.2c [14, 15]. It is noteworthy that the word "metamaterial" first appears in the 2000 work by Smith et al. [14]. The authors in [15] demonstrated that their composite medium exhibited simultaneously negative values of ϵ and μ in a given frequency region. The dispersion curves in figure 2.2c show that where the transmission of electromagnetic waves was prohibited in a frequency region (a stopband) by just the SRR array (solid curves), a passband was shown to be created permitting wave propagation by the SRR-wire combination (dashed curve). These results were validated by further experimental demonstrations of negative refractive index in [16–20].

The dispersion characteristics of the NIMs as obtained by substitution of negative material parameters [14] and using an equivalent circuit approach [21] both revealed the existence of a negative dispersion passband that supports backward propagating waves as predicted by Veselago in [5]. The equivalent circuit modelling of the NIM in [21] further revealed that when the electromagnetic wave propagating in free space and the SRR array were uncoupled (theoretically speaking), the SRR medium on its own could act as a backward-wave medium without a negative index by virtue of the magneto-inductive (MI) coupling between the SRRs. The MI waves were already a familiar concept by then [22, 23]. SRR-based MI wave devices have since paved the way for the emergence of several interesting applications such as magneto-inductive waveguides [23], magneto-inductive lenses for sub-wavelength focussing of electromagnetic radiation [24, 25], and in general as wireless power transfer devices [26]. The theory of magneto-inductive waves will be discussed in section 2.5.

Metamaterials with their tailored electromagnetic responses have laid the foundation for several sub-disciplines like invisibility cloaking through conformal mapping [27–29], superlens to beat the diffraction limit and improve the resolution in imaging [30–36], wireless power transfer applications [22, 23, 26, 37–39], and metamaterial magnetic layered lenses for medical imaging [24, 25]. Several different meta-atom and metamaterial designs have emerged to design NIMs, such as cut-wire pairs [40–42], fish-net/stacked hole array structures [43–48], H-shaped resonators [49], and Ω resonator-wire pair [50], to name a few. It is beyond the scope of this chapter to review every NIM design/configuration. More comprehensive reviews of the chronological development and general research in the area of electromagnetic metamaterials can be found in the review articles in [51–56]. The stacked hole arrays will be discussed briefly in chapter 6, because of their relevance. In the rest of this chapter, a theoretical background on SRR meta-atom design, electromagnetic properties of SRR meta-atoms, and interactions between SRRs with a view to highlight their importance in metamaterial design are provided.

2.3 Design and resonant response of a split-ring resonator

The first step in understanding the collective response of an effective medium is to understand the resonant response of its constituent building blocks - the meta-atoms. In some early approximations, the response of a metamaterial was considered to be that of a bulk-material like medium (or an 'effective medium') with its own effective material parameters. Though this collective response was considered by ignoring inter-element interactions, Gay-Balmaz et al. [57] discovered that the response of a metamaterial consisting of SRRs is not determined solely by the response of the individual resonators, but is also dependent on inter-element interactions, which in turn depend upon the relative arrangement of the elements. The strength and range of this interaction depends on the resonance frequency, lattice spacing and relative geometrical orientations of the elements with respect to one another. The discussion will return to this topic of coupling between resonators, in section 2.5. The design and resonant response of an individual SRR is discussed next.

2.3.1 Approaches to designing a SRR

SRRs were one of the first metamaterial building blocks, the interactions of which were studied widely by researchers. There are still many features in the nature of coupling

in SRRs that are to be understood. The design for the very first SRRs used in metamaterials (shown in figure 2.2b) is credited to the work by Pendry [13], as mentioned in section 2.2. The design can be simplified further by detaching the two rings to make two single-split single SRRs, which are themselves simple harmonic oscillators that have also been widely studied [58–68]. It is meaningful to begin the discussion starting from this elementary design. Figure 2.3a shows a simple schematic of a single-ring SRR with its design parameters marked on it at the appropriate locations. Figure 2.3b shows a single SRR's instantaneous charge and current distributions and the corresponding excited dipole moments at its fundamental resonance.

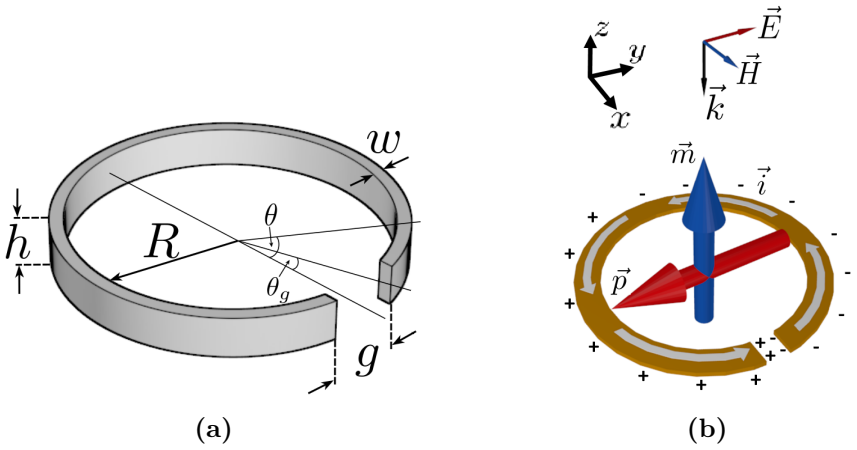

(a) (b)

Figure 2.3: (a) Schematic of a thick SRR analysed in [67]. R is the innner radius of the ring, h and w the height and width of the ring, and g is the height of split-gap. θ refers to the co-ordinate points on the SRR, with θ_g marking the co-ordinates of the split-gap edges. (b) A simple representation of single SRR's electric (red arrow) and magnetic (blue arrow) dipole moments represented at its fundamental resonance. The dipole moments are instantaneous but are not simultaneously at their peak strength. The instantaneous charge and current distributions are also shown.

When the resonator is oriented in such a manner that the split of the ring is perpendicular to the electric field component (as seen in figure 2.3b), a potential difference is created across the split. The electric field map in figure 2.4a shows a high concentration of electric fields across the split-gap, in the SRR's plane. The black arrows show an instantaneous distribution of electric field around the SRR in response to an electromagnetic excitation. The electric field response of the SRR is seen to comprise of the electric field at the split-gap contributing to a gap capacitance, fringing electric fields around the split-gap and between the inner surfaces of the SRR contributing to a surface capacitance. The electric field is zero around the metallic region of the SRR opposite to the split. Despite the strong electric field accumulation closer to the split-

gap of the SRR, for simplicity the collective electric response of the SRR is represented by an in-plane electric dipose moment (red arrow in figure 2.3b), positioned at its centre.

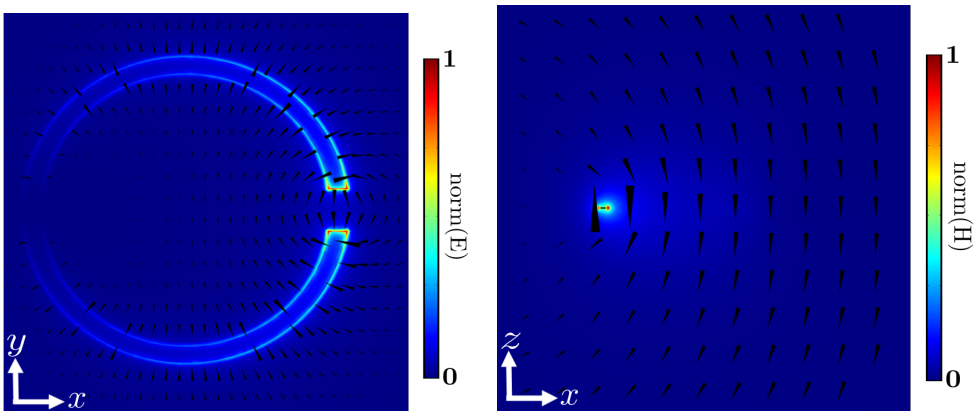

(a) (b)

Figure 2.4: (a) Plane view of the SRR with the colour map showing normalised electric field norm. The black arrow arrow heads are vectors representing the instantaneous electric field distribution on the map. (b) A zx-plane perpendicular to the plane of the SRR and dividing it equally through its split containing a colour map showing normalised magnetic field norm. The black arrow arrow heads are vectors representing the instantaneous magnetic field distribution in the chosen plane.

The presence of the split results in a harmonically changing charge distribution in response to the time-varying electric field of the electromagnetic wave, which induces an oscillating electric current in the SRR corresponding to the ring's resonance frequency. Figure 2.4b shows a colour map of the magnetic field (norm) plotted in an xz-plane with respect to the co-ordinate system chosen in figure 2.3b, dividing the SRR equally through its split. As seen from the colour map, the strength of the magnetic field is the strongest closer to the metallic region of the SRR opposite to the split (left half of figure 2.4b). The black arrows represent instantaneous magnetic field distribution in the chosen plane, with the size of the arrows indicating the field strength. The instantaneous field distribution also shows strong magnetic fields closer to the metallic region of the SRR. Similar to the electric field representation, the collective out-of-plane magnetic field strength of the SRR is represented by an effective out-of-plane magnetic dipole moment (blue arrow in figure 2.3b), at the SRR's centre. The magnetic dipole moment of the SRR can also be directly excited by the magnetic field component of the electromagnetic wave by suitably orienting the SRR. The electric dipole moment will then be indirectly excited due to the charge accumulation in the vicinity of the splits. This property whereby an electric field excites a magnetic response in the SRR and vice-versa is called bianisotropy, and is the subject of discussion in section 2.3.2.

The coupled-dipole approach to understanding electromagnetic coupling in metamaterials cannot be accurately quantitative and is instructive to understand the nature of electromagnetic coupling between meta-atoms. Approaches in literature to analyses 1D dipolar systems is discussed in section 2.4. Discussion on coupled-dipole approach to analyse electromagnetic coupling in a SRR dimer qualitatively is presented in chapter 4.

The equivalent circuit approach has been favoured in literature to design SRRs. The authors in reference [67] have derived an approximate expression for the resonance frequency of the single split-ring structure in figure 2.3a. The single SRR structure is approximated as an LC circuit in the quasi-static limit, with the resonance frequency expressed as,

$$f_0 = \frac{1}{2\pi\sqrt{LC}} \tag{2.1}$$

where L and C are respectively the effective inductance and capacitance of the split-ring. The inductance of the ring was calculated using formulas from [69] treating the split-ring as a single loop of a coil. Capacitance is to be expected in the split-gap due to charge separation, in the inner surface of the SRR, and also around the split-gap due to the fringing fields. The total capacitance of the ring is the sum of the individual capacitance contributions. The formulas for calculating L and C of the SRR are given by,

$$\begin{aligned} L &= \mu_0 R_m \left(\log \frac{8R_m}{h+w} - \frac{1}{2} \right) \\ R_m &= R + w/2 \end{aligned} \tag{2.2}$$

$$\begin{aligned} C_{gap} &= \epsilon_0 \frac{hw}{g} + C_0 \\ C_0 &= \epsilon_0 (h + w + g) \\ C_{surf} &= \frac{2\epsilon_0 (h+w)}{\pi} \log \frac{4R}{g} \\ C_{total} &= C_{gap} + C_{surf} \end{aligned} \tag{2.3}$$

In equations (2.2) and (2.3), μ_0 and ϵ_0 are the permeability and permittivity respectively of free space, R_m is the radius of the ring measured at the centre of the conductor, R is the inner ring radius, h the height of the cylinder, w the width of the

ring, and g the height of the split-gap. C_0 is the correction term to the capacitance due to fringing fields, C_{surf} and C_{gap} the surface and gap capacitances respectively, and C_{total} the total capacitance of the ring. These analytical expressions work well for most values of the ring height h and width w. The authors observe that when the ring width w and and the height h were made small simultaneously so that the resonance wavelength and the circumference of the ring were comparable, the accuracy worsened. These expressions hold well for SRRs with their fundamental resonance in the lower GHz frequencies, and are also good qualitative descriptors that highlight the nature of the capacitive and inductive effects in the SRRs.

The effect of the design parameters on the SRR's resonance can be directly observed by considering the equations (2.2) and (2.3). Any design changes that result in an increase of inductance and/or capacitance of the SRR cause the resonance frequency to reduce, in accordance with equation (2.1). For example, increasing the radius of the SRR increases the effective path length of the electric current and therefore, the resonance wavelength (resonance frequency decreases). Complementing this idea, the radius terms R and R_m can seen to have a direct relationship with both L and C and hence an inverse relationship with the resonance frequency f_0. Similarly, the effect of the width, split-gap and height of the SRR on the resonance frequency can also be understood through their relationship to L and C in equations (2.2) and (2.3). Detailed analysis of the effects of tuning the design parameters on the resonance frequency can be found in [61, 63, 65, 67, 70].

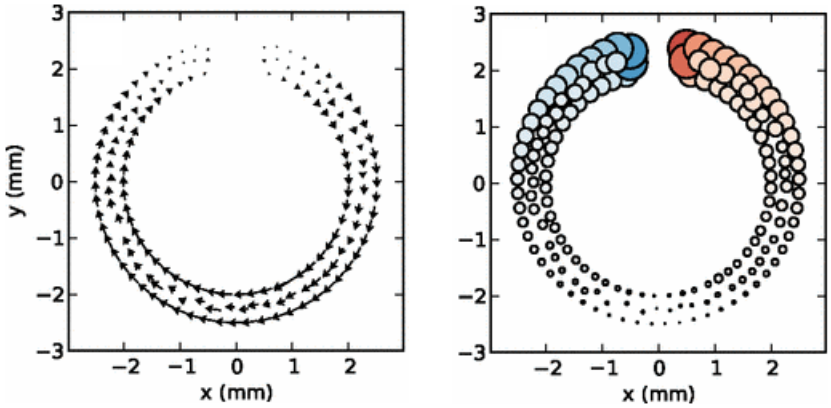

Figure 2.5: Numerically calculated (a) current and (b) charge distribution across an SRR at resonance. Reused with permission from [71].

The equivalent circuit approach is advantageous in designing metamaterial based

devices for engineering applications. Using physical quantities like the resistance, inductance and capacitance of the resonators helps quantify the system's response in terms of characteristic impedance that needs to be matched to couple energy into and out of the device. The equivalent circuit approach helps reduce the metamaterial into a transmission line, which for example, is beneficial to conceptualise and visualise metamaterial waveguides. Another approach to analyse a single SRR or coupled SRRs is in terms of field distributions, determining analytical expressions or numerically computed electric charge and current distributions on them. This approach has an advantage over the equivalent circuit method in that it has better accuracy in accounting for the effect of decaying near-fields of the coupled resonators on the strength of electromagnetic coupling between them, which the circuit model does not include.

The authors in [72] give analytical expressions for the electric charge and current distributions in terms of the design parameters as,

$$\rho_L(\theta) = \frac{h+w}{\pi}\epsilon_0 V_0 \tan\frac{\theta}{2} \quad \text{for} \quad \theta \leq \theta_g \tag{2.4}$$

$$I(\theta) = -i\omega 2R\frac{h+w}{\pi}\epsilon_0 V_0 \ln\left(\frac{cos\frac{\theta_g}{2}}{cos\frac{\theta}{2}}\right) \tag{2.5}$$

where the parameters h, w and R represent the same design parameters as in the previous equations. V_0 is the SRR's input voltage. The parameter θ represents the co-ordinates on the SRR, with $\pm\theta_g$ specifically representing the co-ordinates of the split-gap, as seen in figure 2.3a. The equations satisfy the continuity condition and as per the boundary conditions, show a high magnitude of charge concentration and vanishing electric currents at the splits. A slightly different treatment to the electric current and charge distributions in the single SRR is given in [71], where the charge and current distributions on a single-ring SRR are numerically calculated. Figure 2.5 shows the instantaneous values of the numerically calculated charge and current distributions on a SRR at its resonance [71]. The use of these charge and current distributions in the calculation of coupling coefficients in coupled SRR systems is discussed in section 3.5.2.

Building back to the double-ring SRR [13], a close-up schematic is shown in figure 2.6a. In addition to the capacitance in the splits of the inner and the outer rings, there is an inter-ring capacitance due to the interaction between separated unlike charges of the inner and outer rings, as shown in figure 2.6a. An equivalent circuit model to

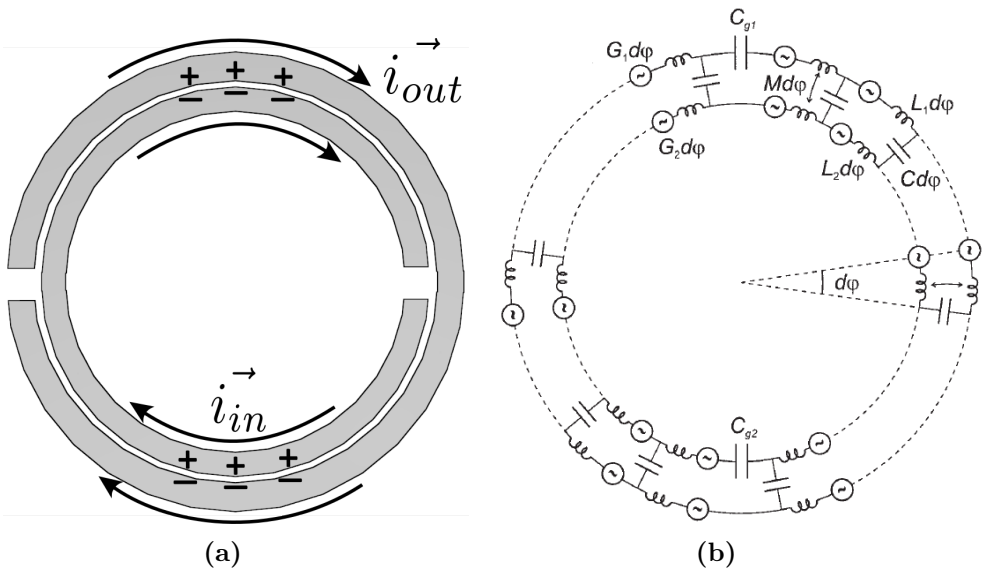

(a) **(b)**

Figure 2.6: (a) A close-up view of the schematic showing a SRR used in [13] with instantaneous electric currents in the inner and the outer rings. Due to the strong inter-ring capacitance, the electric currents in both rings are co-directional. The equivalent circuit representation of the double-ring SRR shown in (a), reused with permission from [73].

compute the resonance frequencies of this double-ring SRR was given by [73], which is shown in figure 2.6b. Note that the symbol ϕ is used in the equivalent circuit of figure 2.6b to denote the angular co-ordinates, instead of θ. The inner and the outer rings are represented as two separate LC resonant circuits placed one within the other, with the inter-ring capacitance introduced by capacitances connecting the two LC circuits. The stronger the inter-ring capacitance, the higher the magnitude of the electric current in the rings. Many different approaches have been followed to determine an analytical formulation for this double ring, each with slightly different results. Key works in this area to mention are equivalent circuit treatments in [13, 73, 74], and the equivalent circuit treatment with polarisabilities accounted for by Sauviac et al. [75]. The fundamental resonance of this double-ring SRR is much lower in comparison to those of the individual SRRs it comprises. The reduced resonance frequency (longer wavelength) achievable by combinations of SRRs enables the design of highly sub-wavelength resonators. Densely packing such resonators allows entry into a regime where the metamaterial medium can be considered to have its own bulk medium-like properties.

2.3.2 Bianisotropy

A brief description of bianisotropy was presented in section 2.3.1 while describing the fundamental resonance of a single-ring SRR. Bianisotropy can be defined as the excitation of an electric (magnetic) dipole moment in the resonator in response to an applied magnetic (electric) field. The constitutive relations describing a reciprocal bianisotropic medium could be given by [76],

$$\mathbf{D} = \bar{\bar{\epsilon}} \cdot \mathbf{E} - i\bar{\bar{\alpha}} \cdot \mathbf{H} \tag{2.6}$$

$$\mathbf{B} = \bar{\bar{\mu}} \cdot \mathbf{H} + i\bar{\bar{\alpha}}^T \cdot \mathbf{E} \tag{2.7}$$

where $\mathbf{E}$ and $\mathbf{H}$ are the electric and magnetic field strengths, $\mathbf{D}$ and $\mathbf{B}$ are the electric and magnetic displacements, respectively. $\bar{\bar{\epsilon}}$ and $\bar{\bar{\mu}}$ are the permittivity and permeability tensors of the medium. $\bar{\bar{\alpha}}$ is a Dyadic tensor denoting polarisability. From equations (2.6) and (2.7), in an isotropic case $\bar{\bar{\epsilon}}$, $\bar{\bar{\mu}}$ and $\bar{\bar{\alpha}}$ are all scalar quantities [76]. In a bianisotropic media, the polarisability tensor describes the cross-polarisation effects i.e. polarisation of the magnetic field due to the electric field and vice versa. Bianisotropy in SRRs became a topic of interest when the experimental observations of the transmission and forbidden bands of the designed left-handed media could not be matched completely by the theory that was proposed in the original work [13, 15]. It was realised that a more accurate description of the band features could be arrived at when the bianisotropy of the SRRs in the medium, and its effect on the whole composite structure, was carefully considered [58].

A detailed analytical treatment of Pendry's double-ring SRR structure (from figure 2.6a) [13] was performed by the authors of [58]. They calculated the polarisabilities of the SRR and found that there were non-vanishing cross-polarisation terms in the calculated polarisabilities. This is attributed to the asymmetric placement of the splits in the inner and outer rings. Some other works cite the lack of an inversion symmetry in the meta-atom's geometry as the reason for the presence of bianisotropy [77, 78]. The cross-polarisation terms were found to be particularly strong around the resonance frequencies. Determining the macroscopic characteristic parameters of the medium using the calculated polarisabilities gave a better qualitative agreement with the analytical results of the left-handed system in [15]. It should, however, be mentioned here that the electromagnetic coupling of the individual resonant elements to their neighbours was still assumed unimportant in the overall picture.

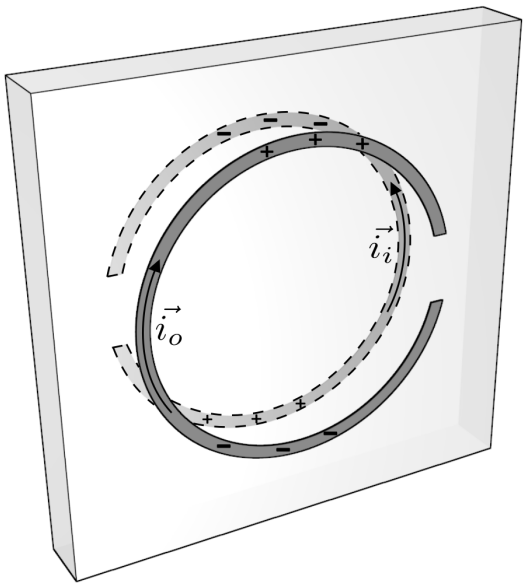

Figure 2.7: Schematic of a modified split ring resonator (MSRR) proposed in [58] as an alternative to the conventional bianisotropic SRR. The instantaneous electric currents and the inter-ring capacitive effect is seen.

Bianisotropy was shown to be undesirable for designing NIMs in [58]. The large positive values of electric polarisability and consequently also dielectric permittivity resulting from the bianisotropy, can cancel out the negative dielectric permittivity of the wire-medium in the SRR-wire interspersed arrangement, like the one in [15]. It will be shown through the work in chapter 4 of this thesis that bianisotropy has undesirable effects on inter-element coupling as well. In order to avoid bianisotropy, the authors in [58] proposed an alternate SRR design, which is shown in figure 2.7. This structure called the Modified Split-Ring Resonator (MSRR) and later Broadside Coupled Split-Ring Resonator (BC-SRR) [79], replaced the inner ring by a copy of the outer ring, fabricated on the opposite side of the substrate. The rings shared a common axis and were rotated by 180° relative to each other, as in the original bianisotropic design. The distributed capacitance between the rings allows the induced currents in the rings to be coupled, but prevents cross-polarisation. The compact design offers the advantage of enabling the fabrication of a homogenised left-handed metamaterial medium.

Several other works also studied bianisotropy in the single-ring and double-ring SRR geometries [62, 80–82], though they do not make any specific recommendations to avoid bianisotropy. Zhou et al. made an observation that the SRR's odd resonant modes (fundamental mode, second higher order mode and so on - modes with odd field symmetry) were prone to cross-polarisation, while the even modes (with even field symmetry) allowed only electric polarisations to be excited [61].

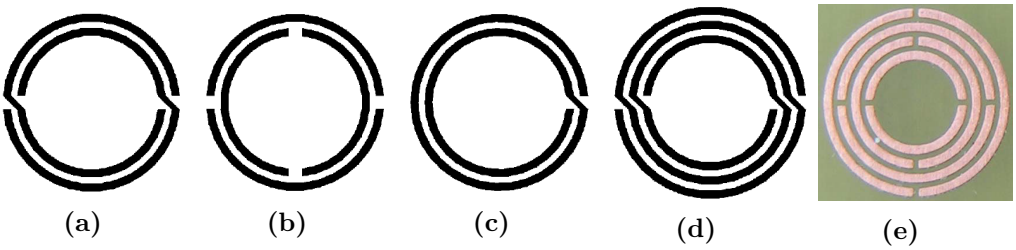

Figure 2.8: Schematics of the proposed non-bianisotropic split-ring structures to eliminate cross-polarisation effects (a) Non-Bianisotropic SRR, (b) Double-slit SRR, (c) Spiral resonator, (d) Double spiral resonator, reused with permission from [74]. (e) Photograph of a labyrinth SRR, reused with permission from [83].

Further research on non-bianisotropic structures resulted in more compact solutions [74, 84]. See figure 2.8 for schematics of the proposed structures. The non-bianisotropic split-ring resonator (NB-SRR) as named by the authors in [74] (figure 2.8a) is only slightly different from a conventional double-ring SRR, where some of the ring elements are rearranged to form a continuous loop like structure with 180° rotation symmetry. While the cross-polarisation effects are completely eliminated in this structure, the resonance frequency of the structure is still very close to that of a regular SRR of similar size. The Double-slit SRR (DSRR) (figure 2.8b) is a non-bianisotropic structure of comparable size to a normal SRR but offers twice the resonance frequency. The symmetric slits (splits) on the two rings and the 90° relative rotation, result in the net cancellation and suppression of the net electric dipole moment under magnetic excitation. Similarly, when excited by the electric field component of an incident wave (to excite higher order modes), the net magnetic dipole moment is suppressed.

The DSRR configuration was the base structure used in the labyrinth structure shown in figure 2.8e. Two more outer rings were added to the design, with every ring rotated by 90° with respect to its adjacent rings [83]. The two additional rings enable the meta-atom to become more sub-wavelength by reducing its resonance frequency. This is a consequence of the increased frequency separation between the fundamental resonances of the innermost and outermost split-rings. The last of the proposed structures is the Spiral Resonator (SR), shown in figures 2.8c and 2.8d. The SR is a single continuous spiral structure, in which the electric field is symmetrically distributed between the strips of the SR structures and hence a magnetic excitation does not induce an electric dipole moment in the structure. Adding more spiral arms to the structure as shown in figure 2.8d helps reduce the resonance frequency while still maintaining the non-bianisotropy. Besides providing equivalent circuit models to each

of these designs, the authors in [74] tested their non-bianisotropic nature under electromagnetic excitation in a rectangular waveguide. The short list of resonators discussed here describe some of the possible basic variations in meta-atom geometry to achieve non-bianisotropy and may be considered the basis set for many further design variations, which are not discussed here.

2.4 Coupled dipoles

Besides the analytical and numerical approaches to analysing coupled meta-atoms, a coupled-dipole approach can also be used. While the earlier two are quantitative analysis methods, the coupled-dipole approach to analyse metamaterials is instructive and can be employed as a toy model to gain understanding of the nature of coupling between meta-atoms and how it could influence the coupling strength between them. Since both the electric and magnetic interactions between SRRs involve the dipole moments of the structures interacting with each other, a brief summary of the coupled-dipole picture is presented first.

There are two possible orientations in which a pair of dipoles (electric or magnetic) can be positioned with respect to each other, namely transverse and longitudinal, as seen in figure 2.9. An oscillating dipole moment always has a resonance frequency associated with it. When two dipole moments are coupled, their combined oscillations cause a splitting of the resonance frequency of the system into two branches - a low frequency resonant mode (ω^-) and a high frequency resonant mode (ω^+). The relative orientation of the dipole moments determines whether a particular orientation is a high-frequency or a low-frequency solution. See figure 2.9 showing the nature of dipole interactions for transverse and longitudinal coupling.

In transverse coupling, the dipoles are coupled laterally as shown in the left part of figure 2.9. When the transversely coupled dipole moments are aligned in the same direction as shown in the top left (symmetrically), the dipoles experience a repulsive force due to the adjacency of like poles/charges. More energy is required to maintain the charge distribution in this configuration, causing this dipole orientation to be the higher frequency resonant mode. When the dipole moments are oriented antisymmetrically (pointing opposite to one another), the opposite effect occurs and the dipoles are attracted to one another, which is why this orientation corresponds to the lower frequency resonant mode. The condition is reversed when the dipole moments are coupled longitudinally. The configuration with symmetric orientation of dipoles is the

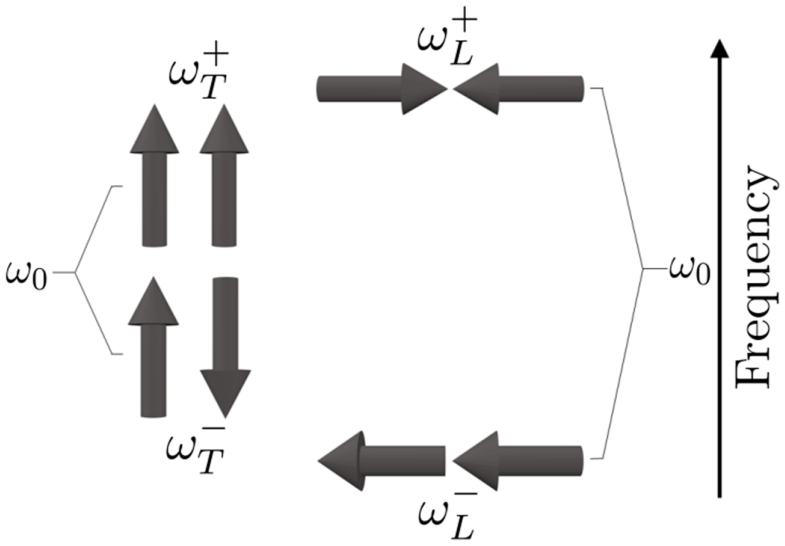

Figure 2.9: A schematic showing the splitting of the coupled modes of a pair of dipoles for both transverse (left) and longitudinal (right) orientations of the dipole moments. The magnitude of the frequency splitting is larger when the dipoles are coupled longitudinally.

low frequency resonant mode and the anti-symmetric orientation of dipoles corresponds to the high frequency resonant mode. The restoring forces experienced by the dipoles is different for the transverse and the longitudinal coupled cases, resulting in the different levels in the energy splitting of each case, as seen in figure 2.9. The coupling between the dipoles is stronger in the longitudinal case [85].

The relative orientations of the dipoles plays a vital role in determining the nature of dispersion relation in chains of multiple coupled dipoles. The works [86, 87] studying electromagnetic energy transfer in nanoparticle chain arrays are of relevance to the current discussion. The equation of motion from [86], that describes the problem of coupled dipoles in this 1D system (modified to ignore damping terms due to electron relaxation and radiation) is given by,

$$\frac{d^2}{dt^2}p_{i,m} = -\omega_0^2 p_{i,m} - \gamma_i \omega_1^2 (p_{i,m-1} + p_{i,m+1}) \tag{2.8}$$

where $p_{i,m}$, represents the displacement of the m^{th} oscillator (its charges) in the chain from its mean-position, where i represents the transverse or longitudinal orientation, ω_0 is the natural oscillation frequency of the dipole, ω_1 represents the strength of interaction of each dipole with its neighbours (equal interaction with neighbours assumed here due to periodicity), and $\gamma_T = 1$, $\gamma_L = -2$ is a constant according to the relative dipole orientation. A propagating wave solution for this equation of motion, takes the

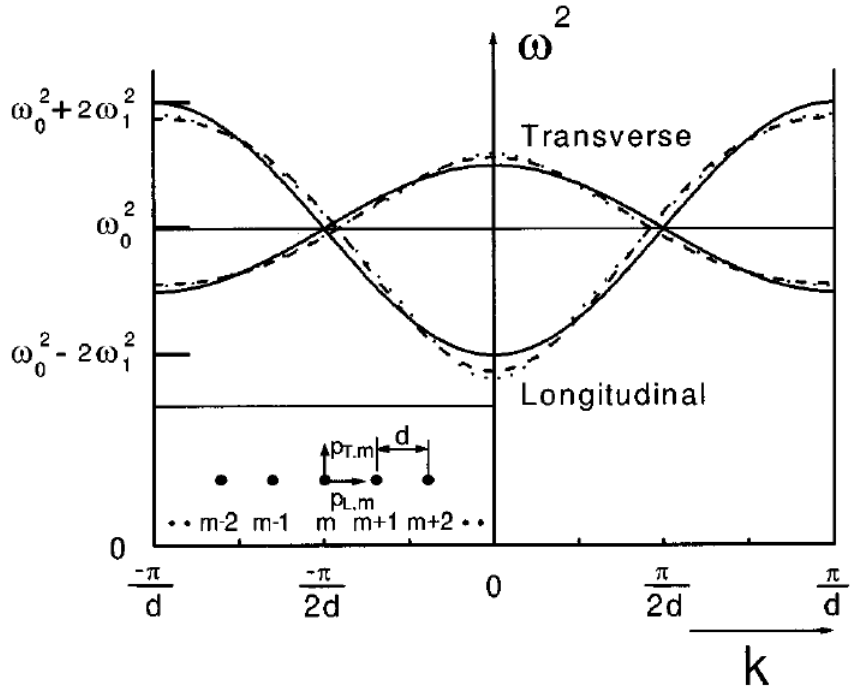

Figure 2.10: Dispersion relation for the coupled transverse and longitudinal plasmon modes in a metal nanoparticle chain (in the inset). Solid curves include nearest-neighbor interactions only, the dashed curves include next-nearest-neighbor interactions, and the dotted curve include fifth-nearest-neighbor interactions. Reused with permission from [86].

form

$$p_{i,m} = P_{i,0}\exp[-\alpha md + i(\omega t \pm kmd)] \tag{2.9}$$

where $P_{i,0}$ represents the dipole moment of the very first oscillator in the chain (at $m = 0$), α represents the attenuation coefficient, k the propagation constant/wavevector, and ω the angular frequency of the propagating wave. Notice in equation (2.9) that there are two solutions: $(\omega t - kmd)$ where the phase and group velocities are along the same direction corresponding to the positive dispersion of the nanoparticle chain, as shown in figure 2.10, and $(\omega t + kmd)$ has the phase and group velocities directed anti-parallel to each other (backward-wave), and corresponds to the negative dispersion seen in figure 2.10. Assuming minimal attentuation, the simplified dispersion relation of the system is given by

$$\omega^2 = \omega_0^2 + 2\gamma_i\omega_1^2\cos(kd) \tag{2.10}$$

From the corresponding dispersion curves plotted in figure 2.10, it can be observed that the transversely and longitudinally coupled chains of dipoles exhibit negative and

positive dispersions, respectively. Similar to the coupled dimer case, where it was observed that the longitudinally coupled dipoles result in a broader energy splitting, the bandwidth of the longitudinally coupled chain of dipoles (positive dispersion) is seen to have a broader bandwidth than the transverse case, due to stronger inter-neighbour interaction in the chain. A more detailed analysis of the relationship between the relative orientation of the coupled dipoles and the corresponding observed dispersion will be discussed in chapters 5 and 6 of this thesis, on the topic of wideband metamaterial waveguides.

2.5 Electromagnetic coupling between split-ring resonators

From the discussion in section 2.4, it was seen that changing the relative orientation and position of dipoles with respect to each other can result in vastly different responses. The discussions in the previous sections have shown that a SRR (bianisotropic in this case) can be represented using both its electric and magnetic dipole moments, the relative orientations and separation between SRRs can also result in different resonant responses from the coupled system. In this section, the discussion on SRR interactions is categorically divided according to planar coupled SRRs and axially coupled SRRs, and extend the review to literature on chains of SRRs.

2.5.1 Planar coupling - SRR dimer

When two SRRs are arranged on the same plane, only a fraction of the magnetic energy from one SRR reaches its neighbours. Therefore, the coupling strength is very weak in planar coupled SRRs. When only one of the SRRs excited, as shown in figure 2.11a, the magnetic field of the excited SRR loops through the centre of the second SRR, inducing an electric current in the second SRR as well. The directions of the magnetic field at the centres of the two SRRs is opposite, as observed in [23]. The mutual inductance between the two SRRs is therefore considered to be negative.

In the same year as the publication of [23], the coupling between double-ring SRRs was also studied by excitation inside a rectangular waveguide [57]. Hesmer et al. [88] performed a more detailed experimental study on the strength of coupling between two planar coupled SRRs under different relative orientations, the schematic of which is shown in figure 2.11a. The black dots at the centre of the SRRs denote the axial point about which each of the SRRs can be rotated in-plane, independent of each other. The excited magnetic field of the first SRR and the induced magnetic field in the second

SRR, both shown by solid blue lines, are anti-symmetrically oriented. However, two resonant modes (corresponding to the symmetric and anti-symmetric dipole orientations) were observed in both the experiments and simulations of [88]. The electric fields (solid red lines) excited at the capacitive split-gaps of the SRRs due to bianisotropy also contribute to the electromagnetic coupling depending on the relative orientation of the SRRs. This work was the first that explained how depending on the change in relative orientation between the planar coupled SRRs, the nature of coupling can be dominated by the magnetic and/or electric interactions. It was also identified in their work that the splitting of the resonant modes was due to the coupling between the SRRs, similar to the energy splitting in coupled dipoles.

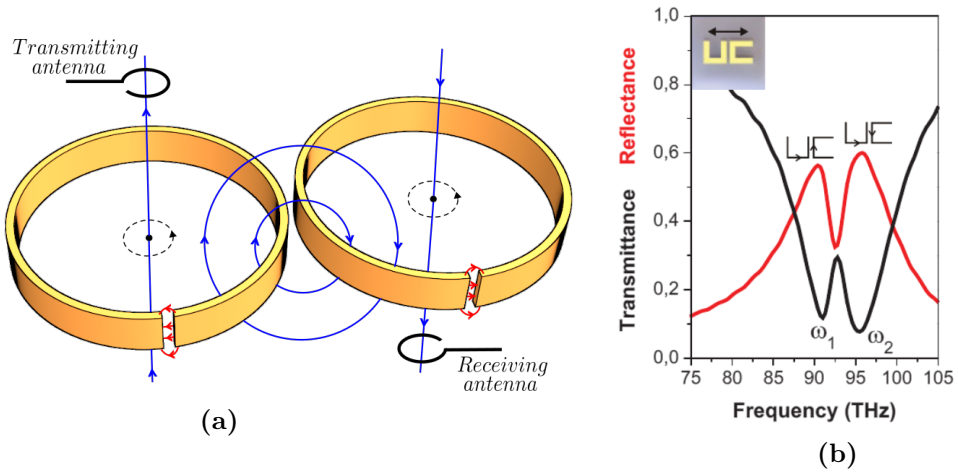

Figure 2.11: (a) Schematic of the planar coupled SRR dimer studied in [88]. The central axes of the two SRRs are shown by the black dots about which the SRRs can be independently rotated relative to each other. An instantaneous magnetic field (solid blue lines) excited in the first SRR (left) by a transmitting loop antenna induces a magnetic response in the second SRR by looping through it. The solid red lines show the instantaneous electric field excited at the split-gaps in response to the electric currents in the SRRs. (b) Simulated transmittance and reflectance curves of a coupled U-shaped SRR dimer with resonance frequencies in the THz frequency range (reused with permission from [89]). Inset diagram shows the relative orientation of the U-shaped SRRs.

The essence of the findings from [88] is as follows:

1. Irrespective of the relative arrangement, the electric and magnetic dipole moments excited in the first SRR always induced both a symmetric and an anti-symmetric configuration of dipole moments in the second SRR, giving rise to two coupled resonances.

2. The relative orientation of the split positions of the two SRRs influenced how

strongly the two SRRs were coupled to each other. When the rings were rotated such that the splits of the rings were on the opposite sides, the magnetic coupling between the SRRs dominated. When the SRRs were rotated such that the splits were in immediate proximity, the strong electric and magnetic interactions resulted in the strongest coupling and therefore, the strongest splitting between observed resonant modes.

The magnetic coupling between SRRs in a plane was also studied in the THz regime using U-shaped SRRs by Liu et al. [89]. The electric field interaction was deliberately minimised by orienting the SRRs as shown in the inset of figure 2.11b. Under excitation by normally incident radiation, the fields of the excited first SRR coupled to the second inducing a "plasmon hybridisation". Their plasmonic resonance frequencies hybridise to form new symmetric and anti-symmetric states. Figure 2.11b shows the simulated transmittance and reflectance curves for the inductively coupled SRRs. The transverse symmetric and anti-symmetric electric current directions in the two SRRs are also shown next to the observed resonant features. In the absence of electric interactions, anti-symmetric and symmetric magnetic coupling result in the lower and the higher frequency hybridised modes. This is in agreement with the preferred lower and higher energy modes of the transverse symmetric and anti-symmetric coupled dipoles, as shown in figure 2.9. Another notable work studying planar coupled SRRs is reference [90], which studies in detail the strength of coupling as a function of changing relative orientation and separation between SRRs. The general ideas conveyed by the work have already been discussed here.

2.5.2 Axial coupling - SRR dimer

When SRRs are stacked one above the other such that they share a common axis, there is an increased overlap of the fields of the two SRRs and therefore, an enhanced interaction. A wide range of coupling strengths between the SRRs can be probed in this configuration, since the distance between the two rings can be decreased until the rings are practically in contact. The strength of the coupling should only get stronger with decreasing separation distance, as one might expect from coupled-dipole theory. The stronger interaction between the axially coupled rings results in stronger effective dipole moments.

The SRR dimers in the axial coupling configuration have occasionally been referred to as stereometamaterials because of their resemblance to stacked molecules in stereochemistry, after the work by Liu et al. [91]. Upon excitation with an electromagnetic wave, the strength of the electric dipole moment coupling between the SRRs in the

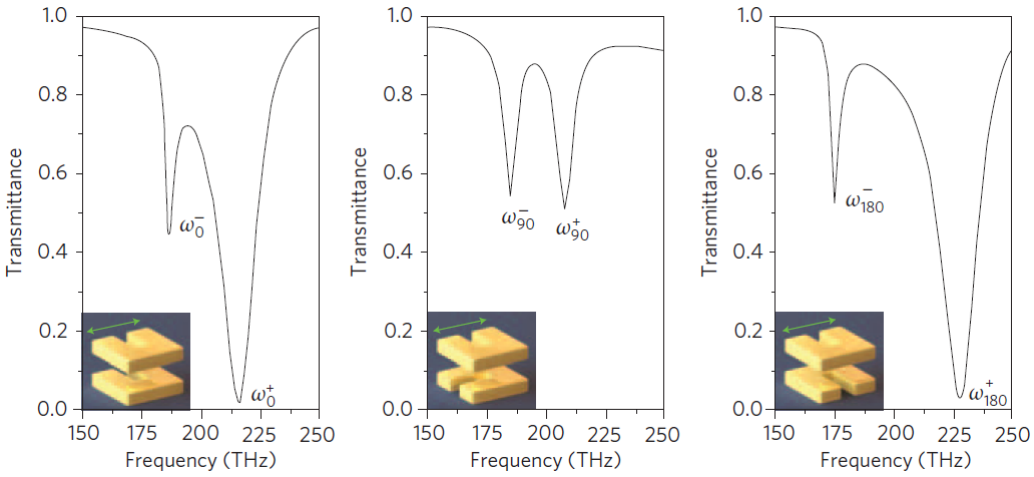

Figure 2.12: Simulated transmittance for the case of two axially coupled SRRs, with the second SRR rotated by 0°, 90° and 180°, shown from left to right. (Insets) Relative orientation of the coupled SRRs with the green arrow indicating the direction of electric field polarisation in incident radiation. Figures reused with permission from [91]

pair changes depending on the relative rotation/twist angle. In axially coupled SRRs, the three relative orientation angles of 0°, 90°, and 180° between the SRRs exhibit unique cases of coupling, as shown in [91]. Figure 2.12 shows the simulated frequency dependent transmission curves corresponding to these cases. The insets in each case shows the corresponding orientation of the two SRRs relative to each other and to the electric field polarisation in the incident radiation (shown by the green arrow).

As seen from figure 2.12, all the three cases show two resonant modes, which is a clear indication of electromagnetic coupling between the SRRs. Changing the relative orientation between the two SRRs changes the nature of the resonant modes and the frequency splitting between them. This behaviour of varying coupling strength between the SRRs as a function of their relative rotation angle has also been observed in [71, 92, 93]. A more detailed discussion on axially coupled SRR dimer will be presented in chapter 4, where the electromagnetic interactions in an axially coupled SRR dimer are analytically and experimentally characterised as a function of both relative orientation and separation.

2.5.3 Magneto-inductive coupling and wave propagation in 1D metamaterials

When the length of the coupled system is extended, i.e. when more SRRs are added along a single direction to form a linear chain, they become of use in applications such as magneto-inductive (MI) waveguides [22, 23], and wireless power transfer [26]. When

the first SRR in the chain is excited, the harmonically varying electric currents in the SRR give rise to correspondingly oscillating magnetic fields. The magnetic field of the SRR drives electric currents in the neighbouring SRRs, thereby transferring energy down the chain by virtue of the inductive coupling between the SRRs. The nature of this 'magneto-inductive' wave propagation and their dispersion relations in both axially coupled and planar coupled SRRs have been demonstrated in [22, 23, 94].

Shamonina et al. derived the dispersion equation of such a 1D MI system in [23] as,

$$1 - \frac{\omega_0^2}{\omega^2} - \frac{i}{Q} = \sum_{s=1}^{u} \kappa_s \cosh(s\gamma a) \tag{2.11}$$

where ω is the angular frequency of the wave and ω_0 is the resonance frequency of each SRR, $Q = \omega L/R$ is the quality factor, i is the imaginary unit (not to be confused with electric currents from the previously discussed works), $\kappa_s = 2M/L$ is the coupling coefficient between two SRRs (M being the mutual inductance between SRRs and L the self-inductance of each SRR) that are separated by distance sa (a being the distance between adjacent SRRs and s denoting the position of a SRR in the chain containing 'u' coupled SRRs), and $\gamma = k_a + ik_p$ (once again not to be confused with the constant γ_i used in the coupled-dipole dispersion equation), with k_a the attenuation coefficient and k_p the wavevector of MI wave propagation, also called the phase constant. Though conventionally, α and β are used to denote the attenuation and phase constant respectively in literature, the same constants are used to denote the magnetic and electric coupling coefficients in our work in chapter 4. Hence, the new symbols have been suggested and used in the rest of the work with the motivation to avoid confusion. If the system is assumed to be lossless ($Q = \infty$) and one limits the interactions to be between only nearest neighbours, the dispersion equation from (2.11) reduces to [95],

$$1 - \frac{\omega_0^2}{\omega^2} = \kappa \cos(k_p a) \tag{2.12}$$

Comparing this equation with the dispersion equation for a 1D chain of coupled dipoles from equation (2.10), one can appreciate the similarity between the two cases. The dispersion in either case is described in terms of the oscillation frequency of each resonator on its own, along with a coupling coefficient quantifying the strength of interaction between neighbouring resonators. Similar to the constant γ_i in the 1D chain of coupled dipoles that takes positive or negative values depending on relative dipole orientation, the coupling coefficient κ in equation (2.12) takes a minus sign for transversely coupled dipoles in planar resonators ($-M$) and a plus sign for the longitudinally

coupled dipoles in the axially stacked resonators ($+M$). Plugging in some arbitrary values for the terms in equation (2.12), such as nearest-neighbour separation a =10 mm, a frequency value of choice and coupling coefficient value of -0.1 for transverse MI coupling and 0.1 for longitudinal coupling, helps visualising the nature of dispersion in each case. The dispersion curves calculated using these values, for the transverse and longitudinal MI systems are shown in figures 2.13a and 2.13b, respectively. The insets show a section of a sample SRR chain in each case.

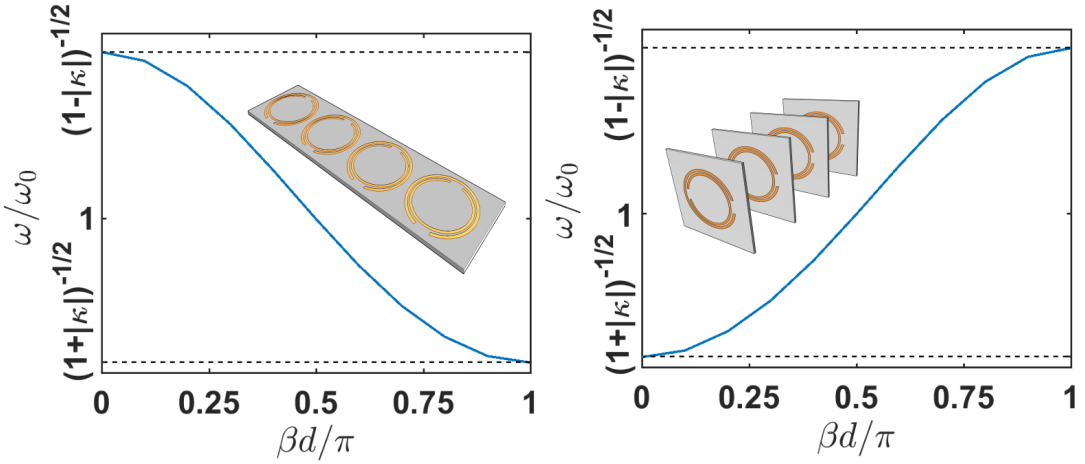

Figure 2.13: Dispersion relations ($\omega-\beta$) calculated for magneto-inductive (MI) waves in (a) planar coupled and (b) axially coupled linear chains of SRRs. The separation between SRRs was assumed to be a =10 mm, and the coupling parameter set at $\kappa = -0.1$ for the planar case and $\kappa = 0.1$ for the axial case. Insets show schematics of the SRR layout corresponding to each of the cases.

The similarity of the two MI dispersion curves to the corresponding coupled-dipole cases in figure 2.10 show that under certain cases of lattice arrangement when only the nearest neighbour interactions are significant, the responses of a 1D metamaterial waveguide can be qualitatively described using a coupled-dipole approach. When interactions among multiple neighbours are to be taken into account, and when the inter-element interaction is quite strong due to dense metamaterial packing, near-field effects and non-nearest neighbour coupling coefficients need to be included in the calculation to improve accuracy. A 1D MI waveguide can be used to develop several applications such as power dividers, power coupling lines, and delay lines, as suggested in [23].

When a 2D planar arrangement of SRRs as shown by [96], was placed next to another 2D or quasi-2D arrangement (mixture of planar and axial arrangements) of

SRRs with a different resonance frequency from those in the first, MI waves underwent refraction at their interface. When the second SRR medium's lattice arrangement was rotated with respect to the first such that its MI wavefront was rotated with respect to that of the first medium, negative refraction was observed without the necessity for a negative refractive index or backward-wave propagation. This important finding by [96] was the first to be shown with SRR metamaterials, though Luo et al. in [97] had already demonstrated it using photonic crystals.

The 1D treatment of MI waves can easily be extended to 2D and 3D by adding more dimensions to the dispersion relation shown in equation (2.11). However, the discussion of SRR interactions in 2D and 3D media are beyond the scope of this thesis. Therefore, the reader is directed to works such as [23, 54] for more in-depth analyses of 2D and 3D MI waves.

2.6 Electro-inductive coupling

The term electro-inductive (EI) coupling was first coined in [98], where the authors proposed systems comprising the so-called complementary SRRs (CSRRs) where the CSRRS were coupled to one another via capacitive (or electric) interactions.

2.6.1 Complementary resonators - duality and complementarity

In the discussion in section 2.2, it was mentioned that wire arrays behaved like plasma and could be made to exhibit negative permittivity values at a suitable frequency. They were natural choices for negative ϵ media in several early designs of left-handed metamaterials. Despite their effective contribution, there did not exist a more compact and easily tunable electric counterpart to the SRRs. Falcone et al. used the concepts of duality and complementarity [99–101] as dictated by Babinet's principle to design a new kind of resonator, called the complementary SRRs (CSRRs) [102], an example of which is shown in figure 2.14. Babinet's principle states that the diffraction pattern created by a 2D object should be identical to that created by a hole in a screen, of the same shape and size as the object. The amount of light diffracted by the two (the beam intensity) would however, be different in each case. In Babinet's principle, the electric and magnetic fields in Maxwell's equations are dual. Thus, if the field distribution of a regular resonator such as a SRR is known, the electromagnetic field distribution of its complementary structure can be worked out simply by interchanging the electric and magnetic fields of the regular resonator.

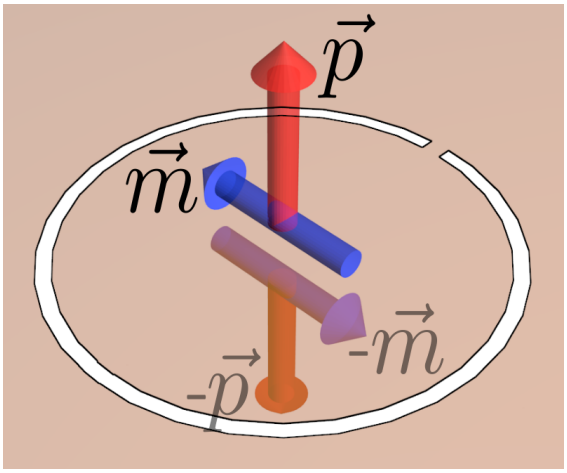

Figure 2.14: Schematic of a single-ring complementary SRR (CSRR) meta-atom showing local out-of-plane electric (red arrows) and in-plane magnetic (blue arrows) dipole moments on either side. The net dipole moment of the CSRR meta-atom is zero.

A CSRR is realised by replacing the metallic portions of a SRR with air-gaps and the air surrounding the SRR in its plane by metal, as if to create a negative image of the SRR [102, 103]. The CSRR shown in figure 2.14 is the complementary counterpart of the single-ring SRR that was shown in figure 2.3b. Consider also the cross-sections of the single-SRR and its complementary SRR shown in figure 2.15. It can be seen that the out-of-plane magnetic fields of the SRR are replaced by the out-of-plane electric fields in the CSRR and vice-versa, due to complementarity. Note however from figures 2.14 and 2.15b that owing to the continuous metal screen in the CSRR, the out-of-plane electric fields cannot be continuous across the boundary. Therefore, the direction of the electric fields and consequently, that of the magnetic fields are opposite on either side of the meta-atom. Note that although the magnetic field in the CSRR is dominant in the split-regions (like the electric field of the SRR), there will still be magnetic field lines at the centre of the meta-atom due to weak electric currents. This can be thought of in parallel to the surface capacitance between the charges on the inner surface of the split-ring, as discussed in section 2.3.1.

The effective local dipole moments of the CSRR meta-atom as seen from figure 2.14 can be represented by oppositely pointing arrows - out-of-plane electric dipole moments shown by red arrows and in-plane magnetic dipole moments by blue arrows. The local dipole moments on the top and bottom of a complementary resonator are equal in strength and oppositely polarised. The CSRR meta-atom therefore, does not have a net electric or magnetic dipole moment, but can be excited locally on either side using time-varying electromagnetic fields and can interact with other adjacent CSRR

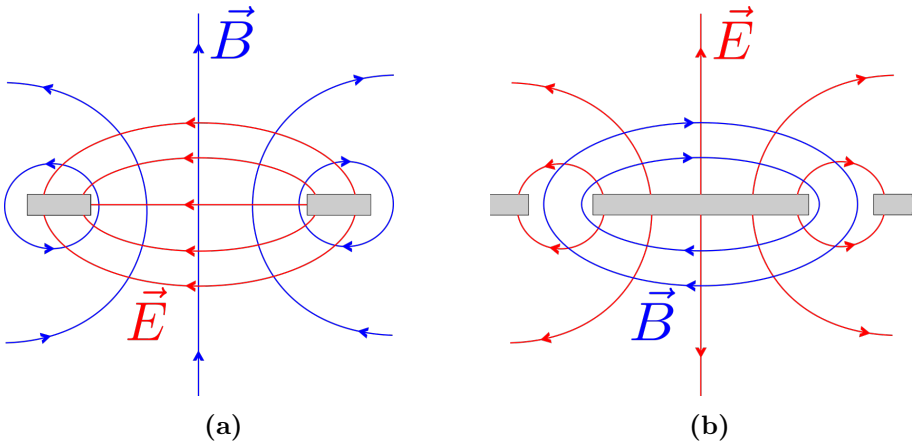

Figure 2.15: The electric (red lines) and magnetic (blue lines) field lines seen at the cross-section through the centre of single-ring (a) SRR and (b) CSRR meta-atoms, without a substrate. The solid grey lines indicate the metallic portions of the meta-atoms. The duality between the fields of the SRR and CSRR are seen through their interchanged positions.

meta-atoms through excited near-fields. The duality between the electric and magnetic fields of SRRs and CSRRs is reflected in their effective material properties as well. The negative magnetic permeability of the SRR is replaced by a negative electric permittivity in a CSRR, close to its resonance frequency [102].

In the equivalent circuit approach to designing the CSRRs, the duality is implemented by replacing every inductor in the circuit design of a SRR by a capacitor and vice-versa [74, 102–104]. Circuit elements connected in series in the regular SRR's circuit are replaced by their complementary elements connected in parallel and vice-versa. For a single-ring SRR and its CSRR, switching the inductive and capacitive elements results in the same LC resonant circuit. Ideally, this means that their fundamental resonances should also occur at the same frequency. The inter-element coupling in CSRRs, however, is visualised in terms of mutual capacitance which is complementary to the mutual inductance between SRRs.

2.6.2 Axial and planar coupling in the complementary resonators

When a dual complementary counterpart to the SRR exists, it is only natural that a complementary concept to the magneto-inductive coupling exists. The EI coupling in a planar microstrip waveguide etched with CSRR patterns was first demonstrated in [98]. The photograph of the EI CSRR waveguide used, is shown in figure 2.16. The dispersion relation for the EI wave propagation was also provided in the work, which (after using some new symbols for parameters to avoid confusions and rearranging) is

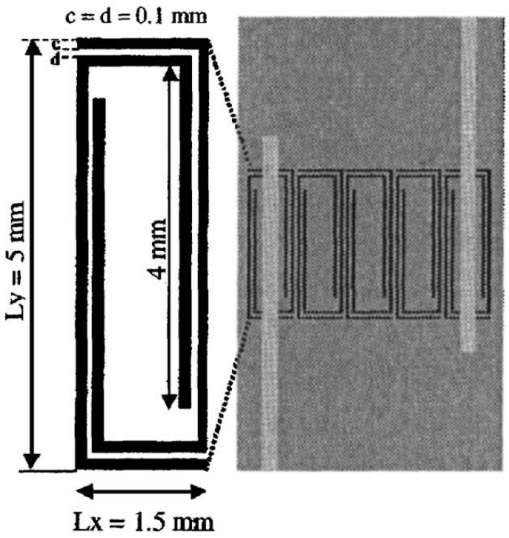

Figure 2.16: Electro-inductive (EI) CSRR waveguide manufactured in microstrip technology, used in [98] (reused with permission from [98]).

given for the lossless case by,

$$1 - \frac{\omega_0^2}{\omega^2} = -\kappa_C \cos(k_p a) \tag{2.13}$$

where $\kappa_C = 2C_M/C_C$ denotes the coupling coefficient and is quite similar to the magneto-inductive coupling term κ $(= 2M/L)$ observed in equation (2.12). C_M is the mutual capacitance between CSRRs and C_C the self-capacitance of each CSRR. Irrespective of the axial or planar arrangement of the CSRRs, the EI wave propagation always has a negative dispersion [105]. Irrespective of the relative orientation of neighbouring CSRRs, electric coupling arises due to the capacitive effect between the CSRRs' opposite charges. A negative mutual capacitance is not possible. Therefore, equation (2.13) always describes a negative dispersion, with the passband's bandwidth determined by the strength of the coupling coefficient. The CSRR has been one of the popular candidates for metamaterial based transmission-lines [106–108].

More works followed treating the CSRR chains and the concept of electro-inductive waves from a different perspective [109, 110]. Reference [109] deals with metasurfaces containing CSRR arrays which were used to spoof plasmon modes by confining electromagnetic energy to the surface on a subwavelength scale. The metasurfaces exhibit a negative dispersive behaviour as a consequence of electro-inductive effects. The idea of interaction among the CSRRs via the spoof plasmons was later extended into an electro-inductive waveguide concept in [110]. A completely different idea to the waveguiding was to alternatively stack 2D CSRR metasurfaces and 2D SRR metasurfaces

[111]. This stacked 3D metamaterial device was shown to support ultraslow modes in the microwave regime. This is a very useful concept for designing devices like spatial delay lines. As interesting and novel the electro-inductive waves are, more research is still being performed in the area to give way to more useful applications.

2.7 Summary

A historical outlook of the research in electromagnetism, leading to the birth of metamaterials was provided. A comprehensive review of the literature on electromagnetic interactions between split-ring resonators (SRRs) and complementary split-ring resonators (CSRRs) was presented. SRRs interact with each other via magneto-inductive coupling and CSRRs via EI coupling. If the meta-atoms are bianisotropic, both electric and magnetic fields participate. Magneto-inductive coupling can result in a positive or a negative dispersive behaviour depending on if the relative meta-atom orientation is axial or coplanar. On the other hand, EI coupling due to mutual capacitive effects always results in a negative dispersion.

Chapter 3

Methods

3.1 Introduction

This chapter details the sample fabrication procedure, experimental equipment and measurement techniques along with the numerical and analytical modelling techniques used for the generation of the experimental and computational results presented in the forthcoming chapters.

3.2 Sample fabrication

The samples fabricated for all the experiments in this thesis consist of patterned metallic structures clad on rigid plastic substrates. The maximum dimensions of a single unit in the samples measure on the millimetre scale. The base material for making these samples are printed circuit board (PCB) laminates. These commercially available PCBs are about the size of an A3 sheet of paper, with 35μm of copper electrodeposited on one side of a plastic board as shown in figure 3.1a. The plastic boards are 1.5 mm thick, supplied by Rogers Corporation and Isola group depending on the substrate's dielectric permittivity required for the specific study.

A single unit of each fabricated sample is a split-ring resonator (SRR) or a variation of it, that has a curved geometry that is challenging to be realised accurately through standard 'print-and-etch' techniques. The high resolution required for realising these structures were achieved through photolithography using laser imaging done with the in-house Durham Magneto Optics laser writer or the more sophisticated Laser Direct Imaging (LDI) device of a local PCB manufacturer, Graphic PLC. The laser writer is suitable for the batch fabrication of ten samples or fewer, given its high write time. LDI is preferred for the fabrication of samples in their hundreds. The photolithography

process is explained using the example of a 2D array of basic split-ring resonator shapes.

3.2.1 Photolithography

The different stages of sample fabrication using the photolithography procedure are shown in figure 3.1. As a first step, the PCB laminate from figure 3.1a is coated with a thin layer of positive photoresist, as shown in figure 3.1b. The positive photoresist is sensitive to light and becomes soluble in a developer by exposure to a laser beam of suitable wavelength. PCBs with side dimensions measuring about 10 cm or less can easily be spin-coated with photoresist using a spinner. Larger PCBs require a photoresist film to be coated using heat rollers.

The strategy to realise the required split-ring shaped patterns through laser writing is to shield the resist coated laminate with a photomask containing the target shapes. The masking pattern is written directly onto the interfacing software. The laser beam is raster scanned across the resist coated laminate skipping areas according to the masking pattern. The in-house laser writer employs a laser of wavelength 405 nm and spot size 5 μm. The industrial LDI machine does a raster scan over an area of 610 mm $\times$ 450 mm in 10 seconds with a resolution of 35 μm. Both device resolutions are at least a hundred times finer than the smallest dimensions in the fabricated structures. The exposed area of photoresist is readily soluble in a photoresist developer. Figure 3.1c distinguishes the areas of photoresist using a lighter shade from the blocked patterns.

The exposed laminate is then washed in a bath of photoresist developer with a gentle rocking motion for about 30 seconds to dissolve the photoresist. The laminate is immediately transferred to a bath of de-ionised water and cleaned of any developer liquid. Post-development, the laminate looks like that shown in figure 3.1d. The developed laminate is immersed in a heated bath of Ferric Chloride etchant to strip off the exposed copper. The portions of split-ring shaped photoresist along with the metallic regions underneath them are retained as shown in figure 3.1e. The remaining photoresist is then removed by wiping the surface with acetone solvent, leaving the final copper split-ring shapes on the substrate as in figure 3.1f.

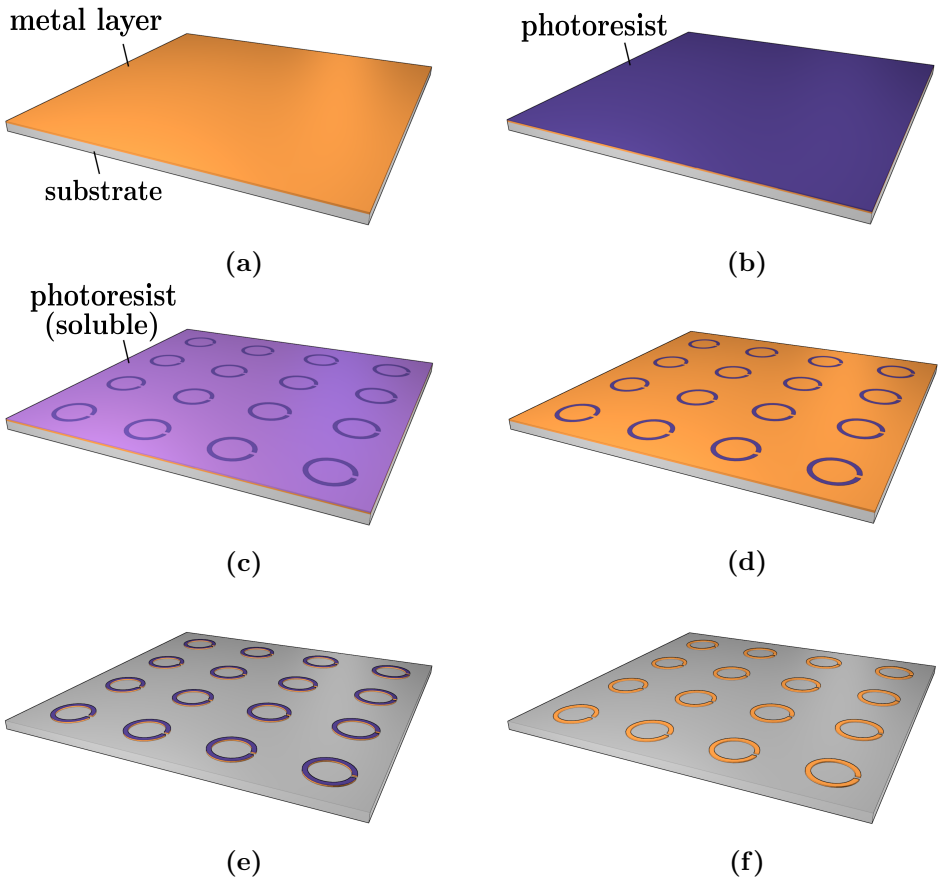

Figure 3.1: The steps involved in fabricating a 2D array of meta-atoms (split-ring resonators have been picked as an example) using standard lithography. (a) A PCB laminate with copper electrodeposited on one side, (b) PCB laminate uniformly coated with a positive photoresist, (c) exposure of photoresist on the PCB to laser light via a laser writer with pre-loaded patterns, (d) removal of exposed photoresist by cleaning in a developer solution, (e) etching the developed PCB in a Ferric Chloride bath to strip of exposed metal, (f) removal of photoresist by cleaning with acetone solvent.

3.3 Experimental equipment

3.3.1 Vector Network Analyzer

A Vector Network Analyzer (VNA) is a network analysing device used to characterises a Device Under Test (DUT) by recording the amplitude and phase of the electromagnetic signals reflected from and transmitted through the DUT, relative to the original signal that was sent as input. For all measurements in this thesis, the MS4644A Anritsu two-port VNA capable of generating AC signals in the frequency range of 10 MHz to 40 GHz was used.

Figure 3.2a shows the block diagram representation of a two-port VNA with both

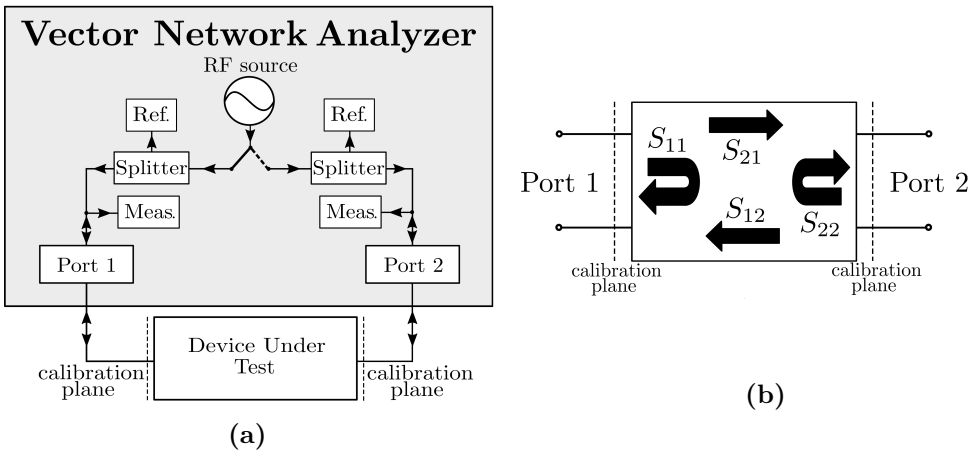

Figure 3.2: (a) Schematic diagram of a Vector Network Analyzer (VNA) showing the input and output signal processing blocks and a Device Under Test (DUT) connected to the two ports of the VNA. (b) The S-parameters corresponding to the reflected and transmitted signals from the DUT with the direction of propagation of each signal shown by the black arrows. The calibration planes are set at the ends of the DUT.

ports connected to the DUT. The RF source in figure 3.2a constitutes a crystal oscillator, the spectral purity of which is maintained in a phase-locked loop by another voltage controlled oscillator. Part of the input signal is split and stored as a reference signal (in the reference circuit marked Ref. in figure 3.2a). This reference signal is used to assess the returned signal's strength and phase shift relative to the input signal. The signal detection (marked Meas. in figure 3.2a) at the receiving section of the ports work on the heterodyne principle, where the incoming signal frequency is mixed with a local oscillator signal to generate a low intermediate frequency (IF) signal. It is to be noted that the amplitude and phase information are retained in the mixing process and only the frequency of the signal is altered for digital signal processing and data storage. The calibration planes mark the boundaries of the DUT. By default, the calibration planes are set at the ports of the VNA, but by a prescribed calibration procedure, they may be moved to the ends of the DUT, so that the connecting cables are not part of the analysed system. The Anritsu VNA MS4644A has a noise floor level of -110 dBm ($1 * 10^{-11}$ times) below an input power of 0.1 mW in the frequency range of 10 MHz to 2.5 GHz [112]. In the same frequency range, the receiver dynamic range (the difference between the maximum and minimum detectable signals) of the device is 120 dB. With good calibration, the data recorded in the VNA would always have its minimum detectable signal above the noise floor such that it is not lost.

The data in the VNA are in the polar form giving the linear amplitude and phase of the recorded signals, which are stored as complex values called the scattering param-

eters (S-parameters). The linear amplitude can be directly squared to determine the signal power. The S-parameters are ratios of the recorded to the input signal strengths at the VNA ports. They are represented by S_{mn} with m representing the output port and n representing the input port. A N-port VNA has N^2 scattering parameters. Figure 3.2b shows the four S-parameters that are recorded by a two-port VNA, to fully characterise the DUT. The VNA has an auto-reversing feature through which both ports can almost simultaneously perform the function of an input and an output port and all four S-parameters are almost simultaneously recorded [113]. The S_{11} and S_{22} ($m = n$) scattering parameters give the ratio of the incoming signal strength at the ports to the outgoing signal strength from the same port. Similarly, the parameters S_{21} and S_{12} ($m \neq n$) give the ratio of the received signal strength at the output port to the input signal strength from the other port. The relative transmitted or reflected power from the DUT is obtained from $\|S_{mn}\|^2$ with a minimum value of 0 and a maximum of 1.

With reference to the study of metamaterial systems, the DUT can be any of the following: a metamaterial analysed by exposure to plane microwaves from a radio antenna connected to the input port of the VNA and the scattered radiation collected by another radio antenna at the VNA's output port, or a closed measurement system such as a waveguide filled with 1D metamaterials, or a metamaterial whose modes are excited and probed at close range by near-field antennas. All kinds of DUT relevant to the work in this thesis will be discussed in the subsequent sections of this chapter.

The VNA needs to be calibrated for experiments with the rectangular waveguide, since the studied system needs to be accurately characterised based on the frequency dependent reflection and transmission recorded at the ends of the waveguide. The calibration planes are set at the ends of the rectangular waveguide through TRL (Thru-Reflect-Line) calibration, which is a 2-port calibration technique. In this technique, two transmission measurements between the two ports (with a line of zero length and a line with $\lambda/4$ electrical length, where λ is the wavelength corresponding to the waveguide's central frequency) and one reflection measurement (for each port with a highly reflective surface) are performed to determine error co-efficients for the two ports and compensate for them in the actual measurements [114].

In the experiments that employ near-field measurements, the information regarding the strength of the frequency components in the DUT are directly extracted from the measured data through Fourier transform. The key information needed for this process is the strength and phase of the measured field components relative to each other as if to create a field-map. Therefore the VNA does not need calibration to characterise this

system. The section 3.5 briefly outlines the Fourier transform post-processing done on the experimental data to construct a dispersion diagram for a tested metamaterial.

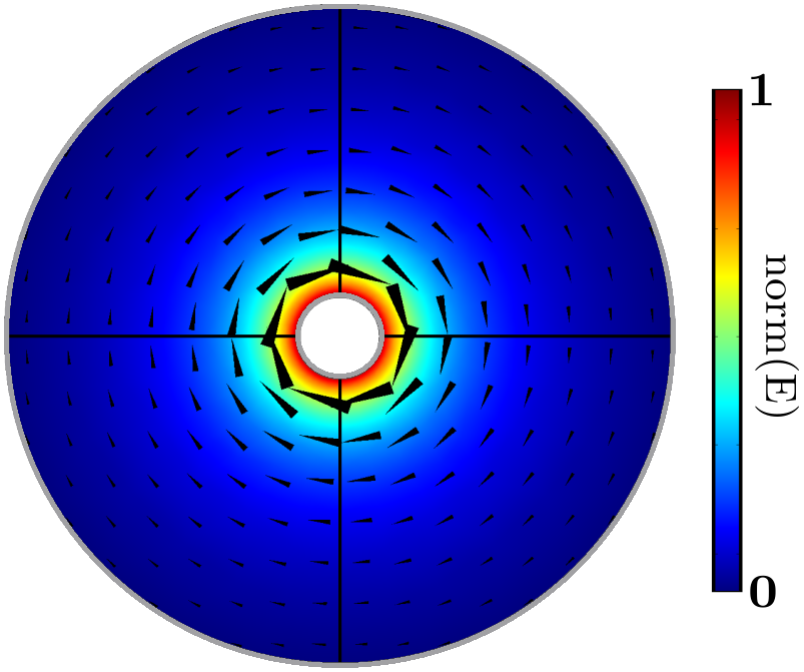

Figure 3.3: Cross-section of a coaxial cable showing the norm of electric field as a colour map and black arrow heads representing the instantaneous magnetic field of the Transverse Electromagnetic (TEM) coaxial mode, all computed in COMSOL. The central metallic conductor and the outer metallic sheath (ground) are shown as grey outlines. The colour bar shows the strength of the electric-field norm normalised to the maximum value close to the central conductor. The field strengths of both the field components are seen to be the strongest close to the central conductor, decaying as the reciprocal of distance away from the centre.

3.3.2 Coaxial cables

The coaxial cables that connect the DUT to the VNA are waveguiding structures, guiding the signal from the VNA to the DUT as transverse electromagnetic modes (TEM). The coaxial cables have a central cylindrical conducting wire, in which an electric current is driven at a range of frequencies. The central conductor is surrounded by an outer metallic sheath that also serves as an electric ground for the inner conductor. The gap between them is usually filled with a plastic dielectric and sometimes even air. Figure 3.3 shows the cross-section of a coaxial cable, where the inner metallic conductor and the outer metallic sheath are drawn in grey. The electric current driven in the central conductor gives rise to electric field directed radially outward from the central conductor to the outer metal sheath and a circular magnetic field around the central

conductor. The fields associated with this TEM mode are also plotted in figure 3.3. The distribution of the electric field's magnitude across the coaxial cable's cross-section, via the normalised electric field norm given by

$$\|\mathbf{E}\| = \sqrt{\mathbf{E}\mathbf{E}^*} \tag{3.1}$$

where $\mathbf{E}$ is the complex electric field vector. The black arrowheads in the plot represent the direction of the instantaneous magnetic field. Naturally, the fields are stronger closer to the central conductor and decay radially outward with an inverse relationship to the distance from the central conductor.

3.3.3 Rectangular waveguide

Metamaterials are designed so as to interact readily with electromagnetic waves and manipulate them. Their response stems from the nature of their constituent meta-atoms. SRRs, for example, are highly scattering resonant elements that interact very strongly with electromagnetic radiation close to their resonance frequency. In order to characterise the electromagnetic interactions among multiple coupled SRRs mediated by their near-fields as well as the radiated fields, closed measurement systems such as rectangular waveguides offer a reliable means by capturing the energy scattered by the analyses system with minimal losses. Rectangular waveguides have been widely used by researchers for the analysis of meta-atoms and one-dimensional metamaterials [74, 115–118].

Rectangular waveguides are hollow metallic structures that guide electromagnetic waves. When placed between the two ports of the VNA as the DUT as shown in figure 3.2a, the VNA ideally records a 100% transmission of energy from the input port to the output port and 0% in reflection at the input port, after calibration. By placing the split-ring resonators inside the cavity of the rectangular waveguide, the energy reflected from and transmitted through them are collected at either ends of the waveguide for analysis. By setting the VNA's planes of calibration at the ends of the waveguide, the waveguide channel together with the split-ring resonators inside it become the DUT.

The modes permitted by a rectangular waveguide are quite different from the coaxial cable modes. Therefore, coaxial to WR137 waveguide adaptors are used to connect the coaxial cables from the VNA to the waveguide for mode conversion. The rectangular waveguide permits several propagating transverse electric and magnetic modes, each of which has a cut-off frequency below which the electromagnetic transmission of that

mode is prohibited through the waveguide. The cut-off frequency for the transverse electric mode $\mathbf{TE}_{mn}$ of the waveguide is determined as,

$$f_c = \frac{c}{2\pi}\sqrt{\left(\frac{m\pi}{a}\right)^2 + \left(\frac{n\pi}{b}\right)^2} \tag{3.2}$$

where c is the speed of light, a and b are the length and breadth of the rectangular waveguide's cross-section as marked in figure 3.4a, m and n can take positive integer values or 0 denoting the number of half wavelengths of the mode's field components that can fit in the x and y directions (for axes see figure 3.4) [119]. m and n of a mode are never simultaneously 0.

For the analyses in this thesis, the rectangular waveguide WR137 (as per the Electronic Industries Alliance) was chosen with dimensions, $a = 34.9$ mm and $b = 15.8$ mm. Only the TE_{10} fundamental transverse electric mode of the waveguide is used for the study, which is ideal for exciting the resonances in split-ring meta-atoms placed at the centre of the waveguide cross-section. The propagating electromagnetic waves inside the waveguide scatter off the coupled split-ring resonators and carry information about their resonant response to both ends of the waveguide to be recorded by the VNA. From equation (3.2), it is straightforward to determine that by setting $m = 1, n = 0$ and for the given value of a, the cut-off frequency corresponds to the longest half-wavelength that can fit across the horizontal cross-section of the waveguide. The cut-off frequency of the TE_{10} mode is thus determined to be 4.3010 GHz. The commercial operational frequency band of the fundamental mode is set between 5.85 GHz and 8.2 GHz (the C-band according to IEEE standards) due to excessive absorptive losses within the guide close to this cutoff. The next higher propagating mode in the waveguide is TE_{20} with its lower cut-off at 8.6 GHz.

The instantaneous electric and magnetic field distributions corresponding to the TE_{10} fundamental mode at 6.5 GHz are shown in figures 3.4a and 3.4b, respectively. As can be seen from the figures, the three field components associated with the fundamental waveguide mode TE_{10} are E_y, H_x and H_z. The y-component of the electric field is strongest at the centre of the waveguide cross-section, gradually falling off sinusoidally to zero at the metallic side walls, as dictated by the boundary conditions. The waveguide thus fits one half wave of the electric field component along the x-direction. The field amplitude at a given instant varies sinusoidally along the z-direction, the direction of wave propagation. The magnetic field strength as seen at the front face of figure 3.4b is constant in the y-direction. The magnetic field at the centre of the waveguide cross-section consists only of the H_x component with its strength varying

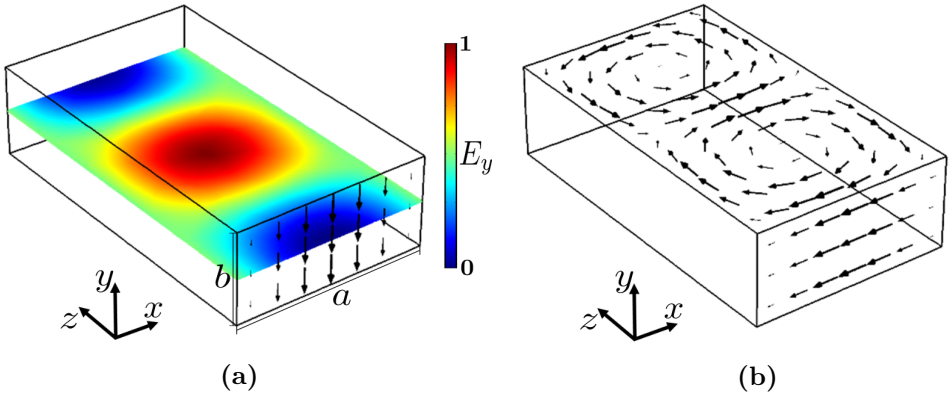

Figure 3.4: The electric (a) and magnetic (b) field distributions corresponding to the TE_{10} fundamental propagating mode of the rectangular waveguide WR137, as computed by finite element modelling software COMSOL at a frequency of 6.5 GHz. The field quantities are instantaneous and the figures show instants in the phase cycle when each of the field components is the strongest at the front face of the waveguide. (a) The black arrows at the front face of the waveguide show the distribution and field strength of the dominant E_y field component across the waveguide's cross-section. The xz-slice with the colour map at the centre of the waveguide shows the distribution of the instantaneous E_y field component both across the waveguide and along the length of it. The colour bar conveys the normalised E_y field strength. (b) The black arrows on the front face show the instantaneous magnetic field strength across the waveguide's cross-section. The magnetic field distribution in the waveguide is best represented as a vector plot on an xz-slice. The dominant field components of the TE_{10} fundamental mode are E_y, H_x and H_z.

sinusoidally along the z-direction like the electric field component. The magnetic field moving away from the centre towards the side walls is a combination of both H_x and H_z components with the H_z being the dominant component at the walls. A SRR's orientation inside the waveguide can be suitably changed with respect to the field components to excite it electrically or magnetically or as a combination of both [74].

The presence of the metallic boundaries causes the wavelength of the electromagnetic wave to be longer inside the waveguide compared to its free-space wavelength. The guide wavelength is calculated as,

$$\lambda_g = \frac{\lambda_0}{\sqrt{1 - \left(\frac{f_c}{f}\right)^2}} \tag{3.3}$$

where f_c is the waveguide's cut-off frequency from equation (3.2), f is the frequency of the propagating mode, and λ_0 is the free-space wavelength of the electromagnetic wave [119]. From equation (3.3), one can verify that for a frequency below cut-off, the guide wavelength is a purely imaginary number indicating exponentially decaying waves in

the waveguide. For frequencies above cut-off, the waves have propagating nature. A detailed mathematical treatment of the rectangular waveguide is presented later, in section 3.7.1.

3.3.4 Near-field measurements

How strongly a metamaterial interacts with free-space radiation depends on the field distribution associated with its resonant modes. Depending on the meta-atom's geometry, the symmetry of the field distribution associated with a mode may prevent its excitation via radiation. Such a metamaterial is very weakly coupled to free-space electromagnetic radiation. The metamaterial then needs to be characterised alternatively by near-field excitation and detection with the aid of near-field antennas and probes. The near-field antennas are connected to the ends of the coaxial cables. The adaptors interfacing the two are of coaxial type and conduct the TEM coaxial mode directly to the near-field antennas. The near-field antennas serve as extensions to the coaxial cables with their outer metallic sheath and the inner dielectric material stripped away.

The commercial coaxial cables and adaptors have a characteristic impedance of 50 Ω. The near-field antennas do not radiate as efficiently as most radio antennas, for the following reasons: (1) the impedance mismatch between the coaxial channel and free-space resulting in a failed mode conversion, (2) the dimensions of the antennas being chosen are intentionally much smaller than the metamaterial dimensions such that their resonance frequencies occur at much higher frequencies than the metamaterial resonances. A near-field antenna driven by the VNA merely facilitates transfer of energy into the highly localised fields of a single meta-atom in the metamaterial. The exponentially decaying near-fields of these antennas couple to the near-fields of the metamaterial, thereby exciting them or detecting their near-fields. However, they also perturb the local field distribution by their presence, becoming a part of the DUT. Since their resonance is significantly different from the metamaterial's resonances, the perturbation is insignificant while characterising the metamaterial's response.

The exposed inner conductor of the coaxial adaptor is suitably modified to act as an electric or a magnetic near-field source. The loop antenna is created by twisting the central coaxial conductor to form a loop which is physically grounded to the outer metal sheath. The alternating current driven in this closed metallic loop gives rise to a magnetic dipole moment making it a magnetic near-field source. In the case of the coaxial dipole probe, the outer sheath automatically acts as a ground plane to the central conductor, therefore physical grounding is not required. The exposed central

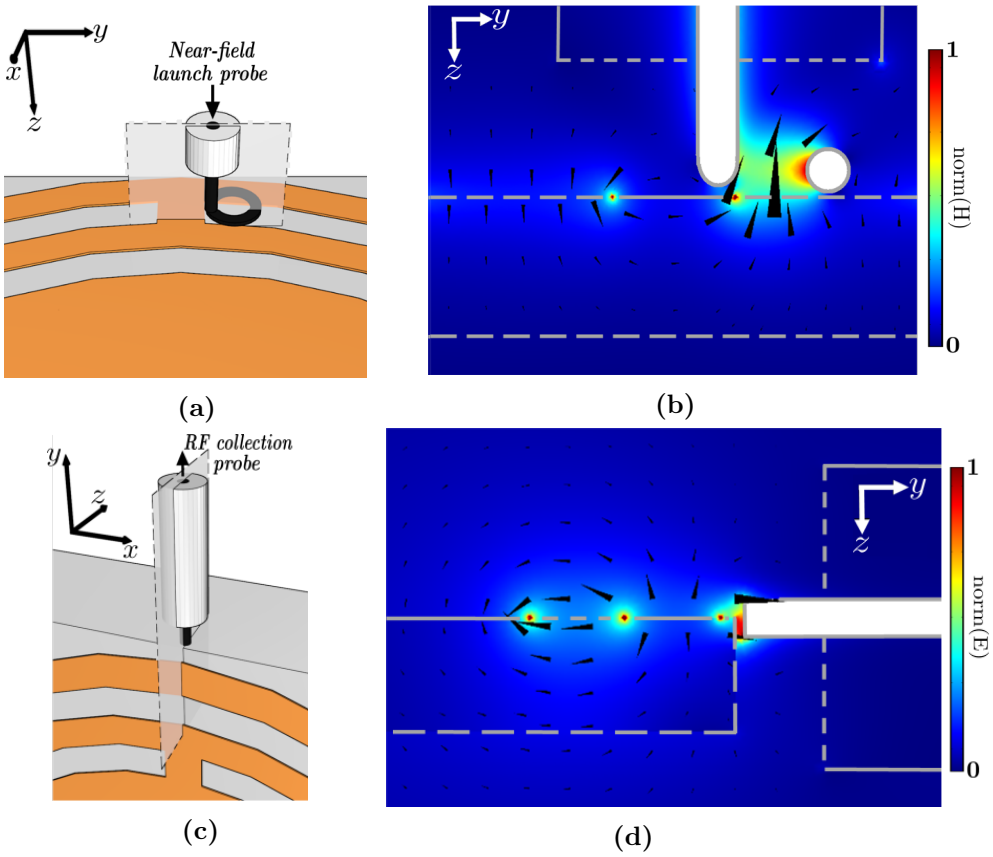

Figure 3.5: Schematic of a complementary split-ring resonator (CSRR) meta-atom being excited by a loop antenna (a) and its near-field probed by a stripped coaxial dipole antenna (c). (b) yz-slice through the centre of the loop antenna showing the near-field excitation of the meta-atom's resonant mode. The colour map represents the normalised magnetic field norm and the black arrow heads are vectors representing the instantaneous magnetic field distribution on the map. (c) yz-slice showing the electric near-field of the meta-atom probed by the coaxial dipole's tip. The colour map shows the normalised electric field norm and the black arrow heads represent the instantaneous electric field distribution on the map.

conductor is a half-wave dipole antenna. At the studied frequencies, which are much lower than its resonance frequency, the coaxial dipole antenna merely acts as an electric near-field source. The polarisation of the electric field component below the coaxial tip is tangential to the antenna and couples efficiently to the metamaterial's electric near-field that has the same polarisation.

To demonstrate the function of the near-field antennas, consider the example shown in figure 3.5. Figures 3.5a and 3.5c show a close-up of a complementary split-ring resonator (CSRR) meta-atom excited by a loop antenna and its excited resonance being detected via a coaxial dipole, respectively. The coaxial dipole here functions as a

probe that collects the electric near-field. This situation is simulated through the finite element field solver in COMSOL Multiphysics, with the meta-atom's fundamental resonance being excited at 1.9 GHz. Two yz-planes (with dotted edges) are shown one each in figures 3.5a and 3.5c through the coaxial antennas' central conductors. Figures 3.5b and 3.5d show respectively the magnetic field distribution and the electric field distribution in the cut-planes of figures 3.5a and 3.5c. The axes directions are also marked for easy identification of the plot orientations with respect to figures 3.5a and 3.5c.

Figure 3.5b represents the yz-plane cutting through the loop antenna to the other side of the plastic substrate containing the meta-atom in figure 3.5a. The metallic boundaries are shown by solid grey lines while other boundaries such as the coaxial end plane and the plastic substrate are marked with dotted grey lines. The colour plot shows the normalised magnetic field strength in the cut-plane. The black arrow heads show the direction of the instantaneous magnetic field in that plane, with their sizes scaled according to field magnitude. The arrows show that the strongest magnetic field magnitude is seen to be at the centre of the loop, which is the position of the loop antenna's magnetic dipole. The magnetic dipole has a z-polarisation normal to the plane of the loop and the meta-atom. The position of the loop antenna is adjusted with respect to the meta-atom for optimum coupling of the antenna's magnetic near-field to the out-of-plane magnetic field component in the meta-atom. The magnetic field strength as seen from the colour plot is strongly localised close to the metal wire of the loop (grey circle) and at the edges of the metal strip in the meta-atom.

Figure 3.5d represents the yz-plane cutting through the coaxial detection probe into the top portion of the meta-atom in figure 3.5c. The solid and dotted grey lines represent the same boundaries as in figure 3.5b. The colour plot here shows the normalised electric field strength in the cut-plane. The black arrow heads show the direction of the electric field, with their sizes scaled according to the field magnitude. The electric field associated with the excited resonance in this example has a dominant electric field contribution from the y-component of the field, as can be seen from the black arrows of figure 3.5d. The strongest electric field localisation is at the edges of the meta-atom's metallic regions. A very strong near-field coupling is achieved by positioning the probe tangential to the direction of polarisation of the meta-atom's electric near-field (y-direction in figure 3.5d), which is the optimum position for near-field detection in this case.

3.4 Numerical simulations - Finite Element Method

Throughout this thesis, a numerical technique called the Finite Element Method (FEM) is used to design and test the electromagnetic response of metamaterial systems, to simulate experimental conditions and understand metamaterial systems better, and to validate the experimental results. The commercial FEM software COMSOL Multiphysics is used. COMSOL solves the time-harmonic electromagnetic wave equation by implementing Maxwell's equations depending on the material properties and the geometry used in the models. It employs several *boundary conditions* to help describe the geometric entities in the modelled system. A full description of COMSOL's working is beyond the scope of discussion in this thesis. The most relevant boundary conditions of COMSOL used in the modelling of metamaterial systems in this thesis are discussed in this section, followed by some brief comments on meshing.

3.4.1 Perfect Electric Conductor (PEC)

The microwave metamaterial systems that are analysed in this thesis have a high composition of metals. The metamaterials studied are metallic resonators that act as good reflectors of (microwave) electromagnetic radiation, especially close to their resonance. Metals are such good conductors at GHz frequencies, that an electromagnetic wave penetrates only a very small distance into metals. This penetration distance is quantified by the term *skin depth* and is a measure of how far the wave penetrates a conductor's surface before attenuating to $1/e$ times its original value [120]. At the GHz frequencies, the skin depth of copper is as small as 2.07 μm at 1 GHz and 0.654 μm at 10 GHz, which are at least 10 times smaller than the thickness of the studied metallic structures. The rectangular waveguide used for the experimental work in this thesis is made of aluminium which has a skin depth of 2.59 μm at 1 GHz and 0.819 μm at 10 GHz. The large impedance mismatch with any bounding dielectric ensures that only a small proportion of the fields exists within the metal. Therefore, a good approximation can be achieved using the idealised perfect electric conductor (PEC) boundary condition in COMSOL, which models the metallic boundaries as lossless surfaces. The PEC boundary condition sets the tangential component of the electric field to zero at the boundary through

$$\mathbf{n} \times \mathbf{E} = 0 \tag{3.4}$$

where $\mathbf{n}$ is the unit vector normal to the boundary and $\mathbf{E}$ is any component of electric field tangential to the boundary. Figure 3.6a shows an example of a frequency

domain COMSOL model that analyses the frequency dependent scattering parameters (to compare to the experimental data recorded with a VNA) of a single SRR. The PEC boundary condition has been applied to the four walls of the rectangular waveguide. Metallic resonators, for example, a single SRR in figure 3.6a placed inside the waveguide to be analysed are also chosen to be PEC boundaries.

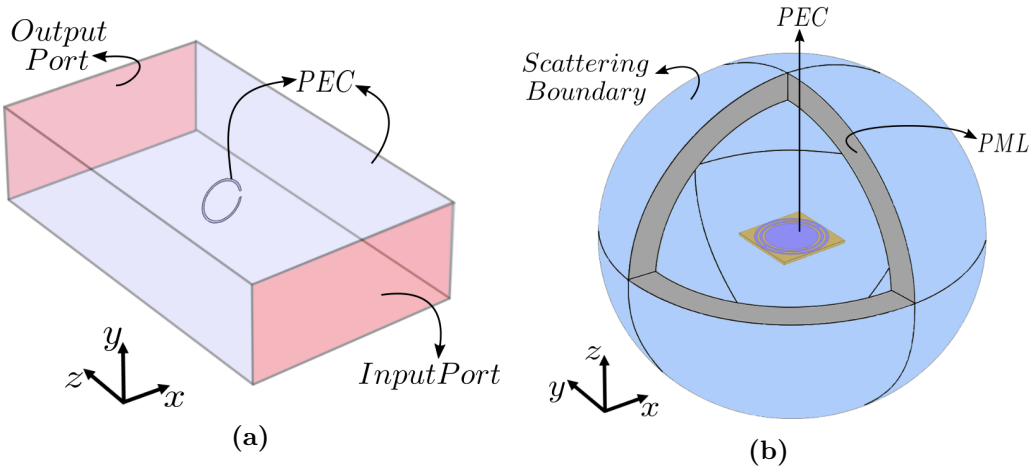

Figure 3.6: (a) Schematic taken from a source driven COMSOL model to calculate the reflectivity and transmissivity of a single SRR. The perfect electric conductor (PEC) boundaries (waveguide walls and the SRR) are highlighted using a faint blue colour. The input and output rectangular ports at the ends of the rectangular waveguide are highlighted here by a light red colour. (b) Snapshot from a COMSOL eigenmode model to compute the eigenmode frequencies of a CSRR meta-atom resting on a plastic substrate. The meta-atom is assigned a PEC boundary condition (dark blue colour). The meta-atom is surrounded by a spherical scattering boundary highlighted in light blue and a perfectly matched layer (PML), highlighted in grey. A section of the spherical scattering boundary and the PML have been removed to reveal the meta-atom at the centre.

3.4.2 Impedance Boundary Condition (IBC)

As mentioned above, the skin depth of metals at microwave frequencies are only a few microns. Compared to the millimetre sized meta-atoms in this frequency regime, the skin depth is quite small. In computations where the attenuation in the medium is important, the perfect electric conductor is not the ideal choice of a boundary condition for metals. Though there are electric currents flowing inside of the metal object, the skin effect drives them to the surface. Therefore, for the purpose of modelling only the surface electric currents are considered. The impedance boundary condition (IBC) is used at boundaries where the skin depth is small, like metals at microwave frequencies. The IBC allows to avoid modelling Maxwells equations in the interior of any metallic objects by assuming that the currents flow entirely on the surface. The IBC can be

employed when computing losses due to the metal's finite conductivity.

3.4.3 Ports

A port in a FEM model is a boundary where the electromagnetic energy enters or leaves the system. The example in figure 3.6a shows two rectangular ports set at the ends of the rectangular waveguide. For simulations done for this thesis, the input port is set to launch the TE_{10} mode of the waveguide and absorb the electromagnetic energy that is reflected back by the resonator(s) into the TE_{10} waveguide mode. The output port at the other end of the waveguide is a listener port, which collects the electromagnetic energy in the TE_{10} mode that is transmitted through the resonator(s). The ports support the calculation of S-parameters that can be compared to those recorded experimentally using a VNA. In order to account for any energy scattered by the resonators into higher order waveguide modes, an additional port that collects higher order modes can be assigned to the same boundaries that act as the input and output ports. In the example of figure 3.5, where a single CSRR meta-atom was characterised using near-field coaxial type antennas, the input and output ports of coaxial type were set at the ends of the coaxial cables that connected into the loop and the coaxial dipole antennas, respectively.

3.4.4 Domain truncation

When the modelled system is closed such as a rectangular waveguide, the boundary conditions that were discussed so far are sufficient. When a metamaterial is to be modelled in free-space, an additional boundary needs to be defined around the modelled system to truncate the infinitely large modelling domain to a finite one to be solved using FEM. The truncated domain is a sufficiently accurate approximation of free space. This outer boundary, where the scattering boundary condition (SBC) is applied, absorbs electromagnetic radiation scattered by the analysed system and is ideally non-reflecting. In practice, the first-order scattering boundary in COMSOL is a good absorber for normally incident radiation, partially reflecting for other incidence angles and almost completely reflecting as an incoming wave approaches grazing incidence. Figure 3.6b shows a snapshot from an eigenmode model (no ports required) in COMSOL where the eigenfrequencies of a CSRR meta-atom resting on a plastic substrate, are computed. The most appropriate shape for the scattering boundary in this case is a sphere, shown in light blue in the figure. The spherical scattering boundary is chosen big enough (typically with a radius of the order of the meta-atom's expected resonance wavelength) so as not to perturb the meta-atom's near-fields. An additional spherical domain shown in grey in figure 3.6b, is included within the scattering boundary. While

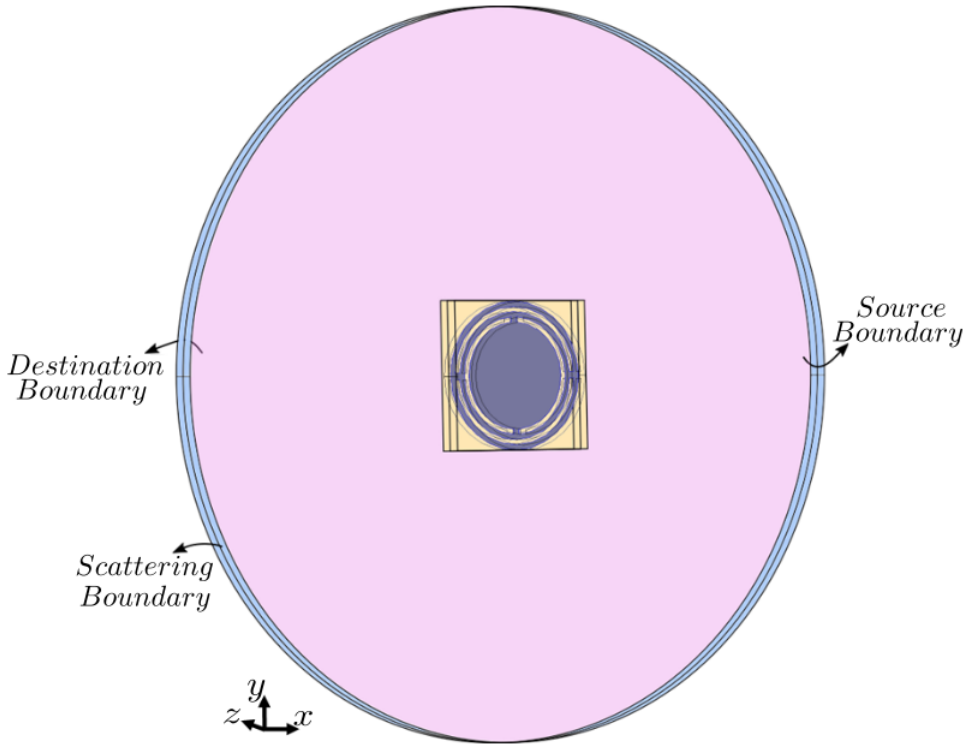

Figure 3.7: Snapshot from a COMSOL eigenmode model to compute the eigenmode frequencies of a 1D periodic metamaterial medium constructed from CSRR meta-atoms. The unit cell of the periodic medium is the meta-atom seen at the centre of the model embedded in a substrate material (yellow). The meta-atom is surrounded by a cylindrical scattering boundary highlighted in light blue. To simulate an infinitely periodic medium in the z-direction, a periodic boundary condition is set up between the circular source boundary at the front of the model and the circular destination boundary (shown in pink) at the back.

not a boundary condition, this perfectly matched layer (PML) is a domain that acts like an absorbing material for outgoing electromagnetic waves and any waves reflected back from the scattering boundary. Only a SBC or a PML needs to be used in a COMSOL model, as they both serve the purpose of domain truncation and absorption of scattered waves. However, neither of them are perfect absorbers. In models where it is crucial to avoid perturbation due to scattered waves, both the SBC and the PML can be used together as shown in figure 3.6b.

3.4.5 Periodic boundary condition - Floquet periodicity

Periodic boundary conditions are frequently used in the field of metamaterials for the computation of eigenfrequencies or S-parameters in periodic media. Consider for example, the snapshot from a COMSOL model shown in figure 3.7. The eigenmode model simulates a 1D stacked metamaterial whose band structure is to be computed.

The metamaterial structure is modelled using a Floquet-periodic boundary condition on the circular boundaries at the front (transparent) and back (pink coloured) of the meta-atom to simulate a periodic medium along the z-direction, as shown. The two boundaries are identified as the source and destination boundaries and a Bloch-Floquet periodicity is setup between the boundaries depending on the wavevector specified in the model. Thus, the eigenfrequency-wavevector ($\omega - k$) relationship of any supported modes can be determined.

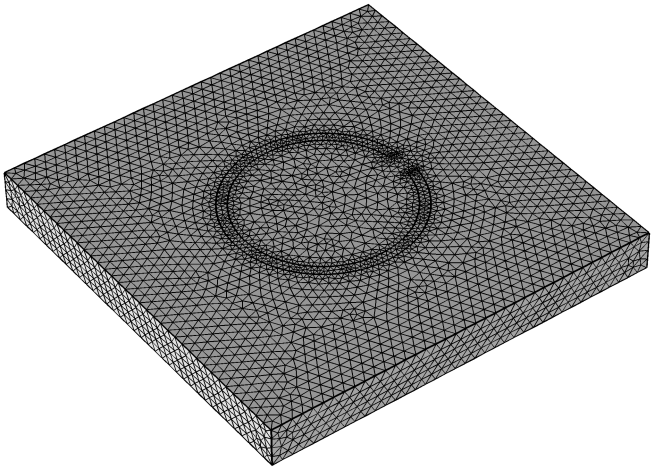

Figure 3.8: A meshing example showing a split-ring resonator on a small block of substrate, meshed with tetrahedral elements. The density of meshing can be tailored throughout the geometry according to the gradient of the fields.

3.4.6 Meshing

Once the model is constructed in COMSOL and all the appropriate boundary conditions applied, the geometry is discretised into finite mesh elements (from where the modelling method gets its name). Maxwell's equations are solved at the nodes of the mesh elements with the appropriate boundary conditions taken into account. Figure 3.8 shows a portion of the geometry from an eigenmode model to compute the eigenfrequencies of a split-ring resonator, meshed using tetrahedral elements. The rest of the geometry would normally consist of a scattering boundary at least a single resonance wavelength (expected fundamental resonance wavelength of the resonator) away, as seen in figure 3.6b. The spherical medium surrounding the analysed resonator is also meshed with tetrahedral mesh elements, but is not shown in figure 3.8. The accuracy of the results can be improved by tailoring the mesh density throughout the model geometry to include more mesh elements in regions of high field gradient. Discretising the geometry in FEM facilitates approximating the partial differential equations

to be solved into a matrix form, which are then solved using matrix decomposition algorithms. Refining the mesh through repeated convergence tests on the calculated field parameters ensures that the solution has minimal error.

3.5 Fourier Transform and Reciprocal space

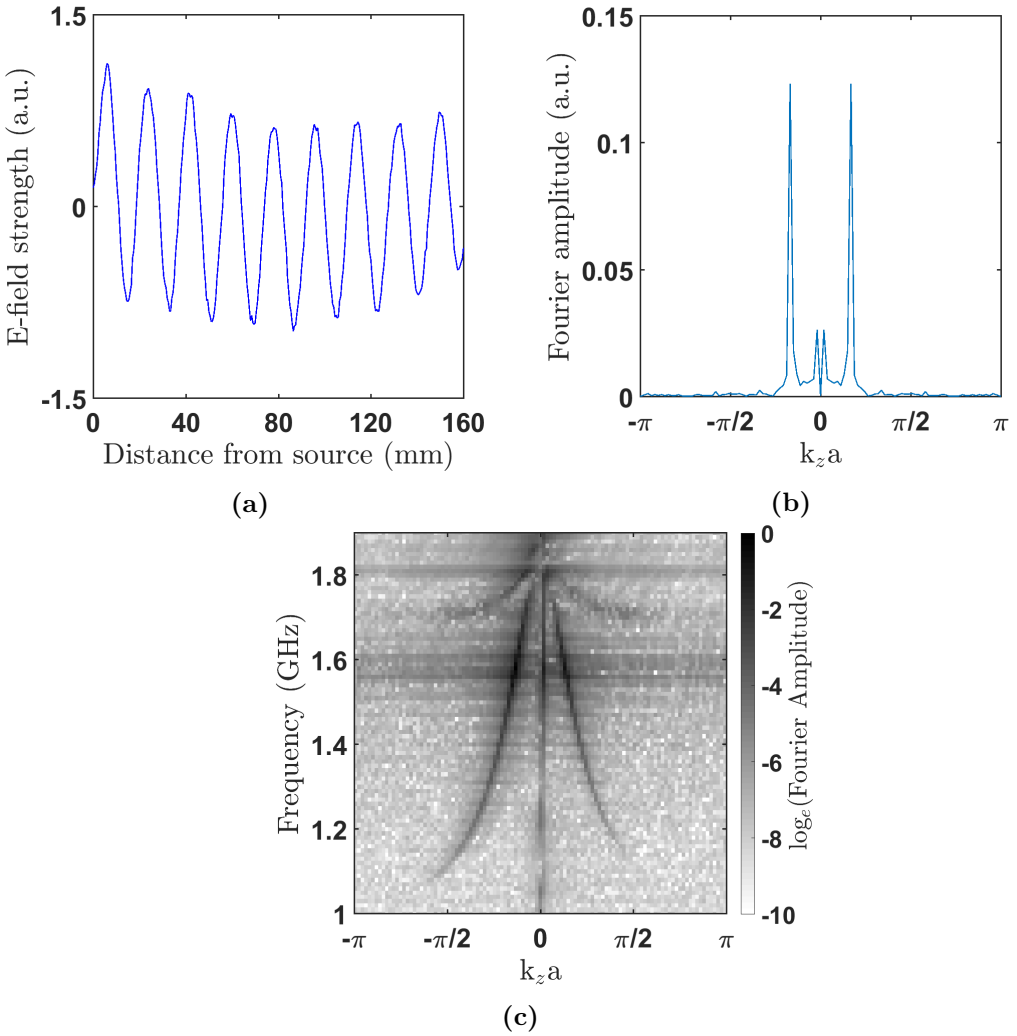

Figure 3.9: The 1D Fourier transform of experimentally determined instantaneous field profile at a given frequency of a 1D metamaterial in (a) gives the strength of the frequency component as a function of wavevector in the metamaterial as shown in (b). (c) Stacking these plots as a function of frequency helps construct the dispersion diagram showing the $\omega - k$ relationship in the metamaterial.

In this thesis, chapters 5 and 6 deal with the design, fabrication and experimental

characterisation of 1D metamaterials. The characterisation is performed using near-field antennas which excite the near-field of the resonant modes in the metamaterial, and probe the near-field to collect and construct a spatial field map. Figure 3.9a shows a sample of an electric field map probed in the near-field of a 1D metamaterial for a single frequency, where the real part of the instantaneous electric field amplitude is plotted. The use of Fourier transform in signal processing is to analyse a small window of a time varying signal to determine the frequency of the signal. In our experiments, since the input frequency used to excite the metamaterials is known information, the Fourier transform is applied to the spatial field maps like that shown in figure 3.9a. The figure 3.9b shows the outcome of the Fourier transform applied on the finite window of the 1D electric field map from figure 3.9a and a subsequent 'fft-shift' that centres the origin with respect to the wavevectors in the reciprocal space. Repeating this process as a function of frequency helps determine the dispersion relationship $\omega - k$ of the analysed metamaterial, as shown in figure 3.9c. The wavevector along the x-axis of the plot is labelled k_z because the direction along the 1D metamaterial is treated as the z-direction, a is the periodicity of the metamaterial. More specific discussion related to these plots can be found in chapter 5.

The relationship between the spatial points at which the data is recorded and the transformation into the reciprocal space is as follows: the real space co-ordinates in which the data is recorded is given in a sequence as $[0, \Delta x, \cdots, (N-1)\Delta x]$, where Δx is the resolution with which the data is collected in real space. $(N-1)\Delta x = L$ is the total scan length, which is usually the length of the sample. These points are mapped onto the reciprocal space as below,

$$[-k_{max}, -k_{max} + \Delta k, \cdots, 0, \cdots, k_{max} + \Delta k, k_{max}] \; for \; even \; N \tag{3.5}$$

$$[-(k_{max} - \frac{\Delta k}{2}), -(k_{max} - \frac{\Delta k}{2}) + \Delta k, \cdots, 0, \cdots, (k_{max} - \frac{\Delta k}{2}) + \Delta k, (k_{max} - \frac{\Delta k}{2})] \; for \; odd \; N \tag{3.6}$$

where $k_{max} = \frac{\pi}{\Delta x}$ and $\Delta k = \frac{2\pi}{L + \Delta x}$ are the maximum wavevector (the Brillouin zone boundary) and the resolution obtainable in wavevector in the reciprocal space as a result of the Fourier transform, respectively. As can be seen, the resolution in real space and that in k-space do not have a direct relationship. The length of the scan determines the resolution in k-space. The Brillouin zone boundary is set at $k_{max} = \frac{\pi}{a}$, where a is the periodicity of the metamaterial or in other words the size of a single unit cell in the metamaterial.

As seen from figure 3.9b, the wavevector spans along both the positive and the negative directions. In real space, it indicates the directions along the length of the sample. The two tall peaks seen mirrored in figure 3.9b are the strengths of the frequency component analysed in the forward and the backward direction in the sample i.e. the signal propagating in the metamaterial away from the source and the signal reflected back from the end of the metamaterial. Two small peaks are visible close to the origin on the plot, corresponding to a wavevector which falls on the light line. The small detected signal at this frequency is a consequence of direct free-space interaction between the source antenna and the probe. The advantage of using the Fourier transform is that the frequency components due to the resonant mode of the metamaterial and that due to the antennas are isolated. It is to be expected that the Fourier peaks seen in figure 3.9b would have finite width as a consequence of attenuation. However, it can also be noticed that there are non-zero ripple like features at some of the other wavevectors. This is a consequence of the effect called 'spectral leakage' [121, 122], where the Fast Fourier Transform (FFT) of the MATLAB software treats the input signal as if it is a small window of an infinitely repeating waveform. For a finite-sized analysed sample, the FFT function repeats the recorded field map to treat it as an infinitely repeating pattern. Therefore, the discontinuity created by 'stitching' the field values at the ends of the sample results in a phenomenon called the 'spectral leakage', giving rise to peaks at wavevectors that are not physically present in the analysed system. It can be seen from figure 3.9c that these ripples are present at almost all the frequency components and this is unavoidable due to the finiteness of the analysed metamaterial samples.

3.6 Attenuation in metamaterial waveguides

In chapters 5 and 6, new meta-atoms are proposed to develop novel metamaterial waveguides. The physics of metamaterial waveguides based on magneto- and electro-inductive coupling was discussed in the chapter 2 along with relevant background literature. In chapter 5, we propose a meta-atom to use a building block for an ultra-wideband metamaterial waveguide, that improves over current metamaterial waveguides in terms of operational bandwidth. It would also be beneficial to estimate its attenuation to compare its losses with other metamaterial waveguides. The metamaterial waveguide in chapter 6 permits simultaneous forward and backward propagating waves via two non-interfering resonances, in an overlapping frequency band. Even for this case, an estimate of attenuation associated with the forward and backward propagating waves is beneficial for tuning the metamaterial response suitably.

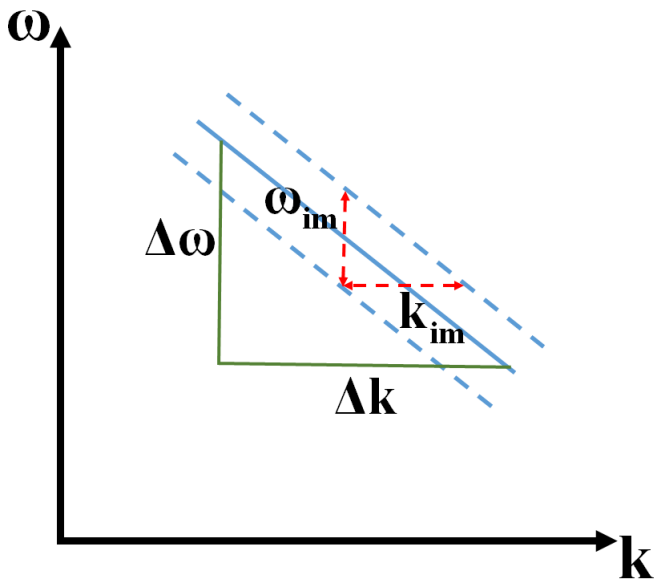

Figure 3.10: A sample representation of a $\omega - k$ relationship is shown. The group velocity of the dispersive mode can be calculated from its gradient. The group velocity can also be related to the imaginary parts of the frequency (f_{im}) and the wavevector (k_{im}) by determining the widths of the mode along the two axis directions.

Figure 3.10 is a rough representation of a dispersion plot showing the $\omega - k$ relationship of a negatively dispersive material. The plot can be considered to represent a zoomed in section of the dispersion in figure 3.9c where the gradient of the dispersion is linear. The phase velocity (ν_p) of the waves in the metamaterial medium is determined directly using the relationship,

$$\nu_p = \frac{\omega}{k} \tag{3.7}$$

where k representd the phase constant k_p. The group velocity ν_g which represents the velocity of power transfer in the metamaterial is given by the first differential of ω with respect to k as,

$$\nu_g = \frac{\Delta\omega}{\Delta k} \tag{3.8}$$

where for the purpose of estimating the group velocity, $\Delta\omega$ and Δk can be determined directly from the dispersion as shown in figure 3.10. Interestingly, the loss/attenuation in the medium can also be estimated from a similar relationship. As mentioned already, the x-axis in figure 3.10 comprises of real values of wavevector, which is the phase constant k_p discussed in chapter 2. It was also previously mentioned that the propagation constant $\gamma = k_a + ik_p$, where k_a is the attenuation. The magnitude of k_a has a direct relationship with how broad the mode is. In figure 3.10, the width of the

observed mode along the x-axis direction is represented by k_{im} which is nothing but k_a. The width along the y-axis direction is represented by ω_{im}. Assuming that the data points have been determined with a sufficiently high resolution to accurately portray the widths of the resonant mode along the two axis directions, the group velocity can also be expressed as,

$$\nu_g = \frac{\omega_{im}}{k_{im}} \tag{3.9}$$

While the value of k_a (or k_{im}) representing the attenuation should be directly calculable from the experimentally constructed dispersion diagram, the finiteness of the sample affects the minimum resolution achievable, as can be seen from the Fourier transformed data in figure 3.9b. This prevents an accurate experimental determination of the attenuation of the system. The lengths of the metamaterial samples demonstrated are typically 300 mm or less. While this is sufficient to successfully characterise and establish its dispersion with sufficient resolution as seen in figure 3.9c, it is difficult to establish the attenuation in length scales of metres, as is conventionally done.

In this thesis, to estimate the attenuation of the metamaterial waveguides, an indirect modelling is approach is followed. The eigensolver in COMSOL Multiphysics computes eigenvalues as complex quantities to express both the eigenfrequency and the losses associated with it. The dielectric losses can be accounted for by including the loss tangent values in the material properties. The perfect electric conductor boundaries for the metals are replaced by impedance boundary conditions to add the appropriate metal's material properties and finite conductivity. Referring back to equation (3.8), the group velocity is first calculated from the computed real values of frequency and the phase constant. Once the imaginary part of the eigenfrequency is extracted from the eigenmode solver, it is a straightforward step to determine k_a. The expression used to convert this k_a from the units of m^{-1} to the conventionally used dB/m is,

$$k_{a[dB/m]} = k_{a[1/m]} \frac{10}{log_e(10)} = 4.343 * k_{a[1/m]} \tag{3.10}$$

which is used in chapters 5 and 6 to convert the attenuation determined from the numerical computation to the conventional unit of dB/m.

3.7 Analytical modelling

The analytical model that was developed to predict the resonance frequencies of a coupled bianisotropic dimer analysed inside a rectangular waveguide is presented here.

The analytical model is used in chapter 4 (section 4.4) where the electromagnetic interactions in a pair of coupled split-ring resonators are studied.

3.7.1 Green's function of a rectangular waveguide

The discussion on the fundamental propagating mode of the rectangular waveguide along with the field profiles was presented in section 3.3.3. In this section, the derivation of the waveguide's Green's functions are presented. While characterising the field interactions between resonators in the cavity of the waveguide theoretically, the first key step is to derive the Green's function of the medium in which the interactions take place.

The Green's functions for studying electromagnetic interactions in free space have been discussed in detail in many past works [71, 123]. The current discussion begins from the free space Green's function and proceeds to deriving it for the rectangular waveguide, by imposing the appropriate boundary conditions. Let a scalar potential ϕ and a vector potential $\mathbf{A}$ of the electromagnetic field be defined first, describing the electrostatic interactions between electric charges and the dynamic interactions between the electric currents of the resonators, respectively. In the Lorenz gauge, the scalar and the vector potentials of the electromagnetic field satisfy the Helmholtz equation

$$\begin{aligned} \left[\nabla^2 + k_0^2\right] \phi &= -\frac{\rho(\mathbf{r})}{\epsilon_0} \\ \left[\nabla^2 + k_0^2\right] \mathbf{A} &= -\mu_0 \mathbf{J}(\mathbf{r}) \end{aligned} \tag{3.11}$$

The corresponding free-space scalar and tensor Green's functions are

$$\begin{aligned} g(\mathbf{r}, \mathbf{r}') &= \frac{e^{ik_0|\mathbf{r}-\mathbf{r}'|}}{4\pi|\mathbf{r}-\mathbf{r}'|} \\ \underline{\underline{G}}(\mathbf{r}, \mathbf{r}') &= \frac{e^{ik_0|\mathbf{r}-\mathbf{r}'|}}{4\pi|\mathbf{r}-\mathbf{r}'|}\mathbf{I} \end{aligned} \tag{3.12}$$

where the boundary is set at ∞, $\mathbf{I}$ is the unit tensor and $k_0 = \frac{\omega}{c}$, with ω being the free space angular frequency. Since the wave is confined inside a rectangular waveguide, the boundary is deformed from infinity to the metallic walls of the rectangular waveguide. Let the origin be set at one of the corners of the waveguide's cross-section. The radiation is confined to $0 < x < a$, $0 < y < b$ and is infinitely extended in the z-direction. For the directions of the axes, refer to figure 3.4. The walls of the waveguide are modelled as Perfect Electric Conductors (PEC), so the continuity of the tangential component

of the electric field across the boundary may be written as

$$\mathbf{n} \times \mathbf{E} = 0 \qquad \text{on the boundaries} \tag{3.13}$$

In terms of the vector potential in the Lorenz gauge

$$\mathbf{n} \times (k_0^2 \mathbf{A} + \nabla(\nabla \cdot \mathbf{A})) = 0 \qquad \text{on the boundaries} \tag{3.14}$$

As a result of the isotropy of the dielectric and the rectangular geometry of the waveguide, the Green's tensor will be diagonal in Cartesian coordinates. Hence equation (3.14) leads to the following boundary conditions at the waveguide walls

$$\begin{aligned} G_{xx}|_{y=0,b} &= 0 \\ \frac{\partial}{\partial x} G_{xx}\Big|_{x=0,a} &= 0 \\ G_{yy}|_{x=0,a} &= 0 \\ \frac{\partial}{\partial y} G_{yy}\Big|_{y=0,b} &= 0 \\ G_{zz}|_{x=0,a} &= 0 \\ G_{zz}|_{y=0,b} &= 0 \\ g|_{x=0,a} &= 0 \\ g|_{y=0,b} &= 0 \end{aligned} \tag{3.15}$$

Such boundary value problems admit unique solutions. Therefore, since g satisfies the same Helmholtz equation and the same boundary conditions as G_{zz}, they will be the same, $g = G_{zz}$.

Applying these boundary conditions to the Helmholtz equation of the Green's tensor

$$\left[\nabla^2 + k_0^2\right] G_{r_i r_i}(\mathbf{r}, \mathbf{r}') = -\delta(\mathbf{r} - \mathbf{r}') \tag{3.16}$$

the final Green's tensor components can be readily obtained as

$$\begin{aligned}
G_{xx} &= \sum_{m=0}^{\infty}\sum_{n=1}^{\infty} i\frac{\epsilon_m\epsilon_n}{2abk_I}\cos\left(\frac{m\pi x'}{a}\right)\sin\left(\frac{n\pi y'}{b}\right)\cdot \\
&\quad \cos\left(\frac{m\pi x}{a}\right)\sin\left(\frac{n\pi y}{b}\right)e^{ik_I|z-z'|} \\
G_{yy} &= \sum_{m=1}^{\infty}\sum_{n=0}^{\infty} i\frac{\epsilon_m\epsilon_n}{2abk_I}\sin\left(\frac{m\pi x'}{a}\right)\cos\left(\frac{n\pi y'}{b}\right)\cdot \\
&\quad \sin\left(\frac{m\pi x}{a}\right)\cos\left(\frac{n\pi y}{b}\right)e^{ik_I|z-z'|} \\
G_{zz} &= \sum_{m=1}^{\infty}\sum_{n=1}^{\infty} i\frac{\epsilon_m\epsilon_n}{2abk_I}\sin\left(\frac{m\pi x'}{a}\right)\sin\left(\frac{n\pi y'}{b}\right)\cdot \\
&\quad \sin\left(\frac{m\pi x}{a}\right)\sin\left(\frac{n\pi y}{b}\right)e^{ik_I|z-z'|}
\end{aligned} \tag{3.17}$$

where

$$\epsilon_m = \begin{cases} 1 & m = 0 \\ 2 & m > 0 \end{cases} \tag{3.18}$$

and k_I is the propagating component of the wave-vector given by

$$k_I^2 = k_0^2 - \left(\frac{m\pi}{a}\right)^2 - \left(\frac{n\pi}{b}\right)^2 \tag{3.19}$$

and m and n are the same non-negative integers from equation (3.2), together describing the different modes that could be accommodated inside the waveguide. Here, $k_0 = \frac{\omega}{c}$ is the free-space wave vector of the incident electromagnetic wave and ω is the corresponding angular frequency. In the analytical model, ω uses the value of the SRRs' natural resonance frequency. This is a natural choice because the strongest excitation of the resonators by the electromagnetic wave and also by each other's radiated fields is achieved at their resonance frequency.

By substitution of numerical values for m and n into equation (3.19), it can be verified that in the specified commercial frequency band of the fundamental TE_{10} mode, only $m = 1,\ n = 0$ gives a real value for the propagation constant. All other combinations of m and n values result in exponentially decaying functions. The energy scattered by the resonators is carried away by the propagating TE_{10} mode. However, the other decaying modes should still be included in the calculations to accurately account for near-field interactions between the resonators, especially at separations smaller than the decay length of these modes. The summations in the expressions for tensor components of the Green's functions in equation (3.19) were calculated iteratively including

the several waveguide modes in the frequency range of 4.5 GHz to 8.5 GHz where the SRR dimer's resonant properties were characterised. A test for convergence of the calculated values was performed in every iteration with a strict tolerance (10^{-6}). The number of modes that needs to be included in the calculations varies as a function of separation between the SRRs.

The charge and current density distributions that need to be input into the analytical model were computed using an eigenmode model in COMSOL Multiphysics. The density of meshing used to compute these parameters also plays an important role in determining the accuracy of the analytical model's results. The smallest separation between two mesh nodes on a SRR should be smaller than the smallest separation between SRRs for which the electromagnetic interaction strength is estimated. At inter-element separations smaller than the diameter of each SRR, the prominent effects of near-field interactions are accounted for by including as many higher order modes of the waveguide as possible to obtain good convergence. For example, in the study of SRR dimers in chapter 4, for the smallest inter-element separation of 0.5 mm between a pair of SRRs, higher order modes up to $m, n = 50, where m = 0, 1, 2, \cdots 50 and n = 0, 1, 2, \cdots 50$ were included to obtain good convergence.

3.7.2 Modelling of meta-atom interactions in the rectangular waveguide

The near- and far-field interactions between a pair of SRRs need to be accurately accounted for to understand the responses of the system for different separations. A complete analytical model is developed to achieve this. The first step is to consider the Lagrangian for a pair of identical lossless resonators, and a complete treatment for their interactions in free space can be found in [71, 123, 124]; here the equations required to implement the model are presented.

The interaction energies between a pair of identical conducting elements arising from their current $W_{J,ij}$ and charge $W_{q,ij}$ distributions are given by,

$$\begin{aligned} W_{J,ij} &= \int d^3\mathbf{r} \int d^3\mathbf{r}' \mu_0 \mathbf{J}^*(\mathbf{r}) \underline{\underline{G}}(\mathbf{r}, \mathbf{r}') \mathbf{J}(\mathbf{r}') \\ W_{q,ij} &= \int d^3\mathbf{r} \int d^3\mathbf{r}' \frac{1}{\epsilon_0} q^*(\mathbf{r}) g(\mathbf{r}, \mathbf{r}') q(\mathbf{r}') \end{aligned} \tag{3.20}$$

where $\mathbf{J}$ and q are the current and charge density distributions of the fundamental eigenmode of a single element (in this work, a single SRR within the waveguide), and

$\underline{\underline{G}}(\mathbf{r}, \mathbf{r}')$ and $g(\mathbf{r}, \mathbf{r}')$ are the tensor Green's and the scalar Green's functions respectively, which were derived in section 3.7.1. When $i = j$, these terms correspond to the self-energies of a single element, and when $i \neq j$ they correspond to mutual-energy terms. The energy term $W_{J,ij}$ is comparable to the inductive energy term in the equivalent circuit approach in ref. [123] (self-inductance when $i = j$ and mutual inductance when $i \neq j$). Similarly, the energy term $W_{q,ij}$ is comparable to the capacitive energy terms (self-capacitance when $i = j$ and mutual capacitance when $i \neq j$).

Since the Green's functions for the rectangular waveguide were already derived in the last sub-section, the resonance frequencies of the symmetric and anti-symmetric modes of a coupled dimer are directly presented, which can be calculated [71] using,

$$\begin{aligned} \omega_s &= \omega_0 \sqrt{\frac{1+\beta}{1+\alpha}}, \\ \omega_{as} &= \omega_0 \sqrt{\frac{1-\beta}{1-\alpha}}, \end{aligned} \tag{3.21}$$

where ω_0 is the angular resonance frequency of a single SRR, and the magnetic (α) and electric (β) interaction constants due to the current and charge distributions respectively are given by [71],

$$\begin{aligned} \alpha &= \frac{W_{J,12}}{W_{J,11}}, \\ \beta &= \frac{W_{q,12}}{W_{q,11}}. \end{aligned} \tag{3.22}$$

The $\mathbf{J}$ and q distributions of the fundamental eigenmode of a single SRR are needed as input for this model. They were calculated using the eigensolver of Comsol Multiphysics.

3.8 Summary

In this chapter, the fabrication procedure for the metamaterial samples, the experimental equipment used to characterise them, and the modelling techniques that are employed to validate, understand or predict the experimental results have been elaborated. Photolithography is the quickest technique to fabricate the metamaterial samples used in the studies of this thesis. The experimental measurements are either performed through closed radiative measurements in a rectangular waveguide or near-

field measurements in free-space to construct a frequency dependent spatial field profile of metamaterials. Analytical modelling is used to accurately predict the resonant mode positions of coupled resonators and to understand the nature of field interactions between the resonators. Where analytical modelling is too tedious to employ or its scope limited, FEM numerical technique is used, for example when spatial field profiles around metamaterials or the dispersion of periodic metamaterials need to be predicted.

Chapter 4

Electromagnetic interactions in coupled split-ring resonators

4.1 Introduction

Split-ring resonators (SRRs) are a fundamental building block of many electromagnetic metamaterials. Metamaterial composites made from SRRs exhibit an effective magnetic permeability (μ_{eff}) despite the SRRs themselves being made of non-magnetic materials, at microwave frequencies they are usually metallic [13]. The effective permeability can also be negative in a narrow frequency region close to the SRRs' resonance, which made them attractive choices to combine with thin wire arrays to create negative refractive index metamaterials [15, 17, 125].

In many of the early works, the response of the metamaterial was assumed to be independent of the interactions between the the individual meta-atoms, but this was soon understood not to be the case. For example, Gay Balmaz et al. [57] discovered in their research on the electromagnetic resonances of SRRs that the response of a metamaterial medium consisting of such meta-atoms is not determined solely by the response of the individual resonators, but is also greatly affected by the inter-element interactions, which in turn depend upon the relative arrangement of the SRRs. Other reports in this area include investigation of SRR pairs in planar and axial orientations [88–93, 71, 126–128], the study of the properties of chains of SRRs arranged along a common axis [22, 23, 129, 130], and several studies investigating interactions in two- and three-dimensional arrays of SRRs [131–135]. These references are but a few notable examples.

In constructing complex metamaterial systems, an understanding of the nature and

strength of the interactions between the meta-atoms that make up the material is vital. Although it is well known that the electromagnetic coupling strength between SRRs depends on both their relative orientation and separation [57, 71, 88–93, 126–128], the details of this interaction in both near- and far-field regimes has not been fully reported before. The motivation for the study undertaken in this chapter is to provide a new and full characterization by investigating the coupling between a pair of axially oriented single-ring SRRs as a function of both their separation and relative orientation. The approach in this work will be helpful in understanding the strength of interaction between any two SRRs in, for example, a 1D chain of SRRs and can readily be extended to more complicated systems, where dense packing of meta-atoms may be important.

Single-ring SRRs exhibit bianisotropy, i.e. an incident electric field induces a magnetic dipole moment in addition to an electric dipole moment, and vice-versa [58]. Therefore, both electric and magnetic interactions must be considered. When the additional degree of freedom arising from the relative orientation of the resonators, and the effect of retardation when the distance between the SRRs becomes of the order of the wavelength are also included, it quickly becomes apparent that this seemingly simple system will exhibit quite a complex coupling landscape. An analytical model that accounts for both the near-field interactions and the effect of phase retardation is developed, allowing the prediction of the coupling strengths between arbitrarily oriented and separated resonators. In the final section, the study is extended to multiple axially coupled SRRs and the suitability of the rectangular waveguide to study such systems is tested.

4.2 Resonant response of a single split-ring resonator

The single-ring SRR structure and its resonant response have been extensively discussed in the literature [58–68]. Figure 4.1a shows the simplest configuration of a SRR that is used in this experimental study. In figure 4.1a, the orientation of the SRR is chosen such that the electric field component of an incident electromagnetic wave is polarised across the split. As a consequence of bianisotropy, an out-of-plane magnetic dipole moment is induced along with an electric dipole moment [58]. Such a novel property where a magnetic response is derived from a naturally non-magnetic structure, makes SRRs attractive for designing metamaterials with effective negative permeability. Bianisotropy is not always an attractive property as was discussed in chapter 2 (section 2.3.2), and researchers have generally avoided bianisotropy in their designs where possible.

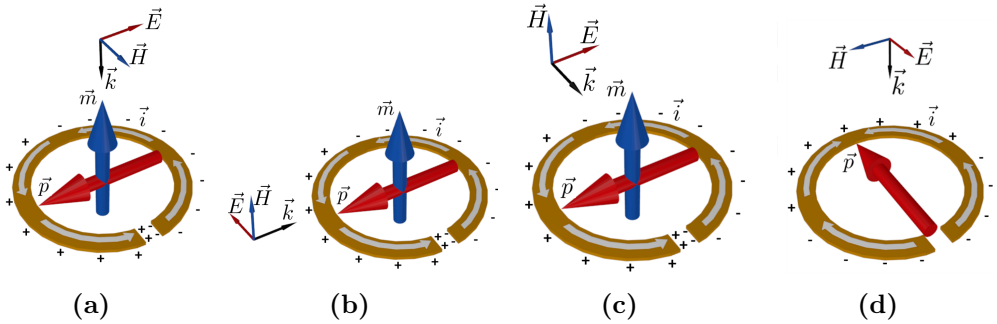

Figure 4.1: Schematic of a split-ring resonator oriented with respect to an incident electromagnetic wave such that its fundamental resonant mode is excited by (a) the electric field component, (b) the magnetic field component, (c) the electric and magnetic field components simultaneously. The corresponding induced electric and magnetic dipole moments in the SRR are shown as the red and the blue arrows respectively. The arrows are indicative only of the polarisations of the induced dipole moments and not of their respective strengths or positions. The broken white arrow on the SRR surface indicates the electric current that is induced in the SRR. (d) Changing the orientation of the SRR with respect to just the electric field component can facilitate the excitation of a higher order resonant mode, that lacks a magnetic dipole moment.

Figure 4.1a represents the instantaneous charge and current distributions, and the dipole moments corresponding to the fundamental resonance of the SRR. The electric dipole moment is the strongest when the charges of opposite polarities accumulate at the SRR's split-ends. The magnetic dipole is at its strongest when the electrons flow from one of the split-ends to the opposite split under the influence of the alternating driving field, thus generating a strong electric current at the metallic region opposite to the split. These occur at a phase difference $\pi/2$. Thus, despite the dipolar representation in figure 4.1a, the strength of the electric and magnetic field responses of the SRR to electromagnetic radiation are not simultaneously at their peak strengths. Since the greatest potential difference between the static charges occurs at the split, the electric dipole moment tends to be localised around the split-region of the SRR. Similarly, the magnetic dipole moment tends to be concentrated closer to the metallic region of the SRR on the side opposite to the split, where the electric current builds up to a maximum. For simplicity, the dipole representation in figure 4.1a is used in the discussions on coupled SRR dimers.

The fundamental mode can also be excited if the magnetic field component of the incoming wave is polarised normal to the plane of the SRR i.e. coinciding with the SRR's magnetic dipole moment, as shown in figure 4.1b. Naturally, the orientation of the SRR can also be chosen such that the fundamental mode is simultaneously excited by the electric and magnetic field components of the incident electromagnetic wave, as

shown in figure 4.1c.

With the field orientation in figure 4.1a as reference, if the SRR is rotated about its centre by 90° as shown in figure 4.1d, a higher order mode with a different charge and current distribution is excited. Due to the symmetric orientation of the SRR meta-atom with respect to the incident electric field, the induced electric currents are symmetric preventing the excitation of an effective magnetic dipole. An electric dipole moment is still excited in the SRR. The path length of the electric current is shorter by approximately half than that in the fundamental mode, causing the frequency of oscillation to be almost double that of the fundamental resonant mode. The analytical model in this chapter which characterises the SRR dimer's resonant response accounts for only the interaction between the fundamental resonant modes of the SRRs, which is found to provide results with sufficient accuracy. In the discussions that follow, the term 'resonance frequency' refers simply to the fundamental resonance frequency. The higher order mode is used in the discussion where applicable.

4.2.1 Design and fabrication

The resonance frequency of a single SRR is determined by the specific geometry of the SRR. The SRR can be considered as a simple LC resonator where the capacitance arises from charge separation across the split and the inductance arises from the circulating currents in the ring, as was discussed in section 2.3.1 of chapter 2.

For the current analysis, the SRR was designed using the eigenmode solver in COMSOL Multiphysics. The design parameters of the SRR were chosen so as to give a resonance frequency of 5.78 GHz. The low frequency cutoff of the TE_{10} mode for the WR137 waveguide is 4.3 GHz but, due to excessive absorptive losses within the guide close to this cutoff, the usable bandwidth is usually 5.35 to 8.2 GHz. The SRR's designed resonance frequency of 5.78 GHz maximises the frequency band over which the coupled modes of the system could be observed. The response of the SRR on its own and the SRR dimer system were measured across the full frequency range for which the TE_{10} mode is the only mode supported by the waveguide. Each SRR was designed to have an outer ring radius of 3.5 mm, a ring width of 370 μm, and a split-gap width of 1 mm. The SRRs were fabricated from 1.6 mm thick Duroid 5880 dielectric sheets clad with 20 μm of copper, from Rogers Corp. The relative permittivity of the Duroid substrate, as taken from the data sheet, is $2.20 + 1.98 \times 10^{-3}i$ at 8 GHz. The samples were fabricated through the photolithography process using the Durham Magneto Optics Laser Writer, as discussed in section 3.2.

4.2.2 Experimental characterisation of a SRR's resonant response

In order to characterise the electromagnetic responses starting from that of a single SRR to the electromagnetic interactions among multiple coupled SRRs mediated by their near-fields as well as the radiated fields, closed measurement systems such as rectangular waveguides offer a reliable means by capturing the energy scattered by the analyses system with minimal losses. Therefore, the experiments on the coupled SRRs in this work are performed inside the rectangular waveguide WR137. The rectangular waveguide facilitates the capture of all energy reflected from and transmitted through the analysed system with minimal loss. The first logical step to study the coupled SRR system is to begin by characterising a single SRR using the waveguide. The SRR can either be excited by using the electric or magnetic field component of the waveguide's TE_{10} mode or as a combination of both, by suitably adjusting the orientation of the SRR with respect to the field components [74].

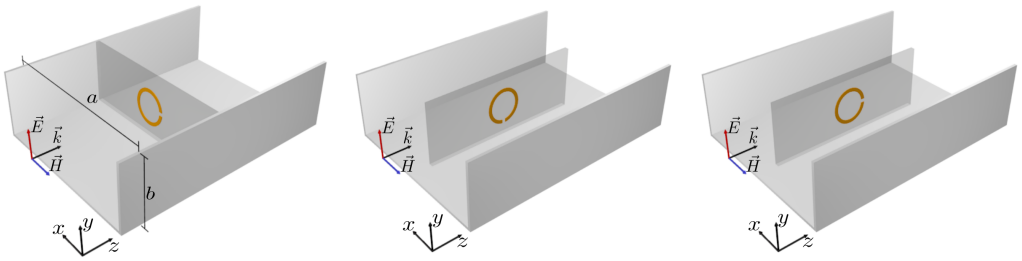

Figure 4.2: Schematic of a split-ring resonator in a rectangular waveguide excited by (a) the electric field component, (b) the magnetic field components and (c) both the electric and magnetic field components of the TE_{10} waveguide mode. Symbols 'a' and 'b' in (a) denote the cross-sectional length and breadth of the rectangular waveguide.

Figure 4.2a shows a single SRR placed in the waveguide (with the top removed) such that the electric field component of the TE_{10} mode excites its fundamental mode. The recorded reflected and transmitted signals are used to produce the frequency dependent transmissivity and reflectivity for this case, plotted as blue curves in figures 4.3a and 4.3b, respectively. It is observed from the blue curves that the resonance frequency of the SRR is 5.78 GHz, as expected.

Figure 4.2b shows the SRR's position changed with respect to the incident electromagnetic wave such that its split is in close proximity to the bottom metallic wall of the waveguide. Only the magnetic field of the TE_{10} mode interacts with the SRR and excites its fundamental mode. The electric field component excites the higher or-

der mode at a higher frequency as shown in figure 4.1d which does not interfere with the excitation of the fundamental resonance. The corresponding transmissivity and reflectivity measured in this case are shown as the red curves in figures 4.3a and 4.3b, respectively. The immediately notable features are the measured resonance at 5.72 GHz being lower than the expected resonance frequency and the narrow mode width of the observed resonance. In this SRR orientation, owing to its bianisotropy, the SRR dipole is excited at the split-region. However, the radiation channel for the electric dipole is restricted, leaving only the magnetic dipole to scatter energy from the SRR. Therefore, the width of the observed mode is narrower than for the previously observed case. The method of excitation does not have any role to play in altering the resonance frequency of the SRR. The only other factor that could account for this shift in recorded resonance frequency is the close proximity of the SRR's split to the top/bottom metallic wall of the waveguide. An explanation for this observation is offered by using the equivalent circuit (LC resonator) treatment of the SRR. The close proximity of the metallic wall to the charge concentrated around the split region of the SRR causes an increase in its gap capacitance and therefore a decrease in its resonance frequency [136].

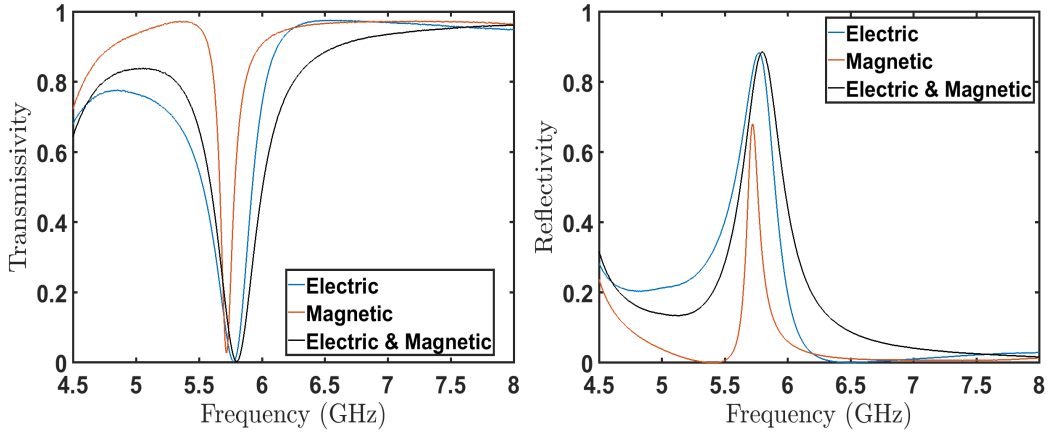

(a) (b)

Figure 4.3: Experimentally recorded (a) Transmissivity and (b) Reflectivity of a single SRR in the rectangular waveguide excited by the electric field component (blue line), the magnetic field component (red line) and both the electric and magnetic field components (black line) of the TE_{10} waveguide mode.

With the position of the SRR changed to that shown in figure 4.2c, the SRR's fundamental resonance could be simultaneously excited by both the electric and the magnetic field. The corresponding recorded transmissivity and reflectivity are shown as black curves in figures 4.3a and 4.3b, respectively. It can be noticed that the recorded

resonance frequency in this case is 5.8 GHz, which is about 0.3% higher than the design resonance frequency of 5.78 GHz. Another immediately notable feature is the marginally broader mode width in comparison to the case when the SRR was excited only electrically. The slightly increased mode width can be related to the simultaneous coupling of the electric and magnetic field components of the incident field to the SRR exciting its resonance, thus two available radiation channels into which the energy can be scattered by the SRR. The fractional increase in the resonance frequency can also be attributed to the simultaneous electric and magnetic excitation of the SRR. The small phase difference between the electric field exciting the SRR at its split and the magnetic field exciting the SRR close the metallic region opposite to the split may cause the resonance frequency to shift lightly. More importantly, in the phase cycle of charge oscillation in the SRR, the instant of maximum charge concentration at the split and the instant of maximum current in the metallic region opposite to the split are $\pi/2$ separated in phase. The restoration force of the charges will have to speed up slightly compared to their natural value to balance the simultaneous excitation of the electric current in the metallic region and a potential difference at the split, causing the recorded resonance frequency also to be higher.

From figure 4.3, it can be observed that the absorptivity calculated from the reflectivity and transmissivity data as (1-R-T) is non-zero i.e. the energy input to the system does not go only into reflected and transmitted radiation. The sources of absorption in this experimental measurement are as follows: 1) absorption in metal, 2) energy lost into the decaying waveguide modes, and 3) absorption in the substrate.

1. In the discussion on perfect electric conductors in section 3.4, it was mentioned that metals like copper typically have a penetration/skin depth of a few microns in the studied microwave frequency range. The thickness of the metal layer used to fabricate the SRRs is about 20 μm which is thicker than the skin depth in the studied frequency range. Despite the meagre penetration depth, the portion of the fields that do penetrate into the metal are absorbed. The waveguide's metallic walls also absorb a small fraction of the electromagnetic energy, though this loss is as small as 5% when calibrated correctly.

2. Though a great fraction of energy scattered by the resonators in the waveguide propagates via the fundamental TE_{10} waveguide mode, a small fraction is lost into the decaying modes of the waveguide that are not permitted to propagate in the studied frequency range.

3. Finally, the major contributing factor to the observed absorption of energy is

the substrate that supports the SRR(s). It can be seen from the discussion on fabrication in this chapter that the dielectric permittivity of the substrate has a non-zero imaginary part, that represents the absorption in the substrate. Especially around the resonance of the SRR, the strong electric field build-up close to the split-gap subsequently penetrates the adjoining substrate where it is absorbed.

Following the observations discussed in this section, the SRRs were excited only via the electric field component of the waveguide mode for all subsequent experiments, so as to keep the resonance frequency of each SRR unaffected by experimental factors.

4.3 Interactions in a SRR dimer - a coupled-dipole picture

To understand the nature of interactions between the SRRs of a coupled dimer, a second identical SRR was subsequently introduced 2 mm behind the first and the reflected and transmitted intensities were recorded for the two SRRs. The first SRR of the pair was always oriented such that the electric field component of the TE_{10} mode was polarised across the split. The second SRR was placed such that the substrates are always facing outwards as shown in figure 4.4a. The second SRR was rotated about its central axis with respect to the first, as shown in figure 4.4b and the reflected and transmitted signals recorded for relative rotation angles of 0°, 90° and 180°. At this separation (2 mm), the SRRs are coupled strongly to each other via their near fields.

If two identical SRRs are in close proximity along a common axis the eigenmode of the single SRR will split into two new eigenmodes, one at a higher frequency and one at a lower frequency than the original, in the same manner as coupled resonators in other areas of physics. The coupling mechanisms in the SRR pair could be qualitatively understood for the different relative orientation angles by using a simple dipole model. In the simple case of two dipoles the strength of the coupling between the dipoles depends upon their relative orientation and the coupling can be either longitudinal or transverse in nature, as was discussed in section 2.4 of chapter 2. Please refer figure 2.9 for the schematic representation of coupled dipoles. Recalling the discussion on coupled dipoles from chapter 2, the coupled modes whether longitudinal or transverse, correspond to aligned or anti-aligned dipole moments. For transversely coupled dipoles, the symmetric mode (aligned dipole moments) is the higher frequency solution and the antisymmetric mode (anti-aligned dipole moments) is the lower frequency solution; for longitudinally coupled dipoles this situation is reversed. It is known that for a given separation, the frequency difference between the coupled modes is greater for longitu-

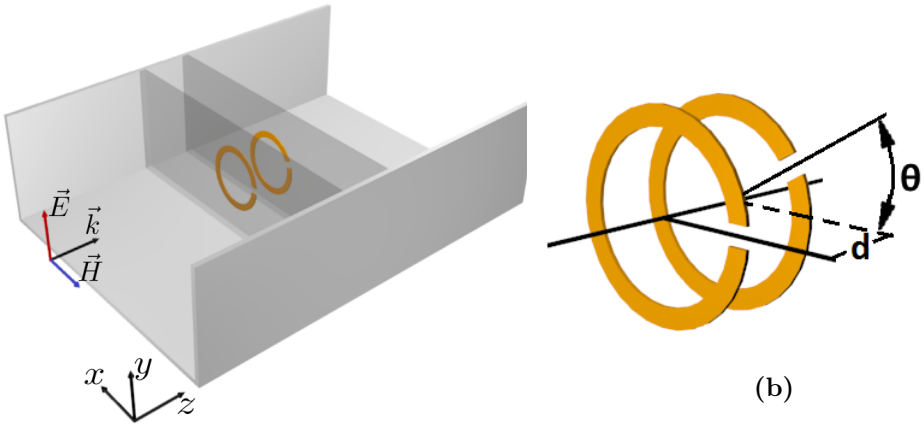

(a) (b)

Figure 4.4: (a) A schematic of the experimental setup showing the SRR pair within the rectangular waveguide with the lid removed. The substrates, shown as translucent blocks, face outwards in the experiment such that the only medium between the SRRs is air. The black arrow shows the direction of propagation, $\vec{k}$, of the TE_{10} mode whilst the green and blue arrows indicate the orientation of the electric and magnetic fields of the mode, respectively. The length and breadth of the cross-section of the waveguide are a and b respectively. (b) The axially oriented SRR pair with a separation d and relative orientation θ.

dinally coupled dipoles than for transversely coupled dipoles [85]. In figure 4.1, it was shown that the electric and magnetic dipole moments of a single SRR's fundamental mode are orthogonal to each other. The coupling between a pair of axially oriented SRRs via their electric dipole moments will therefore be transverse in nature, while the coupling via their magnetic dipole moments will be longitudinal.

The reflection and transmission spectra for the three relative rotation angles of 0°, 90°, and 180° are shown in figure 4.5. To explain the features in the spectra for the three relative rotations of the two SRRs, the relative orientations of the electric and magnetic dipole moments for each case is shown in figure 4.6. The first case considered is the pair of SRRs with a 0° rotation between them (figures 4.6a and 4.6b). Since the electric dipole moments are transversely coupled and the magnetic dipole moments are longitudinally coupled, when the electric dipole moments are aligned (anti-aligned) and thus raise (lower) the mode's energy, the associated coupling via the magnetic moments acts to counter these changes (this can be seen by comparing figures 4.6a and 4.6b with figure 2.9). Thus the frequency splitting between ω^+ and ω^- can be expected to be smaller than would be the case were it due to coupling via the electric or magnetic dipole moments alone.

The strength of radiative coupling to the modes, and the relative strength of the

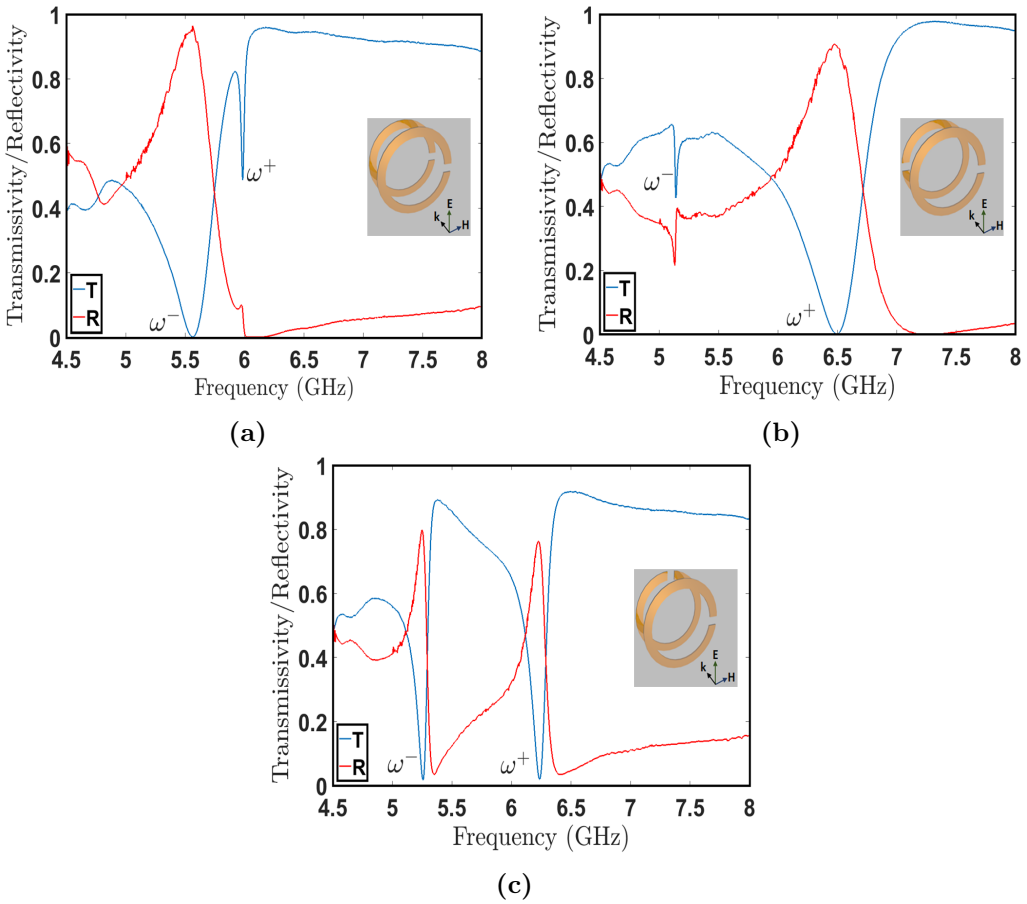

Figure 4.5: Reflection and transmission spectra for a single SRR (a), and a pair of SRRs oriented with relative rotation angles of 0° (b), 180° (c) and 90° (d) when separated by a distance of 2 mm. The ω^- and ω^+ labels indicate the lower- and higher-frequency coupled modes respectively. Insets: schematics showing the relative orientations of the SRR pair and the incident electromagnetic wave.

coupling between the SRRs via the electric and magnetic dipole moments, can also be understood in a similar way. In this geometry, only the electric field of the incident radiation can excite the SRRs (the magnetic field is orthogonal to the magnetic dipole moments) so that only the net electric dipole moment of the SRR pair needs to be considered; if this is large then there will be strong coupling to radiation and a broad resonance will be observed, while if it is weak a narrow resonance will be observed. Thus the ω^+ mode (narrow) can be recognised as having anti-aligned electric dipole moments (figure 4.6b), and the ω^- mode (broad) as having aligned electric dipole moments (figure 4.6a). By comparison with figure 2.9 it can also be identified that the coupling between the SRRs via the magnetic dipole moments must be greater for this separation than coupling via the electric dipole moments.

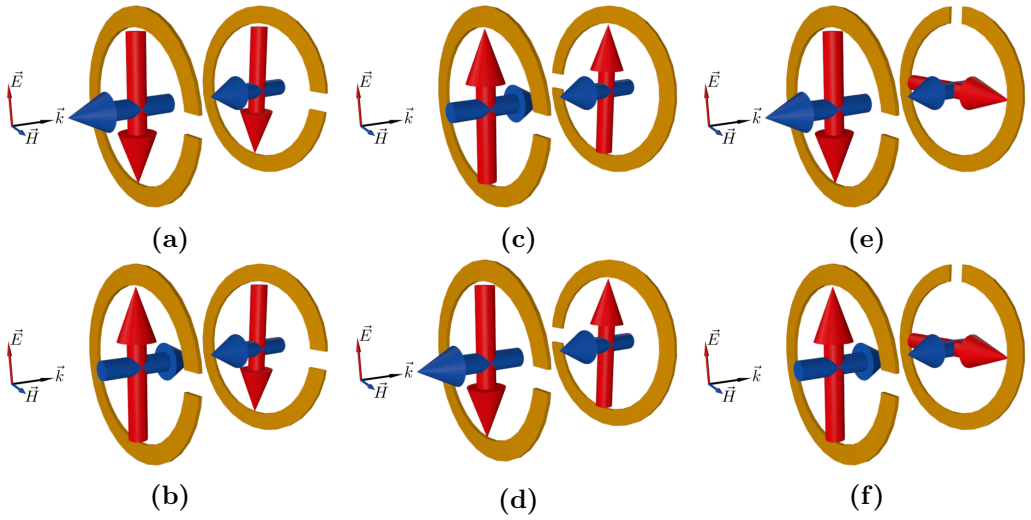

Figure 4.6: The relative orientations of the transversely coupled electric dipole moments, and longitudinally coupled magnetic dipole moments, in the coupled SRR pairs for relative rotations of 0° ((a) and (b)), 180° ((c) and (d)) and 90° ((e) and (f)).

When the second SRR in the pair is rotated such that $\theta = 180°$, the currents circulating around the second ring are reversed relative to the 0° rotated system for both coupled modes (figures 4.6c and 4.6d). By referring to figure 2.9 it can be seen that the coupling between the SRRs via the electric dipole moments and the coupling via the associated magnetic dipole moments will act in concert; this results in a larger frequency splitting between the modes. The net electric dipole moment for the modes will be approximately the same as for the 0° rotated system, resulting in modes of similar widths, but, importantly, it is now the ω^- mode which is narrow and has anti-aligned electric dipole moments, while the ω^+ mode is broad.

The electric dipole moment corresponding to the fundamental mode of the single SRR is always polarised in the direction across the split gap as shown in figure 4.1. Therefore, for the final case, when the relative orientation angle between the SRRs is $\theta = 90°$, the electric dipole moments of the two SRRs are orthogonal to each other so that the coupling between the SRRs is purely via their magnetic dipole moments (figures 4.6e and 4.6f). Since there is no coupling via the electric dipole moments, the size of the frequency splitting could be expected to lie somewhere between that of the $\theta = 0°$ and $\theta = 180°$ cases, which can be seen from the data. Since the electric field of the incident radiation is aligned only with the electric dipole moment of the first SRR in the pair, the net electric dipole moment of the SRRs will be the same for both coupled modes, and their widths will be approximately equal, again, as observed.

4.4 Characterisation of near-field interactions and retardation induced field interactions in the axially coupled SRR dimer

In this section, the coupled modes of a pair of axially oriented SRRs are studied as a function of orientation and separation. Reflection R and transmission T spectra were experimentally recorded as described in section 4.2, for relative orientations of 0°, 90°, and 180° as a function of the separation between the SRRs. Absorption spectra were calculated (using $1 - R - T$) and are shown in figure 4.7.

The necessary expressions for calculating the rectangular waveguide's Green's function, the coupling coefficients due to the charge and current interactions between a pair of resonators and the resonant modes of the coupled dimer were described in detail in sections 3.7.1 and 3.7.2 of chapter 3. The resonance frequencies of the symmetric and anti-symmetric modes of the coupled SRR dimer as a function of separation and relative orientation are predicted by the analytical model [71], by the expressions

$$\begin{aligned} \omega_s &= \omega_0 \sqrt{\frac{1+\beta}{1+\alpha}}, \\ \omega_{as} &= \omega_0 \sqrt{\frac{1-\beta}{1-\alpha}}, \end{aligned} \tag{4.1}$$

where ω_0 is the angular resonance frequency of a single SRR, and the magnetic (α) and electric (β) interaction constants due to the current and charge distributions, respectively.

The real parts of the coupling coefficients α and β quantify the strength of coupling between the SRRs due to the current distributions (the electrodynamic contribution), and the charge distributions (the electrostatic contribution), respectively. The imaginary parts of the coupling coefficients represent damping and are important for predicting the line shapes of the resonant modes. Since the purpose of the analytical model in relation to this study is to predict the resonant mode positions and quantify the coupling strength, it was sufficient to use only the real parts. In figure 4.8 the real parts of the coupling coefficients α and β as obtained from the model are plotted.

The three different data sets shown in figure 4.7 exhibit some common features.

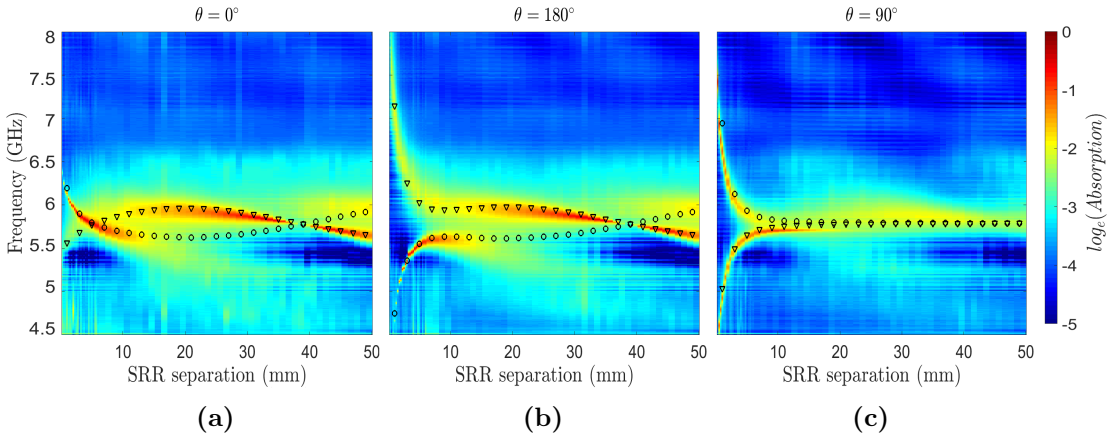

Figure 4.7: The absorption by the SRR pair as calculated from the measured reflection and transmission spectra plotted on a colour scale (see colour bar) as a function of the separation between the SRRs, for relative rotation angles of (a) 0°, (b) 180° and (c) 90°. The black circles indicate the position of the anti-symmetric resonant mode and the black triangles represent the symmetric resonant mode of the systems as predicted by the analytic model.

There is a consistently observed absorptive feature at about 5.3 GHz in all three experimental cases in figure 4.7, independent of the coupled SRR resonances. This feature could be an experimental artifact introduced by minor errors in the waveguide calibration. The length of the waveguide used (200 mm) is roughly an integral multiple of a propagating wave's wavelength in the waveguide at 5.3 GHz (97 mm). Minor calibration errors would result in weak reflections between the ends of the waveguide, resulting in such cavity-reflection artifacts. As for similarities in the observed experimental features, for separations above ∼5 mm the modes are only weakly dependent on separation while for small separations the mode frequencies diverge. Attention is first paid to the large separation data.

For both $\theta = 0°$ and $\theta = 180°$, when the separation is greater than ∼20 mm very similar behavior is exhibited; in this regime near-field interactions between the SRRs are absent. The analytical model predicts the presence of the antisymmetric mode between 15 and 40 mm despite the mode not being visible in the experimental data. The mode may not be visible because of its poor coupling to the incident radiation at these separations, but it is still an eigenmode of the system and is predicted by the analytical model. From equation (4.1) it can be seen that when the coupling coefficients are comparable the resonant modes become degenerate, while when these coefficients are markedly different the splitting is strong. At these large separations the interaction is mediated solely by the propagating field in the waveguide, and this interaction will

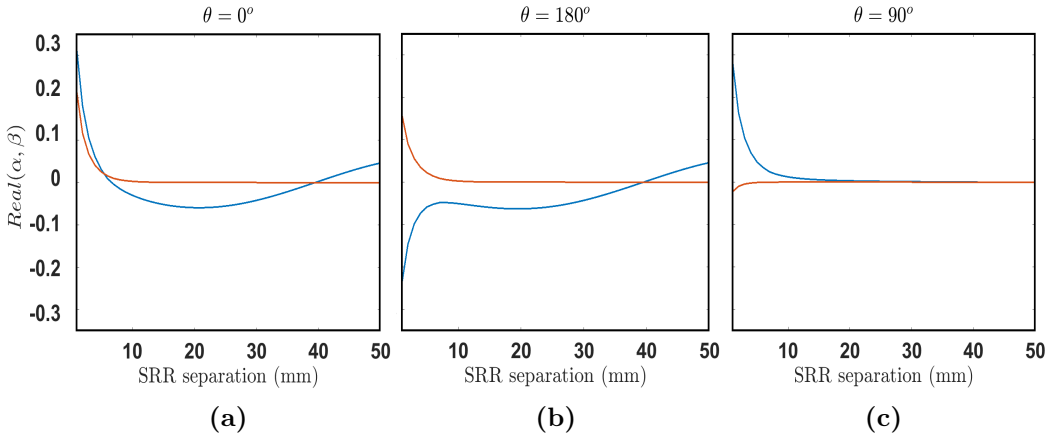

Figure 4.8: The coupling coefficients between the SRRs arising due to the currents (α) and electric charges (β) for relative rotation angles of (a) 0°, (b) 180° and (c) 90°, as a function of SRR separation. The blue curves represent the real part of α and the red curves that of β in all three figures, plotted from a SRR separation of 0.5 mm up to 50 mm in steps of 0.5 mm.

oscillate as a function of separation, with a period corresponding to the wavelength within the waveguide, i.e., in this regime the interaction is retarded.

When $\theta = 90°$ things are somewhat different. From figures 4.7c and 4.8c, the resonant modes of the SRR pair are degenerate and take the same frequency as the resonance frequency of an individual SRR. The lack of any oscillatory behavior similar to that in the $\theta = 0°$ and $\theta = 180°$ cases results from the electric dipole moments of the individual rings being orthogonal (the electric polarisation of the fields radiated by the first SRR cannot excite the electric dipole moment of the second SRR). In essence, the effect of retardation has been switched off in this geometry so that any interactions may only occur via the near fields.

The focus of discussion is next shifted to the small separation regime. When $\theta = 0°$, the near-field coupling mediated via the charge and current distributions conflict each other (the values of α and β have the same sign), see figure 4.8a. This is due to the electric dipole moments and the magnetic dipole moments of the SRRs both being aligned or anti-aligned (figures 4.6a and 4.6b), and results in a relatively small frequency splitting. It is also noted that at small separations the magnitude of α is greater than that of β indicating that the coupling strength between the SRRs due to the magnetic dipole moments is greater than that due to the electric dipole moments, confirming the prediction in section 4.3. This, coupled with the fact that for this orientation, the near-field contribution to α has the opposite sign to the radiative contribution, results

in a crossing in the values of α and β, and a corresponding mode crossing in figure 4.7a at a separation of approximately 6 mm.

When $\theta = 180°$, the near-field contributions to α reverse their sign relative to the $\theta = 0°$ case. The near-field coupling mediated via the charge and current distributions act in concert (the values of α and β have opposite signs), see figure 4.8b. Physically, as described in section 4.3, this difference in sign arises due to the difference in relative alignment of the electric and magnetic dipole moments (figures 4.6c and 4.6d). Since the coupling via the electric dipole moments is transverse in nature, while that of the magnetic dipole moments is longitudinal, this results in a significant splitting of the resonant modes. It is also noted that the contribution to α arising from near-field interactions has the same sign as that of the radiative contribution, and there is thus no frequency crossing of the coupled modes at these small separations.

Lastly, for $\theta = 90°$, the dipole model discussed in section 4.3 predicts the SRR interaction to be mediated only via the magnetic fields due to the orthogonal electric dipole moments of the two SRRs. However, it is noted from figure 4.8c that the electrostatic interaction is not completely absent at very close proximity. The coupled-dipole model does not account for such near-field effects. The interaction in this case is mediated only by the decaying near fields, with the value of β too small to play a deciding role in the overall coupling. The extent of the mode splitting in the near-field regime is thus dominated by the fields arising from the currents oscillating around the SRRs.

4.5 Resonant response in a 1D chain of axially coupled split-ring resonators

The experimental and analytical analysis of the SRR dimer led to understanding the nature of the resonances in the dimer. As a next step, the study is extended to a 1D chain of axially coupled SRRs in the waveguide. However, there were a few important factors to consider before analysing the coupled SRR chain.

In the experiments from sections 4.3 and 4.4, the SRR placement was carefully chosen such that the dielectric between the SRRs was just air. This arrangement simplified the analysis by excluding the effect of the dielectric substrates in the calculation of the coupling coefficients. However, in the case of a chain of SRRs, it is unavoidable that the gap between SRRs contains just dielectric or a combination of air and di-

electric, as seen in figure 4.9a. Figures 4.9b-4.9f show the absorption determined from experiments for 2 to 6 coupled SRRs in the frequency range 4.5 GHz (close to lower waveguide cut-off) - 6 GHz. Each subsequent figure corresponds to one SRR added to the chain. The SRRs were separated by 2.1 mm (1.6 mm substrate and 0.5 mm air-gap).

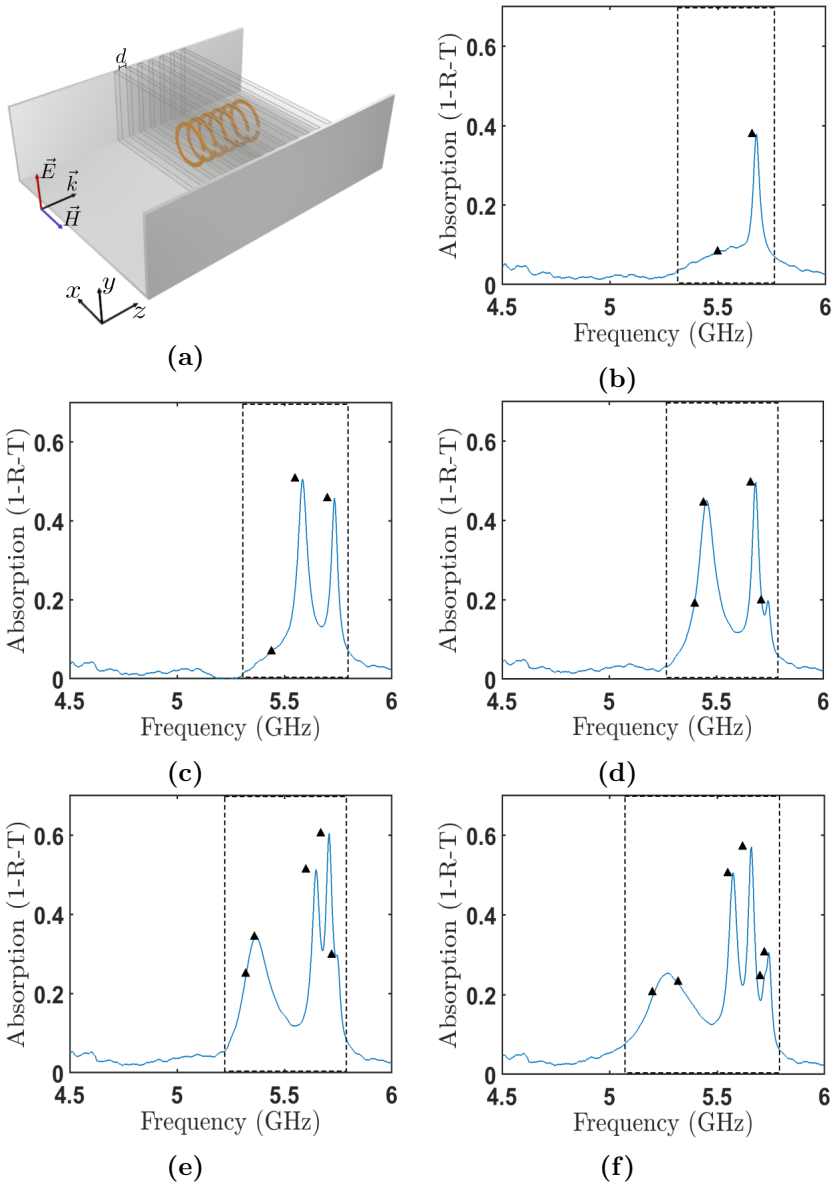

Figure 4.9: (a) Schematic showing a short 1D axial chain of SRRs ($\theta = 0°$) in the rectangular waveguide, with d being the separation between the edges of adjacent substrates. Experimental absorption for (b) 2, (c) 3, (d) 4, (e) 5, and (f) 6 coupled SRRs in the waveguide with a separation of 0.5 mm between substrate edges and relative orientation of 0°.

As seen from figure 4.9, the frequency range of the coupled resonant modes expands with the addition of more SRRs to the chain. This gradual increase in frequency range is highlighted by the dotted black box in figure 4.9. As is to be expected in coupled resonator systems, as many resonant features appear in the absorption spectrum as the number of coupled resonators. The triangular markers in the figures represent the frequency positions of the resonant modes, predicted by the eigensolver in COMSOL. The numerically predicted mode positions match the positions of the experimentally observed resonant modes with a difference of less than 1%. With the coupled modes appearing to have a defined band edge at about 5.75 GHz (where the highest frequency resonant mode of the coupled SRRs occurs), the lower frequency modes enter the absorptive frequency region close to the cut-off of the rectangular waveguide. Any information about the resonance in this absorptive frequency region is lost. As seen in the absorption curves in figures 4.9e and 4.9f for the cases of five and six coupled SRRs, the resonant modes at the lower frequency end appear unified into a single peak-like feature, where the individual resonances are indistinguishable, although the numerical finite-element model predicts the presence of two distinct resonant modes in the region. The frequency band of the waveguide is limited by the absorptive band at the lower end. Systematic resonant features introduced by scattering of the waveguide mode from the stacked dielectric substrates appear at the higher end of the waveguide's frequency band (not shown in figure 4.9).

Some modifications to the analysed system may rectify these shortcomings. The SRRs could be fabricated on thin flexible substrates and the spacing between them could be filled by suitably thick expanded polystyrene ($\epsilon_r = 1.02$, close to air) to eliminate the reflective features at the higher end of the waveguide's frequency band. The resonance frequency of the individual SRRs can then be tailored to be higher in frequency and away from the absorptive band of the waveguide. The flexibility and compressibility of the expanded polystyrene may, however, affect the accuracy of the recorded data. With many such difficulties, it is concluded that the rectangular waveguide is not an ideal system to characterise the resonant properties of a 1D chain of densely packed meta-atoms. Free space characterisation may yield better results for such systems.

4.6 Summary

A single SRR's resonant response was characterised in a rectangular waveguide and the experimental conditions affecting the SRR's resonance were discussed. The coupled modes of a pair of identical split-ring resonators as a function of their separation and relative orientation were studied. The reflection and transmission spectra of the SRR

dimer were measured, and an analytical model was used to help build an understanding of the physical mechanisms involved. It was demonstrated that the coupling in such systems exhibits a rich behavior that can only be understood by considering near-field and far-field interactions of both electric and magnetic character. The results of this work will help inform the design of more complex metamaterials that incorporate SRRs into arrays where the strength of inter-resonator coupling becomes significant, as, for example, in the case of very dense arrays. In the final section, the suitability of the rectangular waveguide to analyse 1D periodic metamaterials was tested. It was found that the waveguide is not a suitable system for studying a 1D chain of resonators. Free space analysis may yield better results for such systems.

Chapter 5

Realising an ultra-wideband backward-wave metamaterial waveguide

5.1 Introduction

In chapter 2, it was highlighted that the traditional treatment of metamaterials in early works was to produce bulk media with effective material parameters which give a tailored novel electromagnetic response. Electromagnetic metamaterials may have their effective values of the permittivity and permeability simultaneously negative, something not found in nature. Such double negative metamaterials have a negative refractive index.

The dispersion characteristics of such negative index metamaterials (NIMs) obtained using negative material parameters [14] and using an equivalent circuit approach [21] both revealed the existence of a negative dispersion passband that supports backward propagating waves as predicted by Veselago in [5]. The authors in [21] investigated the dispersion characteristics of the NIM's equivalent circuit model further, to analyse the system's resonant response when the electromagnetic wave propagating in free space and the SRR array (where the neighbouring SRRs are coupled to one another) were uncoupled. This analysis revealed that the SRR medium on its own could act as a backward-wave medium (without negative refractive index) by virtue of the magneto-inductive (MI) coupling between the SRRs, which was already a familiar concept by then [22, 23]. MI waves have since paved the way for the emergence of several interesting applications such as magneto-inductive waveguiding [23], magneto-inductive lenses

for sub-wavelength focussing of electromagnetic radiation [24, 25], and in general as wireless power transfer devices [26].

A parallel idea to the guiding of electromagnetic waves via magneto-inductive coupling is instead to use an electro-inductive waveguide (EIW) composed of electrically coupled complementary split-ring resonator (CSRR) meta-atoms [102], something that can also be implemented in general for wireless power transferring applications [98]. A CSRR is realised by replacing the metallic portions of a SRR with air-gaps and the air surrounding the SRR in its plane by metal, as if to create a negative image of the SRR [102]. The electro-inductive (EI) metamaterials built from the CSRRs also exhibit a negative dispersion and backward-wave propagation. Some of the other novel applications that have emerged from the EIW concept are oriented towards designing broadband backward-wave metamaterials using stacked CSRR metasurfaces [105] and active metamaterial particle accelerators [137].

The MI devices exhibit positive or negative dispersion depending on the sign of the mutual inductance between the SRRs, which in turn depends on the relative arrangement between SRRs being axial or planar [23]. On the other hand, the mutual capacitive effects in EIW devices have been shown to always result in a negative dispersion [105]. In the works on MIW and EIW devices, the general observation is that the axially coupled meta-atoms of either kind interact more strongly than those coupled in a planar configuration, thereby resulting in a broader operational bandwidth in devices constructed by axially stacking the meta-atoms [23, 105]. Different applications benefit from different fractional bandwidths of the metamaterial devices used. While it would be desirable to have wideband metamaterial lenses, waveguides and wireless power transfer devices would benefit from narrowband operation, complying with the prescribed IEEE frequency standards. The fractional bandwidth of the stacked CSRR metamaterial in [105] of about 26% is one of the broadest values reported in the literature. However, it is to be noted that the stacked CSRR metamaterial's operational bandwidth is quite sensitive to the lattice period along the direction of stacking and as acknowledged by the authors, negative dispersion could be achieved only for small stacking distances between the metasurfaces.

The motivation for the work in this chapter is twofold. The key to manipulating the operational bandwidth in metamaterials comes down to understanding the nature of the fields in individual meta-atoms as much as understanding the field interactions between them. It is well known from the literature that the conventional SRR [13] and by Babinet's principle, the CSRRs [102] are bianisotropic. As observed in chapter 4,

the coupling strength between bianisotropic SRRs is reduced due to the competition between the field interactions. The first motivation therefore is to analyse the field distribution of an individual CSRR meta-atom and suggest a non-bianisotropic design that would in turn enhance inter-element interactions and thus also enhance the metamaterial's operational bandwidth. The second motivation is to offer a missing puzzle piece to help complete the understanding of the field interactions in the complementary metamaterial structures. The standard approach to visualising the interactions in complementary metamaterials adopted in the literature has mostly been via circuit parameters. Here a coupled-dipole picture is used to describe the field interactions between complementary meta-atoms, in hopes that this approach will complement and extend the understanding gained using the standard circuit approach.

Below, in section 5.2, the nature of the resonant response of various SRRs and CSRRs are discussed, elaborating on a method to eliminate bianisotropy by making appropriate design choices.

5.2 Design approach to eliminating bianisotropy

The first logical step towards designing a non-bianisotropic complementary resonator is therefore to understand the nature of resonances in different configurations of regular SRRs and arrive at an optimum non-bianisotropic SRR design. The next step is only a matter of creating its negative image to arrive at the corresponding non-bianisotropic complementary resonator. Table 5.1 shows the electric and magnetic net dipole moments (shown by red and blue arrows, respectively) associated with the resonances in different bianisotropic and non-bianisotropic configurations of SRRs, which are discussed in detail next. The co-ordinate axes that are marked on the single-ring single-split SRR in the top row of table 5.1 are common to all the tabulated SRRs, with the z-axis normal to the plane of the meta-atoms.

The first SRR configuration considered is the simple single-ring single-split SRR that was the subject of the study on electromagnetic interactions between bianisotropic SRRs in chapter 4. The schematic diagram in the left end of the top row in table 5.1 shows the electric and magnetic net dipole moments associated with the fundamental resonance of this SRR. The necessary condition for the existence of bianisotropy in a metamaterial is the absence of inversion symmetry [77, 78]. To demonstrate this condition using the single-ring single-split resonator, choosing a yz-plane equally dividing the meta-atom into two halves as its central plane of inversion and transforming $x \rightarrow -x$ results in a meta-atom that does not coincide with the meta-atom before inversion. If

<table>
<tr><td colspan="2">Single-ring single-split</td><td colspan="2">Single-ring symmetric double-split</td></tr>
<tr><td> 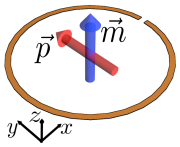
</td><td> 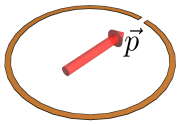
</td><td> 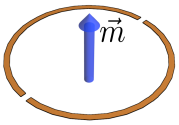
</td><td> 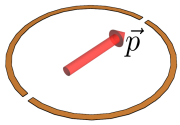
</td></tr>
<tr><td colspan="2">Single-ring asymmetric double-split</td><td>Double-ring single-split</td><td>Double-ring symmetric double-split</td></tr>
<tr><td> 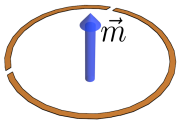
</td><td> 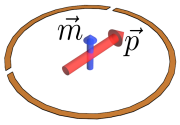
</td><td> 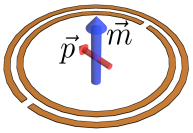
</td><td> 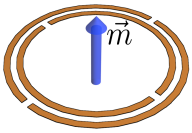
</td></tr>
</table>

Table 5.1: The electric and magnetic net dipole moments associated with the resonances of different ring resonators. Top row (from left to right): the fundamental resonance and the first higher-order resonance of the single-ring single-split resonator, the fundamental resonance and the first higher-order resonance of the single-ring symmetric double-split resonator. Bottom row (from left to right): the fundamental resonance and the first higher-order resonance of the single-ring asymmetric double-split resonator (asymmetric SRR or ASRR from [138–145]), the fundamental resonance of the double-ring single-split resonator ("split rings" from [13]), and the fundamental resonance of the double-ring symmetric double-split resonator (double-slit SRR or DSRR from [74]).

the original and the inverted meta-atoms were to be excited using the electric field component (E_y) of a normally incident electromagnetic wave, the electric dipoles excited at their splits would both be polarised along the same direction at any given instant. But, the electric currents resulting from the flow of charges between the ends of the splits are directed opposite to each other in the original and the inverted meta-atoms, resulting in oppositely polarised magnetic dipoles. The same conclusion can be arrived at by imagining the meta-atom being excited by just the magnetic field component (H_z) of an electromagnetic wave traveling in the y-direction or being simultaneously excited by the electric and magnetic field components (E_y and H_z) of an electromagnetic wave traveling in the x-direction.

The second schematic of the top row shows the first higher-order mode of the single-ring single-split resonator. Repeating the analysis steps followed for the fundamental resonant mode of the structure, the higher-order mode being excited by the electric field component (E_x) of a normally incident electromagnetic wave is considered, choosing an xz-plane through the centre of the meta-atom as its central plane of inversion.

The presence of inversion symmetry of the meta-atom about the xz-plane cutting it through its split, results in an effective electric dipole moment polarised in this direction, but the magnetic fields due to the symmetric electric currents cancel out. This is in agreement with the prediction that the even numbered modes of the single-split SRR do not have cross-polarisation effects [62].

The ultimate goal here is to design a non-bianisotropic resonator. The bianisotropy of the single-ring single-split resonator is removed by introducing a second split to the ring symmetrically opposite to the first, thereby imposing an inversion symmetry to the geometry (see right end of the top row in table 5.1). In the single-ring symmetric double-split case, it can be seen that the fundamental resonant mode has an out-of-plane net magnetic dipole moment but the electric contributions at the splits perfectly cancel each other out due to the imposed inversion symmetry about the central yz-plane equally dividing the meta-atom. The electrically excitable resonance seen at the far right end of the top row in table 5.1 which is also non-bianisotropic, is the first higher-order mode occurring at a higher frequency. The higher-order mode is seen to be quite similar to that of the single-ring single-split SRR.

Before constructing more complex meta-atoms using the single-ring configurations discussed so far, the discussion is steered towards another single-ring configuration to fully appreciate the importance of inversion symmetry to suppress bianisotropy. The two single-ring configurations considered above are both symmetric about the xz-plane that divides the ring through their split(s). An asymmetric single-ring double-split resonator (asymmetric split-ring resonator or ASRR from literature) [138–145] is considered next as seen in the second row of table 5.1, to show that the bianisotropy can be shifted from the fundamental resonance to the higher-order mode by changing the ring's central plane of inversion symmetry. The ASRR shown in table 5.1 has an inversion symmetry only about a central yz-plane equally dividing it. The result is that the fundamental mode comprises an out-of-plane magnetic dipole moment with the net electric response cancelling out due to the symmetric placement of the splits. This fundamental mode is found to be closely similar to that of the non-bianisotropic single-ring with symmetric splits in the right end of the top row in table 5.1. On the other hand, the higher-order mode not only has an electric dipole moment polarised along the x-direction, but also a weak out-of-plane magnetic dipole moment resulting from the imperfect net cancellation of the electric currents in the two unequal arms of the ASRR. The higher the degree of asymmetry in the structure, the stronger the cross-polarisation and stronger the magnetic response. A special case to consider is when the two splits are shifted further in the y-direction on the ring until they share

the same spatial location identical to the single-ring single-split resonator. The resonant mode in this case is the same as the fundamental resonant mode shown in the first schematic of the top row in table 5.1.

As a general rule, a resonator built by combining two other resonators retains the symmetry properties of the constituents and hence their bianisotropic or non-bianisotropic properties. This helps in designing multi-ring resonators whose fundamental resonance occurs at a much lower resonance frequency than those of the constituent single-rings and are therefore valuable in designing highly sub-wavelength metamaterials. For example, the schematic of the double-ring single-split resonator (popularly referred to as the "split rings" in [13]) shown third in the bottom row of table 5.1 is composed of two non-identical single-ring single-split resonators from the top row. The splits of the two rings are placed symmetrically opposite each other. However, the lack of perfect inversion symmetry about the y-axis (a yz-plane) through the meta-atom's centre results in the bianisotropic nature of the fundamental resonance. This geometry serves to achieve a high Q-factor resonance through an *almost* perfect cancellation between the electric fields at the splits, thereby making the meta-atom's response at resonance predominantly magnetic. Similarly, the double-ring symmetric double-split resonator (double-slit split ring resonator or DSRR from [74]) from the right end of the bottom row in table 5.1 is constructed from the single-ring symmetric double-split resonators from the top row. The inner ring is rotated by 90° with respect to the outer ring so that the inversion symmetry is preserved whilst avoiding interference between the inner and the outer rings' electric fields. The non-bianisotropic fundamental resonance of this structure is seen to possess only an out-of-plane magnetic dipole moment.

Let two single-ring resonators be selected from table 5.1 - the single-ring bianisotropic SRR and the non-bianisotropic version of the single-ring SRR with symmetric splits as basic building blocks to construct slightly more complex double-ring versions. These two single-ring structures are also shown in the left half of the top row in table 5.2. The second half of the top row shows the standard double-ring SRR and its non-bianisotropic double-ring version built from the above mentioned single-ring versions. The schematics of the meta-atoms are displayed along with the net dipole moments associated with the fundamental resonance of each resonator, shown as red (electric) and blue (magnetic) arrows. The bottom row in table 5.2 shows the corresponding complementary resonators, each being the negative image of the standard resonators in the top row. The co-ordinate axes displayed in the first meta-atom schematic in the top row of the table are common to all the tabulated meta-atoms with the z-axis normal to the planes of the meta-atoms.

Single-ring (bianisotropic)	Single-ring (non-bianisotropic)	Double-ring (bianisotropic)	Double-ring (non-bianisotropic)
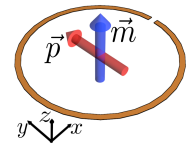	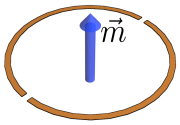	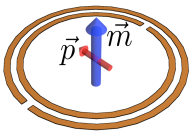	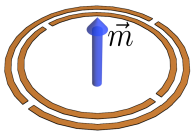
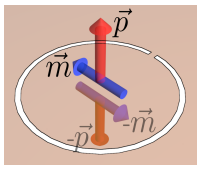	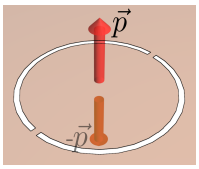	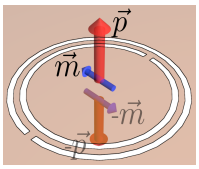	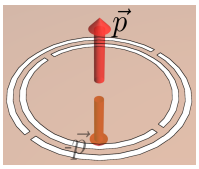

Table 5.2: Top row: The electric and magnetic net dipole moments associated with the fundamental resonance of different ring resonators. Bottom row: The electric and magnetic dipole moments in the top and bottom half spaces of the corresponding complementary resonators. Note: The complementary resonators exhibit zero net dipole moments since the modes consist of equal and opposite *local* dipole moments on either side of the rings, as shown. When considering the interactions between adjacent complimentary resonators, it is these local dipole moments in the spaces between the resonators that need to be considered.

The duality of fields between the SRR and CSRR meta-atoms due to Babinet's principle means that the electric and magnetic fields of the SRRs should be interchangeable with the magnetic and electric field distributions of the corresponding CSRRs [74, 102, 103, 146]. This is also seen from table 5.2. The CSRRs seen in the bottom row of table 5.2 exhibit out-of-plane electric dipole moments which are dual to the out-of-plane magnetic dipole moments of the standard resonators, as dictated by Babinet's principle. The bianisotropic resonators also exhibit in-plane magnetic dipole moments. The local dipole moments on either side (top and bottom) of a complementary resonator are equal in strength and oppositely polarised, resulting in a zero net dipole moment. Despite the zero net dipole moment, the CSRRs can be excited by time-varying local fields on one (either) side and can interact with other adjacent CSRR meta-atoms through their near-fields. Therefore, when analysing the interactions between adjacent complementary resonators, the local dipole moments of the resonators in the space between them need to be considered.

The double-ring bianisotropic and non-bianisotropic CSRRs are ideal candidates for comparing and highlighting the role of bianisotropy in limiting the operational bandwidth of a metamaterial. In section 5.3, 1D axially stacked complementary metamaterials constructed using the bianisotropic and non-bianisotropic CSRR meta-atoms

are analysed and compared. The purpose of the analysis is to highlight the improvement in operational device bandwidth in the non-bianisotropic metamaterial stack over that of the bianisotropic metamaterial stack.

5.3 Design and characterisation of the 1D metamaterial

5.3.1 Design and experimental setup

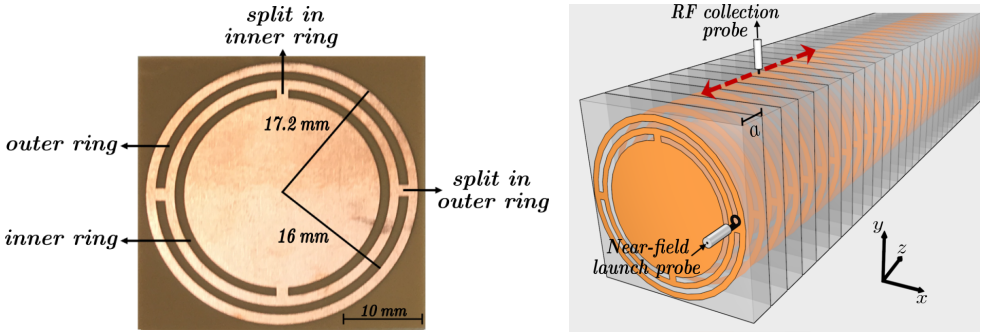

(a) (b)

Figure 5.1: (a) A colour photograph of the modified non-bianisotropic complementary split-ring resonator (MNB-CSRR) meta-atom as fabricated. The splits in both the slots measure 1.5 mm in height and the slots themselves are 1.2 mm wide. The circular metal disc has a radius of 17.2 mm and the outer split-ring shaped slots have an external radius of 16 mm. The metallic regions between the inner and outer slots is 1.2 mm wide. (b) Schematic of the experimental setup used to excite and detect the fundamental mode of the one-dimensional metamaterial, with period $a = 1.5$ mm. The substrate material has been rendered translucent to reveal the periodic structure. A near-field loop antenna excites the magnetic near-field of the 1D metamaterial stack, and a stripped coaxial probe traverses the length of the stack to scan and record the electric near-field above it, along the z-direction (shown dashed red). Both the launch antenna and the probe are connected to a Vector Network Analyzer.

The design process for the non-bianisotropic CSRR meta-atom to be used in the study was performed in a commercial finite element modeling software, COMSOL Multiphysics, using its eigenmode solver. A colour photograph of one of the fabricated non-bianisotropic CSRR meta-atoms is shown in figure 5.1a. It can be seen that the continuous metal sheet surrounding the split-ring shaped slots is truncated to a circular disc, to ease the experimental near-field detection of the supported modes. In order to investigate the effect of this deviation from the ideal complementary condition, an eigenmode model was built in th finite element software COMSOL Multiphysics. Figure 5.2 shows a colour map with the electric field corresponding to the truncated meta-atom's fundamental resonant mode, plotted in an yz-plane perpendicular to the plane of the meta-atom. The position of the meta-atom with respect to the co-ordinate axes are

the same as in table 5.2. The colour map shows a high electric field concentration in the split-ring shaped slot and at the truncated edges of the meta-atom, as one might expect. The black arrow heads show the instantaneous distribution of electric field around the meta-atom at this resonance. The electric field is seen directed normal to the plane of the meta-atom on either of its faces in agreement with the field representation that was plotted in figure 2.15b. Part of this electric field fringes to the edges as a consequence of the truncation. Despite this small modification to the the electric field distribution at the edges of the meta-atom, the collective electric response of the meta-atom could be represented via local electric dipole moments as the unmodified non-bianisotropic CSRR shown in the right end of the bottom row in table 5.2. The new modified meta-atom shall be addressed to as modified non-bianisotropic CSRR (MNB-CSRR) in the rest of the discussion.

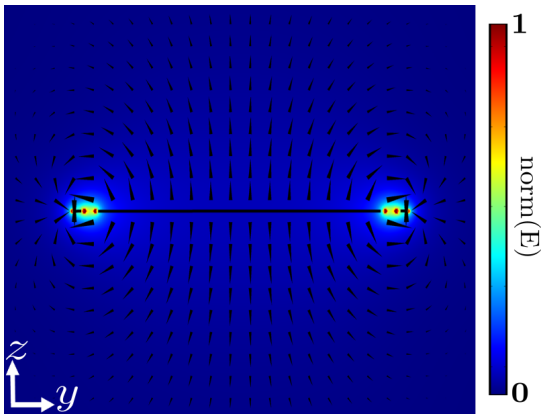

Figure 5.2: A yz-plane perpendicular to the plane of a modified non-bianisotropic CSRR (MNB-CSRR) and dividing it equally through its centre. The colour map shows normalised electric field norm. The black arrow arrow heads are vectors representing the instantaneous electric field distribution in the chosen plane. The dominant electric field component is that perpendicular to the plane of the meta-atom. The truncation of the complementary resonator results in the fringing of the normal electric fields towards the circular edges of the resonator.

The radius of the outer circular metal-disc of the fabricated MNB-CSRR is 17.2 mm, the widths for the split-ring shaped slots are 1.2 mm, the external radius of the outer split-ring shaped slot is 16 mm, the spacing between the inner and outer slots is 1.2 mm, and the height of the split-like strips in each of the slots is 1.5 mm. The meta-atoms were supported by the commercial Astra MT77 substrate which was 1.5 mm thick. The relative permittivity of the substrate material, as taken from the manufacturer's data sheet, is $3(1 + 0.0017\mathrm{i})$ and constant in the range 1 GHz to 20 GHz. This meta-atom design resting on the mentioned 1.5 mm thick Astra MT77 substrate

has a resonance frequency of 1.92 GHz, as calculated using COMSOL. However, in the 1D axially stacked metamaterial the resonators are effectively embedded in the substrate material. To see the effect of this environment on the resonance frequency of a single resonator a modified COMSOL eigenmode model was built with two Astra MT77 blocks 20 mm thick each, sandwiching a single MNB-CSRR meta-atom. The meta-atom's resonance frequency in this altered environment was found to be 1.43 GHz.

A 2D array of MNB-CSRRs was fabricated commercially by a local PCB manufacturer Graphic PLC, on a 1.5 mm thick commercial Astra MT77 substrate clad with 35 μm of copper. A layer of photoresist was coated on top of the copper layer and the design of the MNB-CSRR transferred into the resist by laser direct imaging. The subsequent development of the photoresist followed by etching of the resulting exposed metal using ferric chloride were performed as described in section 3.2 of chapter 3. The individual MNB-CSRRs were machine-cut from the panel, and the 1D metamaterial was constructed by axially stacking 90 MNB-CSRRs with a periodicity of 1.5 mm, as shown in figure 5.1b.

The modes supported by the 1D metamaterial stack were excited via their near-fields using a loop antenna positioned for optimum coupling as shown in figure 5.1b. A second antenna, in this case a simple section of stripped coaxial cable, was used to probe the electric near-field above the metamaterial stack, as a function of distance along the stack direction shown by the dashed red arrows. Both the launch antenna and the collection probe were connected to the ports of a Vector Network Analyzer (VNA). Despite the suppression of an effective magnetic dipole in the structure, optimally positioning the loop antenna in the vicinity of its magnetic near-field facilitates strong coupling into the mode. The coaxial probe recorded the local electric field strength in the frequency range of 1 GHz to 1.9 GHz.

5.3.2 Characterisation of the 1D metamaterial stack

A sample spatial electric field map plot in the inset of figure 5.3a shows the real part of the recorded complex electric field distribution as a function of position along the length of the stack, recorded at a frequency of 1.43 GHz. The main plot of figure 5.3a shows the Fourier transform determined from the complex-valued instantaneous spatial electric field at 1.43 GHz, plotted as a function of wavevector along the z-direction. The steps and side-effects of Fourier transforms was already discussed in section 3.5. It can be noticed here that only the positive half-space of the wavevector axis is presented, as it is sufficient to identify the nature of the dispersion exhibited by the resonant mode in

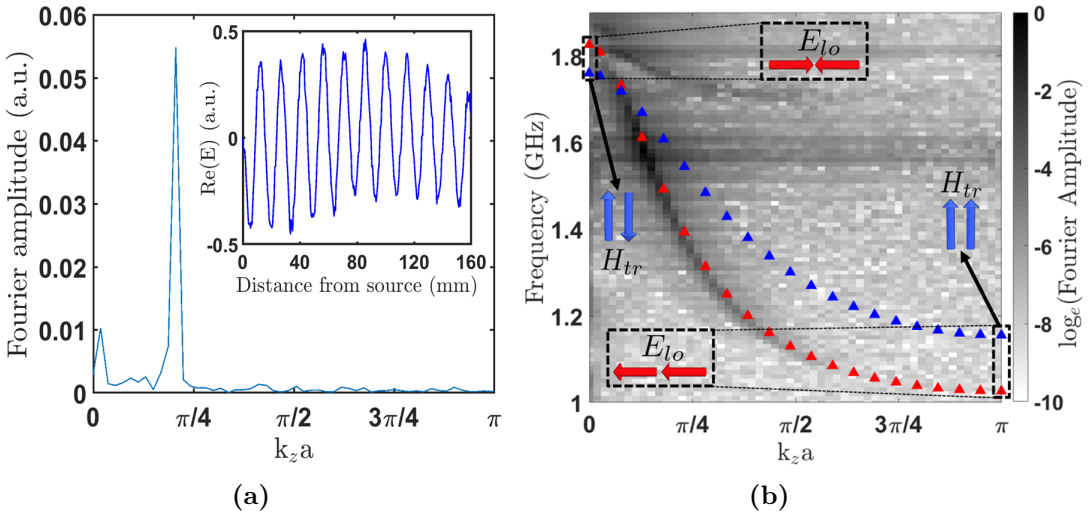

Figure 5.3: (a) Fourier transform of the complex spatial electric field distribution at 1.43 GHz, revealing the amplitude of the frequency component as a function of wavevector along the stacking direction. (Inset) Real part of the complex instantaneous electric field at 1.43 GHz plotted as a function of distance from the source along the 1D stack. The excitation source was at 0 mm on the plot. The electric field was recorded in steps of 0.75 mm. (b) Fourier amplitude of the complex spatial electric field map, plotted as a function of frequency and wavevector along the stacking direction. The red and blue triangles indicate the mode positions predicted by the eigensolver in COMSOL Multiphysics for the MNB-CSRR and CSRR stacks, respectively. The longitudinal electric field interactions corresponding to $k_z = 0$ and $k_z = \pi/a$ (Brillouin zone boundary) for the negatively dispersive modes of the stacks are highlighted by the dotted black box. The transverse magnetic interactions at these points for the CSRR stack are also presented.

the metamaterial. Combining the Fourier transforms of the spatial electric field maps for the measured frequencies results in the dispersion diagram shown in figure 5.3b. The resonant mode observed in the diagram has a negative gradient of dispersion (negative group velocity) for positive values of wavevector (positive phase velocity), indicating that the mode is negatively dispersive. As discussed in section 3.5, the ghost features due to spectral leakage are observed in the data besides the main resonant mode. The other negatively dispersive resonant feature observed around 1.8 GHz is a higher order mode of the metamaterial. The strong feature observed at 1.6 GHz spread across all the wavevector values is neither a component of the metamaterial nor a side-effect of the Fourier transform. It is a resonant feature introduced due to the stripped coaxial probe used to collect the electric field and can be removed by choosing the length of the probe tip more carefully.

To validate the experimental data, the MNB-CSRR metamaterial stack with the

same design specifications as that used in the experiment was modeled in COMSOL Multiphysics. The eigenvalue solver was used to identify the resonant modes of the metamaterial in the frequency range from 1 GHz to 1.9 GHz as a function of wavevector along the stacking (z-) direction. The computed mode positions are overlain on the experimental data in figure 5.3b, as red triangular markers.

The negative dispersion of non-bianisotropic and biansiotropic systems were next compared, by looking at the 1D MNB-CSRR stack and comparing it to that of a 1D CSRR stack. A model of the CSRR system was built in COMSOL with a period and boundary conditions identical to that of the MNB-CSRR medium. The design parameters – namely the width of the slots, height of the splits, the radius of the slots and the circular disc used for the CSRR meta-atom – were exactly half of the parameter values used to design the MNB-CSRR meta-atom. This adjustment to the design parameters was performed to ensure that the negative dispersion passband of the CSRR stack was centered at 1.43 GHz, the same as the MNB-CSRR stack. The eigenfrequency positions calculated for the CSRR stack as a function of wavevector are also overlain on the experimental data in figure 5.3b as blue triangular markers. It is seen that the resonant mode supported by the MNB-CSRR stack has a broader bandwidth than that supported by the CSRR stack of the same periodicity. The fractional bandwidths of the resonant modes for each system were determined using,

$$FBW = \frac{\Delta f}{f_c} \tag{5.1}$$

where FBW is the fractional bandwidth, Δf is the observed bandwidth and f_c is the central frequency of the band. Using the data from figure 5.3b, the FBW of the negative dispersive mode in the CSRR structure is calculated to be 41.5%, while that of the MNB-CSRR stack is 56.3% which, based on a thorough search of available literature, is broader than any reported value for magneto-inductive and electro-inductive metamaterials.

The group velocities ($d\omega/dk$) of the negative resonant modes in the CSRR and the MNB-CSRR structures were calculated using the numerically modelled dispersion curves shown in figure 5.3b and are plotted as a function of the longitudinal wavevector k_z in figure 5.4. The blue curve represents the group velocity of the resonant mode in the CSRR stack and the red curve represents that from the MNB-CSRR stack. It can be seen that the wavevector axis is indicated by $-k_z a$ representing the negative wavevector direction. This choice of axis is to indicate that the group velocity is always positive in a material and that the power always propagates away from the source. The

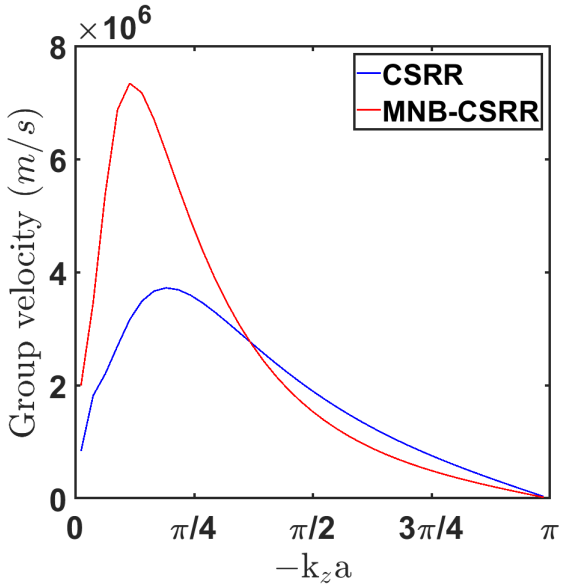

Figure 5.4: The group velocity for the negatively dispersive modes of the CSRR and MNB-CSRR 1D stacks as a function of wavevector in the stacking direction are plotted as blue and red curves, respectively. The wavevector axis is plotted on the negative scale because of the group and phase velocities being oppositely directed to each other in the studied metamaterials.

phase velocity in the backward wave medium is directed opposite to the group velocity and hence the wavevector is represented on a negative scale.

An interesting observation is that the negative group velocity of the mode in the MNB-CSRR stack is twice as large as that in the CSRR stack at small wavevectors. It is observed that the electro-inductive waves are able to travel faster in the MNB-CSRR stack owing to the enhanced coupling in the structure. This can be understood by drawing a comparison to the propagation of elastic waves in solids. The higher the stiffness of a material i.e. the stronger the atoms of the material are bound to one another, the higher the velocity of the elastic wave in the material.

Before proceeding to the discussion on the origin of negative dispersion in CSRR based metamaterial stacks, the attenuation of the MNB-CSRR stack for the periodicity value of 1.5 mm for which the 1D stack was experimentally characterised is estimated and discussed. The estimate is based on the numerically obtained dispersion relations as shown in figure 5.3b and the group velocity that was calculated for the MNB-CSRR stack in figure 5.4, using the technique described in section 3.6. The losses were added to the numerical model by including the substrate dielectric's loss tangent to the material properties and including the losses in the metallic resonators due to the metal's

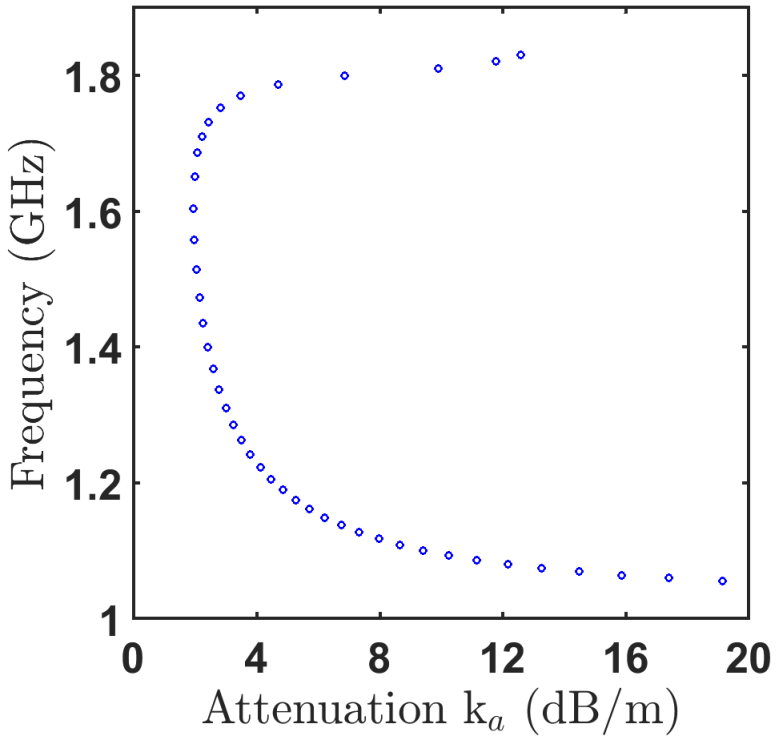

Figure 5.5: The attenuation of the MNB-CSRR metamaterial waveguide with period $a = 1.5$ mm calculated using the computationally obtained dispersion and group velocity data from figures 5.3b and 5.4. The lowest attenuation of 1.97 dB/m is observed at the frequency of 1.6 GHz. The loss is below maintained 3 dB/m (50%) in the frequency range of 1.3 GHz - 1.75 GHz.

finite conductivity through the impedance boundary condition.

Figure 5.5 shows the calculated attenuation of the metamaterial stack. The lowest estimated attenuation of 1.97 dB/m is observed at the frequency of 1.6 GHz. Comparing this attenuation to a wideband magneto-inductive waveguide from [147], it is observed that our lowest estimated attenuation is an improvement over one of the lowest reported attenuation values, of 2.3 dB/m reported in their work. However, the frequency range of operation in their work is in the range of about 60 MHz to 130 MHz which is quite different to ours. More recently, the magneto-inductive waveguide in [148] was reported to have attenuation as low as 0.13 dB/m at a frequency of 950 MHz which is much closer to our current frequency band of operation. It is to be noted however, that in this work a waveguide with fewer than 10 meta-atoms was experimentally characterised. No such reported attenuation values could be found for electro-inductive waveguides to compare.

A consistently low loss of below 3dB/m (below 50%) is observed in the frequency range of 1.3 GHz to 1.75 GHz. Such a low attenuation observed in the MNB-CSRR metamaterial stack is not surprising, given the symmetry of the electric fields as shown in figure 5.2, which make the MNB-CSRR meta-atoms poor radiators. The flatness of the computed dispersion at the band edges mathematically result in unrealistic loss values of greater than 100%. The estimation can be improved by including a higher density of data points at the band edges to better determine the non-zero gradient of dispersion and consequently the attenuation. However, it is true that the attenuation would be high at the band edges. The smaller gradient of the dispersion closer to the band edges, as seen in figure 5.3b, suggests the presence up of slow waves in the metamaterial which would make it easier for the energy to be localised and absorbed. While the attenuation we report is comparable to or slightly better than some of the previously reported values, it can be further improved by reducing the longitudinal periodicity of the metamaterial. This would enhance the inter-element interaction, reduce attenuation and also widen the bandwidth of operation.

In section 5.4, a simple toy-model of the dipole interaction is employed to explain the origin of negative dispersion in CSRR-based metamaterials (both bianisotropic and non-bianisotropic) and the observations from this section.

5.4 A toy dipole interaction model to analyse the nature of field interactions

The experimental and computational results confirm the expectation that the fractional bandwidth of the negatively dispersive mode in the MNB-CSRR stack exceeds that in the CSRR stack. The interaction among the meta-atoms in the bianisotropic medium is weakened by the competition between the electric and magnetic interactions, as expected. The weakened interaction strength results in the narrowing of the fractional bandwidth, and a smaller group velocity. In this section, a toy coupled-dipole model of the field interactions between the complementary meta-atoms is presented as a tool to help explain the origin of negative dispersion in these media, and the impact of bianisotropy on the operational bandwidth of the negative dispersion passband in the CSRR stack.

For the benefit of the reader, the general rules of dipole coupling are briefly recalled here (see figure 2.9 for schematic representation of the coupled-dipole picture). In the simple case of two dipoles, the strength of the coupling between the dipoles

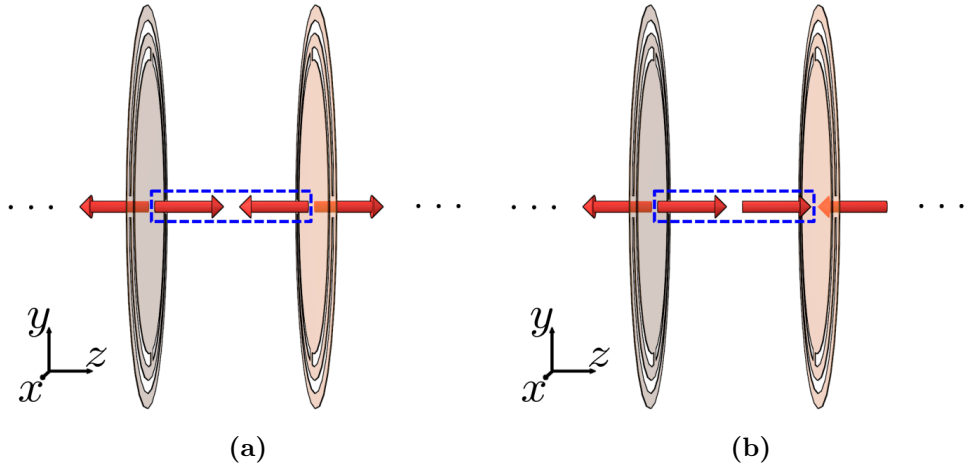

Figure 5.6: Relative orientations of the coupled electric dipole moments ((a) and (b)) between two MNB-CSRR (or CSRR) meta-atoms in the 1D stack. The anti-symmetric longitudinal dipole arrangement in (a) corresponds to $k_z = 0$ in the periodic medium favouring a higher energy solution. The symmetric longitudinal dipole arrangement in (b) corresponds to $k_z = \pi/a$ (a - period) favouring a lower energy solution.

depends upon their relative orientation, and the coupling can be either longitudinal or transverse in nature. These coupled modes, whether longitudinal or transverse, correspond to aligned or anti-aligned dipole moments. For transversely coupled dipoles the symmetric arrangement (aligned dipole moments) is the higher frequency solution and the antisymmetric arrangement (anti-aligned dipole moments) is the lower frequency solution; for longitudinally coupled dipoles this situation is reversed. For a given separation, the frequency difference between the coupled modes is greater for longitudinally coupled dipoles than for transversely coupled dipoles [85].

In the equivalent circuit treatment of CSRR based metamaterials, the negative dispersion is attributed to the positive mutual capacitance between the resonators [105]. If instead the negative dispersion is to be understood in terms of field interactions, the relative electric field orientations between two neighboring complementary meta-atoms in the stack need to be considered first, as shown in figures 5.6a and 5.6b. The view shown in figure 5.6 is from the side of the 1D stack looking along the x-direction. As established in section 5.2, this coupled electric dipole picture can be used to understand the electric field interactions in *both* the CSRR and MNB-CSRR stacks. The relative field distributions shown in figures 5.6a and 5.6b correspond to the resonance frequencies of the stack associated with wavevectors $\mathrm{k}_z = 0$ and $\mathrm{k}_z = \pi/a$ (at the Brillouin zone boundary), where a is the longitudinal stacking periodicity. The reason for this choice is that these are the frequencies at the band edges.

At $k_z = 0$, the wavelength of the electro-inductive wave in the 1D stack, $\lambda|_{k_z=0} = \infty$ i.e. the fields of the meta-atoms in the stack are all in-phase. Whether the resonance frequency associated with this configuration is higher or lower than the resonance frequency of the individual meta-atoms is determined by the relative dipole orientations. As seen in figures 5.6a and 5.6b, the electric dipole interactions between the complementary meta-atoms in the 1D stack are represented by longitudinal relative orientations of the dipoles, as highlighted by the dotted blue boxes. By comparing the relative dipole orientation in figure 5.6a to those in figure 2.9, it can be seen that the anti-symmetric longitudinal orientation corresponding to $k_z = 0$ favours a higher energy solution. The anti-symmetric longitudinal dipole pair is marked on figure 5.3b at $k_z = 0$, highlighted by the dotted black box.

At the Brillouin zone boundary where $k_z = \pi/a$, the fields of each meta-atom are π out of phase with those of its immediate neighbors. Figure 5.6b shows that the relative dipole orientation between the longitudinal electric field components of the adjacent meta-atoms is symmetric in this case, again as highlighted by the dotted blue box. By comparing this to figure 2.9, it can be seen that the longitudinally coupled symmetric orientation corresponds to a lower energy solution. In figure 5.3b, this dipole orientation is marked at the frequency position corresponding to $k_z = \pi/a$, highlighted by the dotted black box.

The two cases discussed above represent the relative dipolar arrangements that occur at the highest and lowest frequencies of the passband where negative dispersion is exhibited by the 1D stack. With these configurations pinned at the band edges, all other possible combinations of dipolar arrangements occur at band frequencies between these edge frequencies. The negative dispersion in the bianisotropic CSRR stack needs to be analysed in more detail next because both electric and magnetic field interactions need to be considered here.

Based on the magnetic dipole orientation of the CSRR as depicted in table 5.2, the relative dipole orientations of the coupled magnetic dipoles will be transverse; the arrangement of these in the 1D stack are shown in figures 5.7a and 5.7b, highlighted by the dotted red boxes. At $k_z = 0$, the magnetic dipoles form an anti-symmetric pair as shown in figure 5.7a. Referring back to figure 2.9, it can be seen that they favour a lower energy solution, thus competing with the electric field interaction that inclines towards a higher energy solution in this case. Similarly, at $k_z = \pi/a$, the magnetic dipoles are symmetrically coupled as seen in figure 5.7b favouring a higher energy solution (see figure 2.9), once again competing with the electric field interaction that inclines

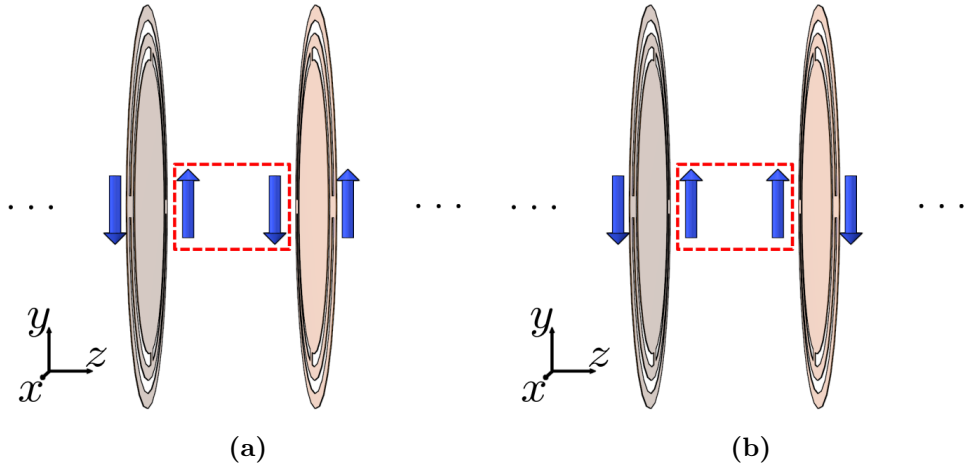

Figure 5.7: Relative orientations of the coupled magnetic dipole moments ((a) and (b)) between two CSRR meta-atoms in the 1D stack. The anti-symmetric transverse dipole arrangement in (a) corresponds to $k_z = 0$ in the periodic medium favouring a lower energy solution. The symmetric transverse dipole arrangement in (b) corresponds to $k_z = \pi/a$ (a - period) favouring a higher energy solution. (a) and (b) correspond to cases (a) and (b) of figure 5.6, respectively.

towards a lower energy solution. This competition between the electric and magnetic field interactions works to shift the edge frequencies towards the central frequency of the negative dispersion passband. The direct effect of this is a reduced interaction strength among the meta-atoms, a reduced resonant mode bandwidth (as seen in figure 5.3b), and a reduced group velocity (as seen in figure 5.4). Since the effect of magnetic interactions in the MNB-CSRR are suppressed owing to the lack of bianisotropy, the interaction is stronger and hence the operational bandwidth is broader.

It is briefly noted that this coupled-dipole picture may at first appear slightly at odds with what one might expect. Typically a negatively dispersing mode arises for *transversely* coupled dipoles since the in-phase arrangement of transversely coupled dipoles is the high energy solution, whilst the out of phase arrangement, corresponding to a higher wavevector, is the lower energy solution (seen from figure 2.9). This difference between initial expectations and the observed results is a direct result of the need to consider the coupling between the *local* dipole moments on either side of the complimentary ring systems rather than the *net* dipole moments as one would typically do in other systems.

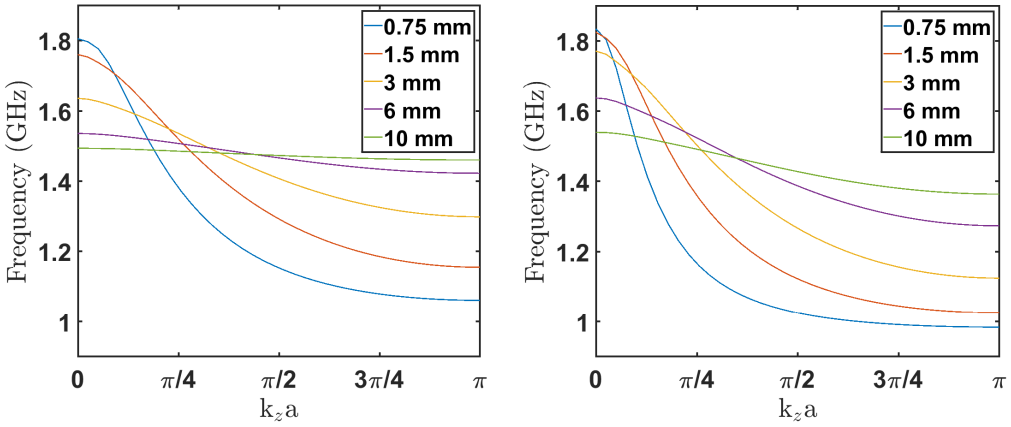

Figure 5.8: Numerically computed dispersion relations for 1D stacks built from (a) CSRR meta-atoms and (b) MNB-CSRR meta-atoms plotting for changing 1D periodicity in the stacking direction, for period 'a' = 0.75 mm, 1.5 mm, 3 mm, 6 mm, 10 mm. At 10 mm, the frequency response of the CSRR stack is reduced to a highly narrow band.

5.5 Sensitivity of the fractional bandwidth to the 1D periodicity

As discussed in section 5.4, the inter-element interaction strength in the 1D CSRR stack is governed by both the electric and magnetic field interactions, while that in the MNB-CSRR stack is governed by just the electric field interaction. The sensitivity of the negative dispersive mode bandwidth in the CSRR and MNB-CSRR stacks was analysed next, as a function of the 1D stacking period. The dispersion relations of the two stacks were numerically computed in COMSOL Multiphysics, as a function of the period along the stacking direction. The spacing between the meta-atoms was completely filled with the substrate material for dielectric homogeneity.

Figure 5.8 presents the numerically computed dispersion relations of the CSRR and the MNB-CSRR 1D stacks for period 'a' = 0.75 mm, 1.5 mm, 3 mm, 6 mm, and 10 mm. It can be seen from figure 5.8a that at a period of 10 mm, the negative dispersive mode in the CSRR stack is reduced to a highly narrow band. This behaviour was already reported in [105] where the authors showed that upon increasing the period further, the dispersion can also become positive. From the analysis in chapter 4 of interactions between coupled bianisotropic resonators, it was understood that the flattening of the frequency band here may not signify a lack of coupling between the meta-atoms. The balance between the electric and magnetic interaction strengths could cause the resonant states of the coupled meta-atoms in the system to be degenerate for a certain

value of period causing the resonant band to flatten. As observed in [105], when the period is increased further, the higher and lower energy mode positions switch causing a positive dispersion. It can be understood that this change in dispersing nature is caused by the shift in the balance between the two field interactions.

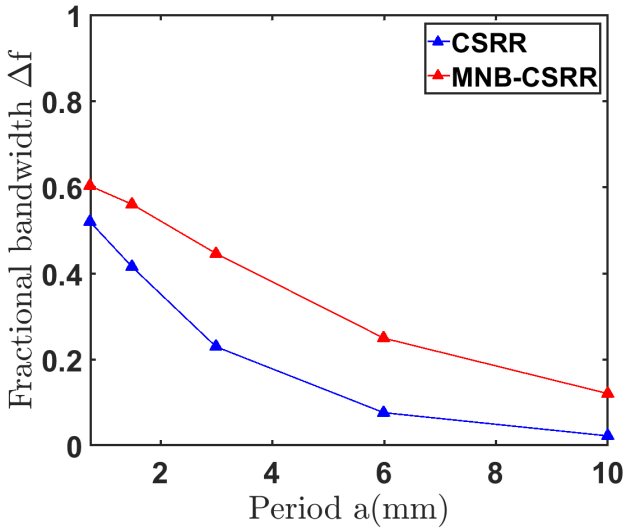

Figure 5.9: The fractional bandwidth of the CSRR (blue curve) and MNB-CSRR (red curve) stacks plotted as a function of longitudinal periodicity, as calculated from figure 5.8. The fractional bandwidth of the MNB-CSRR stack is higher than the CSRR stack for all inter-element separations.

From figure 5.8b, the MNB-CSRR stack's resonant response is less sensitive to changing period than the CSRR stack. At a = 10 mm, due to the decreased interaction strength among the meta-atoms, the fractional bandwidth of the MNB-CSRR has reduced to less than 0.2, as seen from figure 5.9, but still hasn't narrowed as much as that of the CSRR stack. The interaction strength in this system is governed only by the electric interaction and the rate at which the mode bandwidth falls should directly relate to the decay length of the electric near-field of the meta-atoms. The transverse dimensions of the MNB-CSRR meta-atom is double that of the CSRR meta-atom so that they operate at the same resonance frequency. Increasing the transverse dimensions of the MNB-CSRR meta-atoms while retaining the same periodicity as that of the CSRR stack also greatly helps increase the stack's fractional bandwidth by enhancing the electric interaction strength due to the capacitive action between MNB-CSRR meta-atoms.

The fractional bandwidth for the CSRR and MNB-CSRR stacks as computed from the dispersion relations in figure 5.8, are plotted in figure 5.9 as a function of the 1D stacking period. The immediate observation is that starting from a higher inter-element

separation (or period) and gradually decreasing it, shows that at very small separations the fractional bandwidth of the MNB-CSRR stack does not continue increasing with the same trend as that of the CSRR, but instead begins to approach a limit. This clearly demonstrates that at such small separations, the toy dipole interaction model breaks down and does not explain the effects of near-field interactions effectively, as was already observed in chapter 4 (section 4.4). The general observation however is that irrespective of the chosen inter-element separation, the fractional bandwidth offered by the MNB-CSRR stack is always higher than that of the CSRR stack.

The analysis of the results from numerical modelling in this section lead to the conclusion that, by excluding bianisotropy in the meta-atom's design, not only is the metamaterial's operational bandwidth increased, but the negative dispersion also has a reduced sensitivity to longitudinal stacking periodicity in the metamaterial.

5.6 Summary

The resonances of bianisotropic and non-bianisotropic SRRs along with that of the corresponding complementary SRRs were analysed and discussed, along with a modified geometry of a non-bianisotropic CSRR design to remove the inherent bianisotropy. A negatively dispersing mode supported by a 1D metamaterial consisting of axially stacked MNB-CSRR meta-atoms was analysed and the experimentally determined mode dispersion was found to be in good agreement with numerical simulations. It was also shown that the operational bandwidth of the mode is ultra-wide and exceeds that offered by a similar system consisting of bianisotropic elements and also that of any report that could be found in the literature. Estimation of the metamaterial stack's attenuation reveals that the losses in the waveguide are lower than most proposed magneto-inductive waveguides, with room to improve by tuning the longitudinal periodicity. A toy coupled-dipole model was employed to show how the origin of negative dispersion in CSRR based metamaterial devices can be understood. The same model was used to indicate how bianisotropy limits the maximum operational bandwidth. It is deduced that the increased transverse dimension of the MNB-CSRR meta-atoms compared to that of the CSRRs also helps in enhancing the inter-element interactions and hence the operational bandwidth. As a last step in the analysis, the sensitivity of the negative dispersion was compared between the two stacks for increasing values of longitudinal stacking period. The MNB-CSRR stack's dispersion showed less sensitivity to changing lattice period. The results from this study should be of assistance in the design of broadband backward-wave metamaterial devices, with enhanced electro-inductive waveguiding effects.

Chapter 6

A metamaterial waveguide with simultaneous forward and backward-wave propagation

6.1 Introduction

Many works on the dispersion characteristics of 1D metamaterials such as [21–25, 105], show that the relative orientation of the meta-atoms constituting the metamaterial, and consequently the relative polarisation direction of the fields in the meta-atoms at their resonance, determines the positive or negative dispersion exhibited by the metamaterial. The bandwidth of the passband depends on the strength of interaction between the meta-atoms. Previous works have shown that axially stacking regular SRRs can help achieve a positive dispersion [22, 23] and axially stacking CSRRs results in a negative dispersion [105]. The work in the previous chapter showed that a broadband negative dispersion could be achieved using axially stacked modified non-bianisotropic CSRRs.

In the current chapter, the design of a 1D metamaterial prototype that supports both positive and negative dispersion in an overlapping frequency passband is pursued. Such a metamaterial would permit simultaneous forward- and backward-wave propagation. The main motivation is that this metamaterial could act as a microwave analogue of nanoparticle chains that support electromagnetic energy transfer with a positive or a negative dispersion when their longitudinal or transverse dipole modes are excited [86, 87]. The aim is to achieve simultaneous positive and negative dispersion in the metamaterial without having to change the relative orientation of the meta-atoms. Naturally, tailoring the behaviour of the metamaterial comes down to carefully

choosing the design of the meta-atoms and their relative orientation in the metamaterial (which will remain fixed). This shall be discussed in the first section of this chapter.

6.2 Resonant dipole analysis for design of the meta-atom

The first step in the pursuit of the goal is to lay down some basic design rules for the target metamaterial:

1. Coupled-dipole studies show that a 1D chain of longitudinally coupled (electric or magnetic) dipoles gives rise to a positive dispersion while a 1D transversely coupled chain of dipoles exhibits a negative dispersion [86, 87]. The target meta-atom should, therefore resonate with both in-plane and out-of-plane dipole moments of the electric and/or magnetic kinds. When the meta-atoms are stacked in the preferred axial configuration, the interactions between the transversely coupled in-plane dipole moments and that between the longitudinally coupled out-of-plane dipole moments should result in negative and positive dispersions, respectively.

2. The in-plane and out-of-plane dipole moments should not be associated with the same resonant state of the meta-atom (for example, like the electric and magnetic dipole moments of the fundamental resonance in a simple single-ring SRR from chapter 4 (see figure 4.1)). In other words, the in-plane and out-of-plane dipole moments should be associated with different non-bianisotropic resonances of the meta-atom and should have dissimilar field distributions. Interaction between the two resonances will result in a stop-band due to anti-crossing between the modes, inside the target frequency range.

3. The resonances associated with the in-plane and out-of-plane dipole moments should not be separated too much in frequency. The closer the frequency separation between the individual resonances, the higher the frequency overlap of the positive and negative dispersing passbands.

The simplest route to achieving the first and the second design goals is to combine two meta-atoms such that they are not conductively coupled (not physically connected). The third design goal is relatively easy compared to the other two, as it involves the scaling of the two constituent meta-atoms' dimensions to control their resonance frequencies.

The design of the target meta-atom is commenced by tabulating and analysing the dipole moments of a few known meta-atom configurations in table 6.1. The co-ordinate

Non-bianisotropic SRR (NB-SRR)	Closed ring	Circular hole in a metal sheet
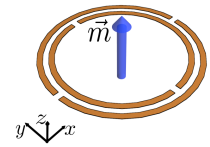		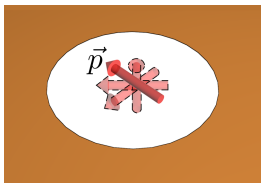
Truncated metal square with circular hole	**NB-SRR inside truncated metal hole**	
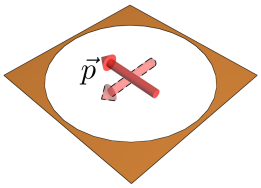	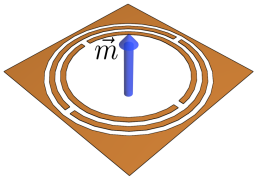	

Table 6.1: Top row (from left to right): the magnetic net dipole moment associated with the fundamental resonance of a non-bianisotropic SRR (NB-SRR), the electric net dipole moments of a closed ring, and a circular hole in an infinite metal sheet. The solid red arrows polarised along the y-axis direction is one of the possible electric polarisations that can be excited in the structures. Other possible electric dipole polarisations are shown as faint red arrows with a dotted outline. Bottom row (from left to right): the electric net dipole moments excitable in of the truncated metallic hole resonator at its fundamental resonance, the magnetic and electric net dipole moments of the combined meta-atoms arising from the resonances of the NB-SRR and the truncated metallic hole resonator, respectively. The infinite metal sheet with a circular hole is truncated to a square resonator containing the circular hole with the NB-SRR positioned centrally within the circular hole. The new meta-atom has orthogonal and selective polarisations of electric net dipole moments owing to the inversion symmetry imposed by the NB-SRR meta-atom about the x- and y-axes.

axes shown in the left of the top row is common to all the tabulated meta-atoms, with the z-axis being normal to the planes of the meta-atoms. The complementary resonators are not included in the initial design stage, for simplicity.

The first meta-atom tabulated in the top row of table 6.1 is the non-bianisotropic SRR (NB-SRR) (the double-slit SRR or DSRR) that was discussed in chapter 5. The meta-atom is non-bianisotropic owing to the inversion symmetry in its geometry about the x- and y-axes. The fundamental resonance of the meta-atom consists of only an out-of-plane magnetic dipole moment and no net electric contribution. The NB-SRR is, therefore, an ideal candidate to be the source of longitudinal magnetic field interactions in the metamaterial. The next requirement is to choose a non-bianisotropic meta-atom that possesses an in-plane electric dipole moment in its fundamental resonance.

On the theme of circular resonators, the first candidate to be considered is a closed ring, shown second in the top row of table 6.1. To add an historical note, this simple closed-ring resonator was used to model the outer sheath shielding a central SRR in early analytical treatments of Magnetic Resonance Imaging (MRI) devices [11, 12]. The closed-ring resonator does not support a magnetic resonance on its own or in response to the magnetic flux of the central SRR, quite simply because of its closed nature. However, its circular geometry permits the excitation of an in-plane electric dipole moment due to an electric field polarised along any direction in the plane of the meta-atom, as seen from the schematic in table 6.1. A solid red arrow along the y-direction is shown to indicate an electric dipole moment along that direction. A few other faint red arrows with dotted outlines are also shown to indicate that an in-plane electric dipole moment could be excited in any other in-plane direction.

Another candidate meta-atom is considered as the source of in-plane electric dipole moments before moving on to the final design. Consider a circular hole in a continuous metal sheet, as seen in the right end of the top row in table 6.1. Its geometry differs from that of the closed-ring resonator only in that the metallic region surrounding the inner hole consists of continuous metal instead of a ring with a finite width. The idea of using metallic films with an array of holes and stacking the hole arrays (or fishnet structures) to achieve novel properties like a negative refractive index and extra-ordinary transmission (EOT) has been pursued before [43, 44, 47, 48, 149–151].

Special attention needs to be paid to the references [149–151] where the criteria on the dimensions of each sub-wavelength hole in the constructed 3D array with respect to the other lattice parameters in order to achieve EOT and negative refractive index simultaneously are explored in detail. The work in [149] points out that it is crucial for the hole's diameter, say a, to be lower than the transversal periodicity d (periodicity in the plane of the meta-atom) for EOT to be achieved ($d > a$). In this regime, the mode that is excited within the hole is evanescent in nature i.e. the 3D stacked hole array exhibits EOT and negative refractive index below the cut-off region of the individual holes' fundamental resonance. The works in [150, 151] explore further the propagating modes supported by the stacked hole array, which occur when the holes are no longer sub-wavelength. These propagating holes no longer exhibit a left-handed (negative) dispersion, but instead a right-handed (positive) dispersion. These works also show that even in the subwavelength hole regime, when the longitudinal periodicity (stacking distance between 2D hole arrays - d_z if z is the stacking direction) exceeds the hole diameter a ($d_z > a$), the negative dispersion vanishes and right-handed behaviour is

exhibited.

When the circular holes are stacked one above the other with an intermediate dielectric, capacitive effects can be observed due to electric field fringing between opposite edges of each circular hole and between the edges of axially stacked holes. In the propagating regime of the holes (hole diameter comparable to wavelength $a \approx \lambda$), like the closed-ring resonator, an in-plane electric dipole moment can be induced in the circular hole, with polarisation along any in-plane direction, as represented in the schematic in table 6.1.

The circular geometries of the closed-ring resonator and the hole in the metal film give rise to inherent inversion symmetry along all directions in their plane. If the infinite metal film were to be truncated to a square metallic strip containing a circular hole at its centre (see the first schematic on the bottom row of table 6.1), the inversion symmetry is defined and the electric net dipole moments have polarisations only along the x- and y-directions. Moreover, this truncated resonator satisfies the conditions laid out in [149–151] to support propagating modes and also a negative dispersive behaviour when stacked. Truncating the metallic area around the hole to a square ensures that the hole diameter is comparable to the transverse periodicity ($d \approx a$), thereby entering the propagating regime instead of the EOT regime. The hole diameter chosen for this work is much larger than the stacking periodicity, as will be shown in the later modelling and experimental sections. In this regime, the system exhibits a negative dispersion despite not being in the EOT regime. Let this resonator be referred to as the truncated hole resonator for the rest of the discussion.

As a consequence of the truncation, local magnetic responses arise at the edges of the metallic square due to electric currents in these regions, but a magnetic net dipole moment is suppressed at the resonance(s) due to the net cancellation of the magnetic fields. Figure 6.1a shows a colour map of the normalised electric field norm plotted in the plane of a truncated hole resonator. The black arrows representing the instantaneous electric field distribution shows a dominant in-plane electric field component along the y-direction. The red arrows show the corresponding instantaneous electric current distribution. By inversion symmetry of the meta-atom, the net magnetic field cancels out. The corresponding dipolar representation of the collective electric field strength along the y-direction is represented in the schematic diagram shown in the bottom row of table 6.1. The orthogonal electric field distribution looks the same but rotated by 90° with respect to that shown in figure 6.1a, hence not shown. This distribution would correspond to the faint electric dipole with dotted edges shown in table

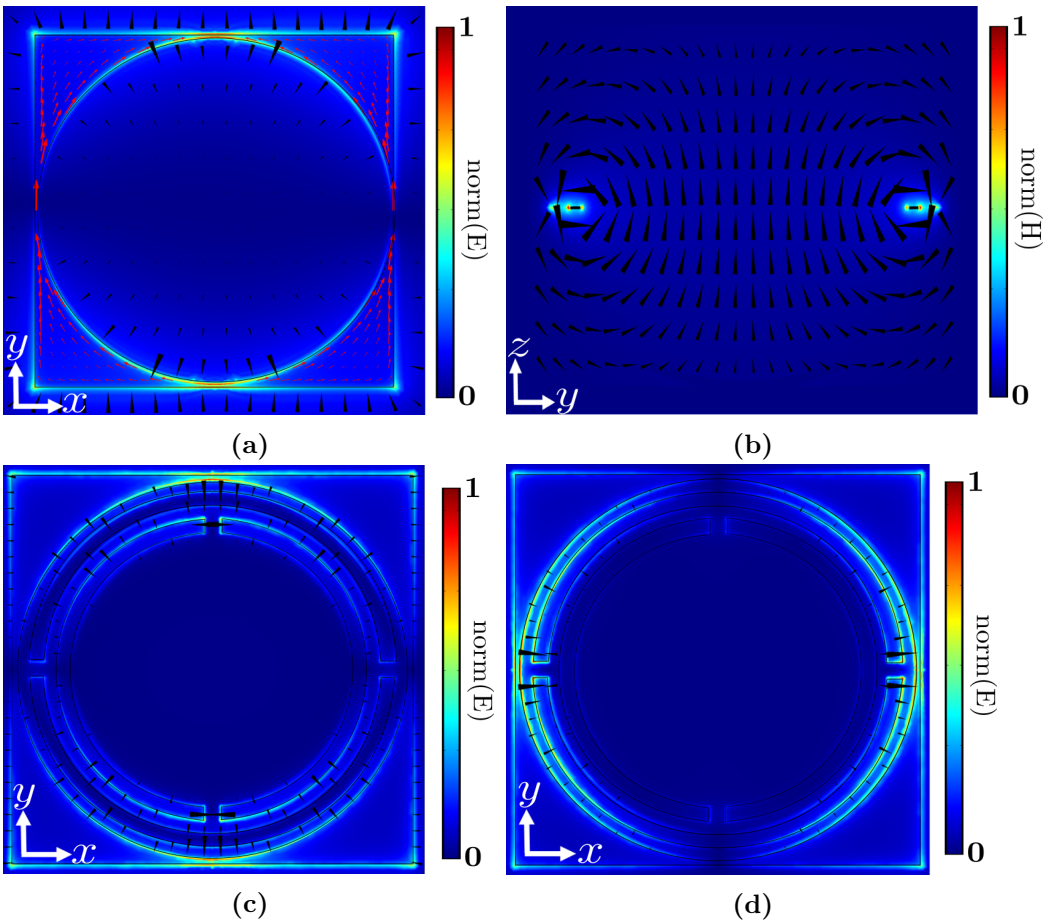

Figure 6.1: (a) An xy-plane containing a truncated hole resonator showing the normalised electric field norm as a colour map at one of its orthogonal resonant modes. Black arrow heads show instantaneous electric field distribution and the red arrows show the corresponding electric current distribution of the mode. (b) A yz-plane perpendicular to a single hybrid NB-SRR (HNB-SRR) dividing it through its centre shows the colour map of normalised magnetic field norm corresponding to its fundamental magnetic resonance. The black arrow arrow heads are vectors representing the instantaneous magnetic field distribution in the chosen plane. The collective magnetic field strength can be represented by an out-of-plane magnetic dipole moment. (c) and (d) show in-plane normalised electric field norm of the two orthogonal electric resonances in the HNB-SRR meta-atom. The black arrow heads represent the instantaneous electric field distribution. The dominant electric field component in each case is pointed along the x- or y- direction.

6.1. The truncated hole resonator makes for a better candidate to contribute towards the in-plane dipole moments because it has defined in-plane electric dipole polarisations. An increased metallic area compared to the closed-ring also ensures enhanced capacitive interaction between adjacent stacked hole meta-atoms.

Since there are now two candidate meta-atoms to contribute independently towards

the in-plane and out-of-plane dipoles, the two are combined in the same plane to make a new meta-atom, shown in the last two schematics in the bottom row of table 6.1. The second schematic in the bottom row shows the magnetic net dipole moment due to the fundamental resonance of the NB-SRR. The magnetic field profile corresponding to the fundamental magnetic mode of the new meta-atom, in a yz-plane dividing the meta-atom equally in half (with respect to the co-ordinate axes in table 6.1), is shown in figure 6.1b. The instantaneous magnetic field distribution (black arrow heads) justifies the out-of-plane magnetic dipole representation used in table 6.1, similar to that of the NB-SRR meta-atom. The last schematic in the bottom row shows the two orthogonal and independently excitable electric dipole moments due to the combined effect of the NB-SRR and the truncated hole resonator. The symmetric placement of the NB-SRR with respect to the x- and y-axes inside the truncated hole resonator supports the electric dipole moments of the meta-atom polarised parallel to the edges of the outer metallic square. Figures 6.1c and 6.1d show the electric field colour maps of the two orthogonal electric modes excited in the plane of the new meta-atom with black arrow heads showing instantaneous electric fields. It can be clearly seen that the region of electric field concentration is between the truncated hole resonator and the NB-SRR meta-atom. But from the relative directions of the electric field in both ends of the meta-atom for both the modes, it can clearly be seen that a simple electric field dipole representation as that shown in the last schematic in the bottom row of table 6.1 is valid for the purpose of qualitative analysis.

The schematics of the new meta-atom from table 6.1 show the in-plane and out-of-plane resonances as if they occur independently of one another. However, the excitation of counter-propagating electric currents in one resonator in response to an electric current driven in the other resonator at its resonance, causes the weakening of both their resonances. The discussion will return to this subject, later.

The non-bianisotropic nature of the resonances in the independent meta-atoms (NB-SRR and truncated hole resonator) results in a non-bianisotropic nature of the resonances of the resultant meta-atom. The dimensions of the individual constituents of the new meta-atom can be independently adjusted to tune the frequencies of the resonances, and therefore the frequency overlap between the resonant modes that result from the two kinds of interactions in a 1D metamaterial chain constructed with the meta-atoms. Given the hybrid nature of this new non-bianisotropic meta-atom's design, and the integral nature of the NB-SRR in influencing both the electric and magnetic resonances of the meta-atom, the name hybrid non-bianisotropic SRR (HNB-SRR) seems appropriate.

In section 6.3, the resonant response of the HNB-SRR meta-atom and the dispersion of the 1D metamaterial constructed from axial stacking of the HNB-SRRs will be numerically computed using the finite-element method.

6.3 Numerical modelling of the 1D metamaterial's resonant response

The resonant response of a single HNB-SRR meta-atom is first computed, followed by the dispersion in a 1D stacked metamaterial constructed from HNB-SRR meta-atoms. For comparison, the dispersions of a 1D stacked hole resonator metamaterial and a 1D stacked NB-SRR metamaterial will also be computed. Since, the nature of field interactions and wave propagation in axially stacked multilayer circular holes has already been treated in [48], for the experimental characterisation in this chapter only the NB-SRR and HNB-SRR meta-atoms are fabricated.

6.3.1 Resonant response of a HNB-SRR meta-atom

The design process for the HNB-SRR meta-atom to be used in this study was performed in the commercial finite element modelling software, COMSOL Multiphysics, using its eigenmode solver. A colour photograph of a fabricated HNB-SRR meta-atom is shown in figure 6.2b. The widths of the split-rings at the centre are $w_1 = w_2 = 1.2$ mm, the external radius of the outer split-ring is $r_{outer} = 16$ mm, the spacing between the inner and outer split-rings is $g_3 = 1.2$ mm, and the split-gaps in both the inner and outer split-rings is $g_1 = g_2 = 1.5$ mm. The radius of the circular hole in the truncated metal square is $r_{hole} = 17.2$ mm and the side of the square metal sheet is 34.8 mm. The minimum width of the metallic region between the circular hole and the edges of the square sheet (w_3 in figure 6.2b) is only 200 μm. The meagre metallic width in these regions as seen from figure 6.2b is intentional to enable easier detection of the magnetic near-field associated with the NB-SRR's resonance. This design choice does not qualitatively affect the nature of the electric dipole moments in the HNB-SRR meta-atom.

The meta-atoms were supported by the commercial Astra MT77 substrate ($\epsilon_r = 3(1 + 0.0017\text{i})$ in the frequency range 1 GHz to 20 GHz) which was 1.5 mm thick. This HNB-SRR meta-atom design has the following resonance frequencies as calculated using COMSOL: 1.7 GHz for the fundamental magnetic resonance, and 2.05 GHz and 2.19 GHz for the electric resonances. Referring to the last schematic in the bottom row of table 6.1, it can be seen that the electric fields polarised along the x- and y-directions

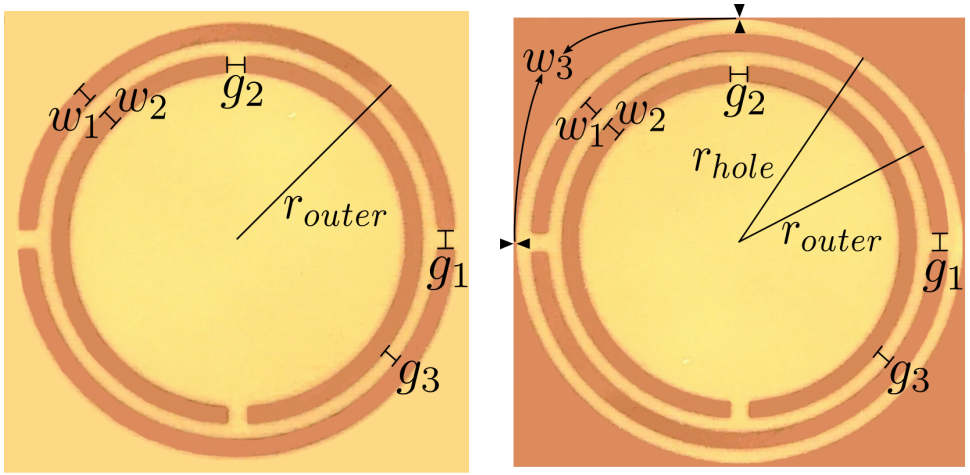

(a) **(b)**

Figure 6.2: Colour photographs of the (a) NB-SRR and (b) HNB-SRR meta-atoms as fabricated. The splits in both the inner and outer rings (g_1 and g_2) measure 1.5 mm in height and the rings themselves are 1.2 mm wide (w_1 and w_2). The outer split-rings in both meta-atoms have an external radius of 16 mm. The gap region between the inner and outer split-rings (g_3) is 1.2 mm wide. Specific to the HNB-SRR design, the circular hole of the truncated hole resonator has a radius of 17.2 mm and the metal square has a side measuring 34.8 mm. The minimum width of the metallic regions between the circular hole and metal square's edge (w_3 in (b)) measure 200 μm

experience slightly different metallic environments because of the inner and the outer rings in the centrally placed NB-SRR rotated by 90° relative to each other. Therefore the two electric resonances of the HNB-SRR meta-atom occur at slightly different frequencies.

Similar to the MNB-CSRR metamaterial studied in the previous chapter, in the 1D axially stacked HNB-SRR metamaterial the resonators are effectively embedded in substrate material. To see the effect of this environment on the resonance frequencies of a single resonator, a modified COMSOL eigenmode model was constructed with two Astra MT77 blocks 20 mm thick each, sandwiching a single HNB-SRR meta-atom. The meta-atom's resonance frequencies in this altered environment were found to be: 1.36 GHz for the fundamental magnetic resonance, and 1.62 GHz and 1.69 GHz for the electric resonances.

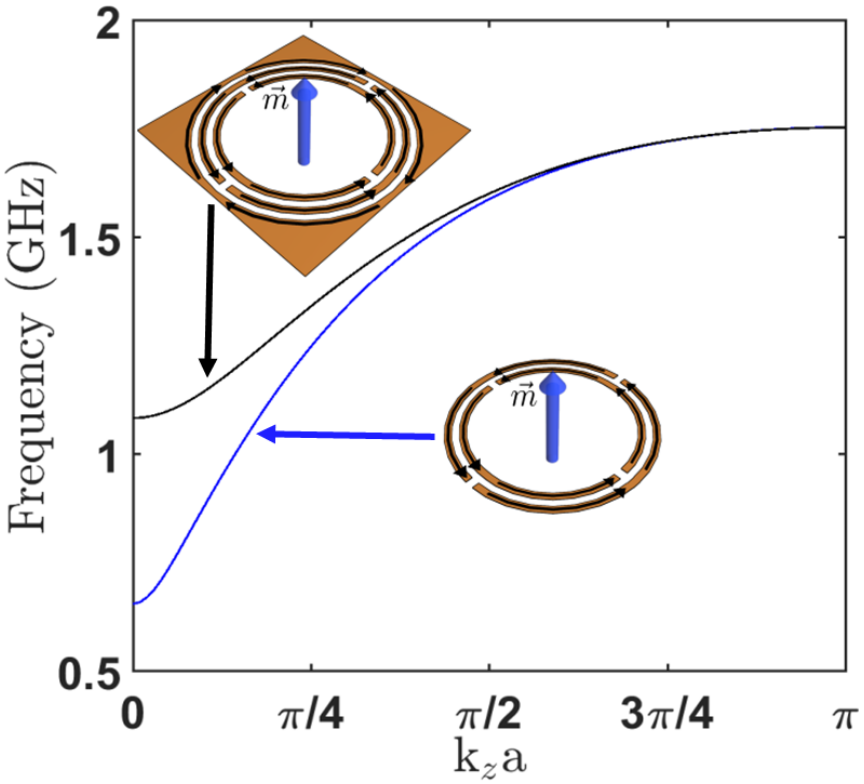

Figure 6.3: Numerically predicted resonant mode exhibiting positive dispersion in 1D axially stacked NB-SRR (blue curve) and HNB-SRR (black curve) metamaterials. The fractional bandwidth (FBW) of the HNB-SRR metamaterial stack's resonant passband is 47.2%, which is lower than the FBW of 64.5% for the NB-SRR metamaterial stack. Insets: instantaneous electric current distribution in individual meta-atoms of the NB-SRR (blue arrow) and the HNB-SRR (black arrow) metamaterial stacks associated with the resonances represented by the dispersion curves.

6.3.2 Dispersion characteristics of a HNB-SRR stacked 1D metamaterial

Before numerically modelling a 1D HNB-SRR metamaterial stack, 1D axial stacks of truncated hole resonators and NB-SRRs were modelled individually in COMSOL Multiphysics, for comparison. The truncated hole and the NB-SRR meta-atoms were designed using the same dimensions of the respective structures in the HNB-SRR meta-atom shown in figure 6.2b. A colour photograph of one of the fabricated NB-SRR meta-atoms is shown in figure 6.2a (note that the stacked hole resonator is not included in the experimental characterisation, as already mentioned). The axial/stacking direction of the metamaterials was chosen along the z-axis, with a stacking periodicity of 3 mm. The eigenmode solver in COMSOL was used to calculate the stacks' resonant modes in the frequency range from 1 GHz to 1.9 GHz as a function of wavevector along the stacking (z-) direction. Figures 6.3 and 6.4 show the dispersion diagrams of the stacked

1D NB-SRR array (blue curve) and the 1D stacked hole array (red curve) respectively, as a function of frequency and wavevector along the stacking direction.

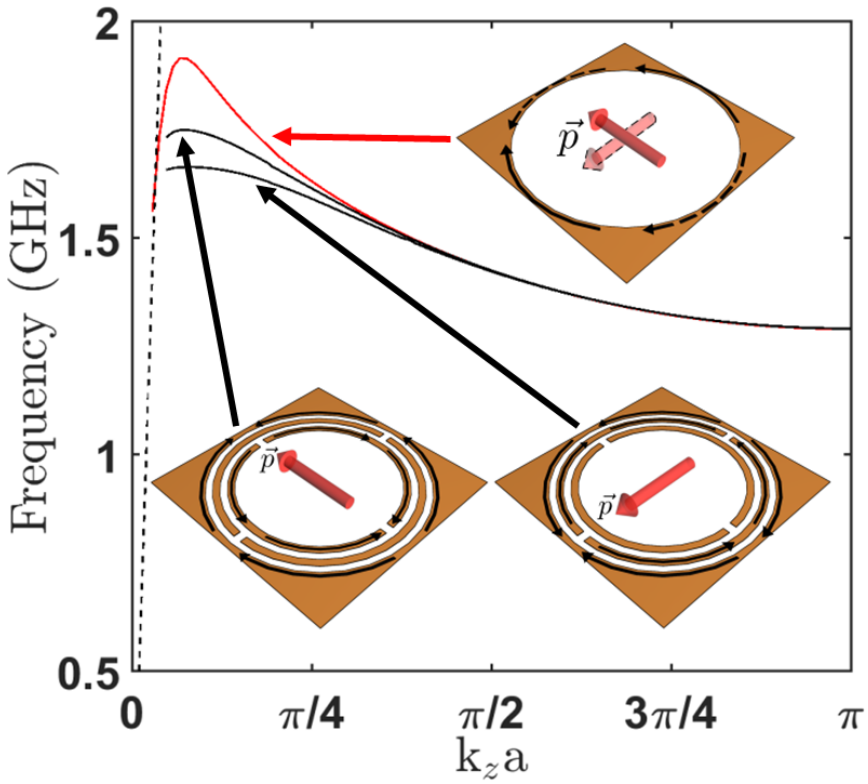

Figure 6.4: Numerically predicted resonant modes exhibiting negative dispersion in 1D axially stacked hole resonator (red curve) and HNB-SRR (black curves) metamaterials. The fractional bandwidth (FBW) of the HNB-SRR metamaterial stack's resonant passbands are 28.5% and 24.5% respectively, which are narrower in comparison to the FBW of 35.6% for the corresponding resonances in the hole resonator metamaterial stack. Insets: instantaneous electric current distributions in individual meta-atoms of the hole resonator (red arrow) and the HNB-SRR (black arrows) metamaterial stacks associated with the resonances represented by the dispersion curves.

The positive dispersion due to the longitudinal magnetic dipole interaction in the NB-SRR stack, as seen from the blue curve in figure 6.3 has a fractional bandwidth (FBW) (given by equation (5.1)) of 64.5%, which indicates a particularly strong inter-element interaction in the stack. The inset at the bottom of figure 6.3 shows the instantaneous electric current distribution and the excited magnetic dipole in a NB-SRR meta-atom of the stack at this resonance. The negative dispersion due to the transverse electric dipole interactions of the stacked holes, as seen from the red curve in figure 6.4 is composed of two identical curves associated with each of the electric dipole polarisations excitable in the stacked hole metamaterial. The inset at the top

of figure 6.4 shows the instantaneous electric currents corresponding to both electric polarisations that can be excited in a single truncated hole resonator. The solid black arrows represent the instantaneous electric current of the electric polarisation shown by the solid red arrow. Similarly, the broken black arrows correspond to the electric currents of the orthogonal electric polarisation, shown by the faint red arrow. Owing to the symmetric geometry of the truncated hole resonator, both the electric dipole resonances are degenerate and hence the identical dispersion. The FBW of the 1D stacked hole metamaterial as computed from the dispersion in figure 6.4 is 35.6%. The dotted black line in the modelled dispersion diagram of figure 6.4 represents the free-space light line. The dispersion curve of the 1D stacked hole metamaterial has an interesting trend as a function of wavevector. For small wavevector values, the curve shows a positive and linear gradient indicating the mode's interaction with some free space modes propagating along the direction of the stack. The negative dispersing character is exhibited for wavevectors away from the light line.

The next step in the analysis was to compute the dispersion of a 1D HNB-SRR axial metamaterial stack and examine the qualitative and quantitative changes that have occurred to the resonant response of this hybrid metamaterial, compared to that of the resonant responses from the individual stacked hole and stacked NB-SRR metamaterials. To visualise the dispersion characteristics of the 1D axially stacked HNB-SRR metamaterial, the stack was modelled as a periodic medium with the already mentioned design specifications using the eigenmode solver in COMSOL Multiphysics. The positive and the negative dispersing modes of the 1D HNB-SRR metamaterial stack computed by the numerical model are overlaid on the positive and negative dispersions in figures 6.3 and 6.4 respectively, for direct comparison.

Comparing the dispersions of the stacked hole and stacked NB-SRR metamaterials in figures 6.3 and 6.4 with that of the overlaid positive and negative dispersions of the HNB-SRR stack, a qualitative similarity in their nature is observed. The longitudinal magnetic dipole interactions in both the NB-SRR and the HNB-SRR stacks result in the positive dispersion in figure 6.3. Similarly, the negative dispersions due to the transversely coupled electric dipoles in the truncated hole resonator and the HNB-SRR stacks are comparable. The degeneracy of the negative dispersing modes in the stacked hole metamaterial is lifted in the HNB-SRR stack owing to the inclusion of NB-SRRs at the centre. This lifting of degeneracy is prominent especially at small wavevectors as seen from figure 6.4. This is to be expected following the observation that the electric resonances in the individual HNB-SRR meta-atoms were also non-degenerate. For higher wavevectors where the phase difference between the fields in neighbouring

resonators approaches π (π at $k_z = \pi/a$, the Brillouin zone boundary, with a being the stacking period), the fields are highly localised to the truncated hole regions of the HNB-SRR meta-atom with little or no role played by the NB-SRR component of the meta-atoms. The degeneracy of the negative dispersing modes is therefore restored at these higher wavevectors.

However, whilst qualitatively similar, it can be noted that the bandwidths of the positive and negative dispersing modes in the HNB-SRR metamaterial stack are narrower than that of the modes observed in the individual stacked hole resonator and the stacked NB-SRR metamaterials. The FBW of the HNB-SRR modes were calculated using the information from figures 6.3 and 6.4. The FBW of the positive dispersing mode was calculated as 47.2% while that of the negative dispersing modes were 28.5% and 24.5%. The reduction in the FBW of the HNB-SRR stack is simply due to the close proximity of the truncated hole and the NB-SRR to each other in the hybrid design of the meta-atoms.

When a resonance is excited in one of the individual components of the HNB-SRR (the truncated hole resonator or the NB-SRR), a counter-propagating electric current is excited in the other, as briefly mentioned in section 6.2. The inset at the top of figure 6.3 shows the instantaneous electric current distribution corresponding to the positive dispersing resonant mode (black curve) in a HNB-SRR meta-atom of the metamaterial stack. The counter-clockwise instantaneous current of the NB-SRR is countered by a clockwise instantaneous current in the hole resonator. The resulting net magnetic dipole moment is weaker than that in a NB-SRR meta-atom. Therefore, the inter-element interaction in the HNB-SRR metamaterial stack is weaker than that in the NB-SRR metamaterial stack and its FBW narrower. Similarly, the insets at the bottom of figure 6.4 represent the instantaneous electric currents in the HNB-SRR meta-atoms of the stack, corresponding to the two orthogonal electric polarisations. At either of these two resonances, the counter-propagating electric currents to the hole resonator's electric current are excited in a different split-ring of the NB-SRR (the inner or the outer), as seen in the bottom insets of figure 6.4. Consequently, the strengths of the two excited electric resonances are different and are both weaker than the resonances in just the truncated hole resonator. Therefore, both these negative dispersing resonances of the 1D HNB-SRR have a narrower FBW compared to those in the 1D stacked hole metamaterial. This difference between the resonance strengths in the HNB-SRR meta-atoms and the corresponding resonance in the individual NB-SRR/hole resonator reflects as different inter-element interaction strengths in the 1D stacked HNB-SRR metamaterial and the individual 1D stacked NB-SRR/hole metamaterials. Therefore,

the difference in FBW values is observed in both the positive and negative dispersing resonant modes. At the higher wavevectors, as explained already, due to the high field localisation to the NB-SRR or the hole resonator components of the HNB-SRR, the dispersions of the respective compared resonances are identical, as seen from figures 6.3 and 6.4.

6.4 Experimental realisation and characterisation of a 1D stacked HNB-SRR metamaterial

NB-SRR and HNB-SRR meta-atoms were fabricated to construct the respective 1D metamaterial axial stacks to experimentally characterise their dispersion relations, the results of which are presented in this section.

6.4.1 Fabrication

2D arrays of NB-SRRs and HNB-SRRs were fabricated commercially by a local PCB manufacturer Graphic PLC, on a 1.5 mm thick commercial Astra MT77 substrate clad with 35 μm of copper. A layer of photoresist was coated on top of the copper layer and the design of the meta-atoms transferred into the resist by laser direct imaging. The subsequent development of the photoresist followed by etching of the resulting exposed metal using ferric chloride were performed as described in section 3.2 of chapter 3. The individual meta-atoms were cut from the panels, and the 1D metamaterials were constructed by axially stacking 90 meta-atoms with a periodicity of 3 mm (the meta-atoms alternate the stack with intermediate 1.5 mm thick blank Astra MT77 substrate squares), as shown in figures 6.5a and 6.5b.

The magnetic mode supported by the 1D NB-SRR metamaterial stack was excited via the near-field using a loop antenna positioned for optimum coupling, as shown in figure 6.5a. A second loop antenna was used to probe the excited magnetic near-field above the metamaterial stack as a function of distance along the stack direction shown by the dashed red arrows. The orientation of the probing loop antenna was co-axial with the input loop antenna, so as to pick up the axial magnetic fields of the metamaterial stack. Both the launch antenna and the collection probe were connected to the ports of a VNA. The coaxial probe recorded the local magnetic field strength in the frequency range of 1 GHz to 1.9 GHz.

The experimental arrangement for the HNB-SRR stack was different from that of the NB-SRR stack, as can be seen from figure 6.5b. The motivation here was

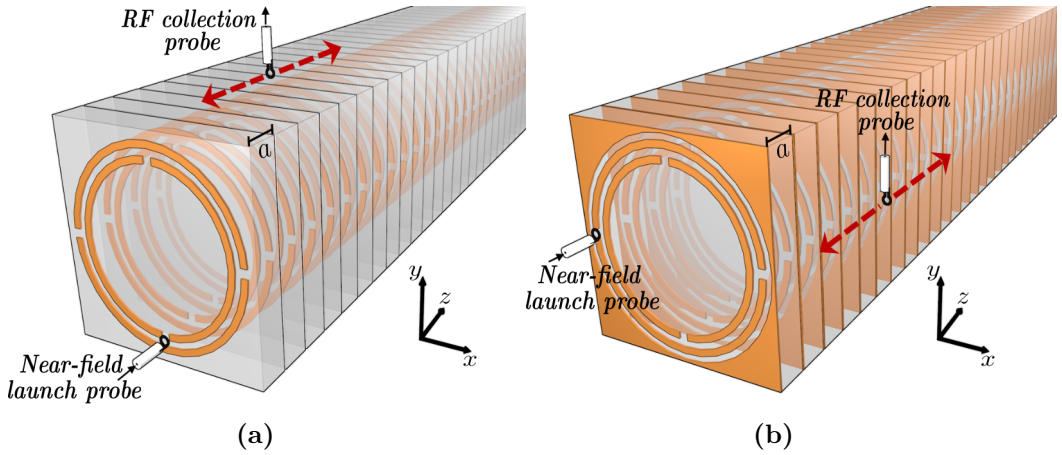

Figure 6.5: Schematics of experimental setups used to excite and detect the modes of the (a) one-dimensional stacked NB-SRR metamaterial and (b) one-dimensional stacked HNB-SRR metamaterial, with period $a = 3$ mm. The substrate material has been rendered translucent to reveal the periodic structures. A near-field loop antenna excites the magnetic near-field of the 1D metamaterial stacks, and a second loop antenna traverses the length of the stack to probe and record the magnetic near-field, along the z-direction (shown dashed red). Both the launch antenna and the probe are connected to a VNA.

to deliberately excite and detect both the positive dispersing mode and one of the negative dispersing modes simultaneously and visualise the metamaterial's dispersion. The exciting loop antenna was positioned optimally to couple into the axial magnetic field of the NB-SRR's magnetic mode and the local magnetic near-field of the broader of the two negative dispersing modes, as seen in figure 6.5b. The detecting loop antenna was positioned co-axially to the input loop antenna and probed the local magnetic field strength in the frequency range of 1 GHz to 1.9 GHz. In the HNB-SRR metamaterial stack, the challenge was to detect the magnetic fields of the NB-SRR component, which is mostly localised through the centre of the metamaterial waveguide. Making the minimum edge metallic width on the outer truncated hole resonator just 200 μm, and using a stacking periodicity of 3 mm allowed us to probe the small proportion of field leaked outside of the chain from this mode.

6.4.2 Experimental characterisation of the 1D metamaterial stack

As described in section 5.3.2 of chapter 5, the Fourier transforms of the spatial magnetic field maps from the NB-SRR stack were combined to plot the dispersion diagram in figure 6.6. The numerically predicted mode dispersion from COMSOL is overlaid on the experimental data as red triangular markers in figure 6.6. The excited mode exhibits a positive gradient and is in good agreement with the numerical prediction, confirming our understanding of the field interactions in the NB-SRR stack.

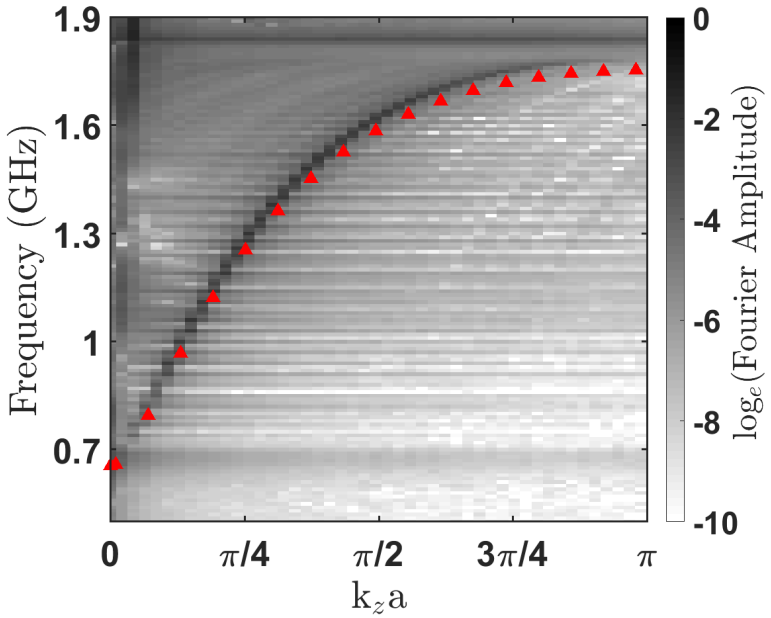

Figure 6.6: Fourier amplitude of the complex spatial magnetic field map of the NB-SRR stack, plotted as a function of frequency and wavevector along the stacking direction. The red triangles indicate the mode positions predicted by the eigensolver in COMSOL Multiphysics for the NB-SRR stack.

The Fourier transforms of the spatial magnetic field maps from the HNB-SRR stack, are combined in the dispersion diagram in figure 6.7. The dispersion shows both positive and negative dispersing modes as expected. The two modes do not exhibit anti-crossing, confirming that they are independent of one another. The numerically predicted dispersions are overlaid as red and blue triangular markers, respectively. The experimental observation appears to be in excellent agreement with the numerical prediction.

This is a first demonstration of a 1D metamaterial with simultaneous positive and negative dispersion along the same direction and in an overlapping frequency band. It is to be noted that simultaneous positive and negative dispersion in an overlapping frequency band by a metamaterial device has been reported in 3D, in literature [152–154]. 2D metasurfaces of modified square hole resonators are stacked to form the 3D structure (fishnet metamaterial) which offers a positive or a negative dispersion in an overlapping frequency band depending on the polarisation of an incident electromagnetic wave. The metamaterial design reported in this chapter shares similarity with that of the 3D fishnet metamaterial from these works in that it also supports two orthogonal electric polarisations. However, both these orthogonal polarisations in our

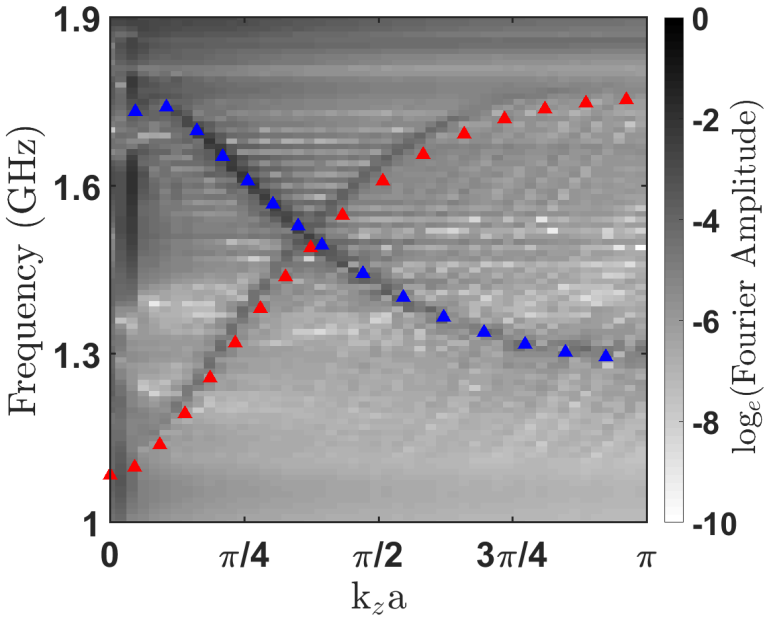

Figure 6.7: Fourier amplitude of the complex spatial magnetic field map of the HNB-SRR stack, plotted as a function of frequency and wavevector along the stacking direction. The red and blue triangles indicate the mode positions predicted by the eigensolver in COMSOL Multiphysics for the positive and negative dispersing modes respectively. The positive and negative dispersing modes are simultaneously detected with no indications of interactions with each other (no anti-crossing).

metamaterial offer a negative dispersion. By virtue of the hybrid geometry, a positive dispersing resonant mode in accommodated in the metamaterial through the NB-SRR inclusions. We have reported simultaneous near-field excitation and detection of positive and negative dispersing electromagnetic modes in a hybrid metamaterial, in an overlapping frequency band.

Further to the analysis of the positive and negative dispersing resonant modes in the NB-SRR, truncated hole and the HNB-SRR stacks, the group velocities of the corresponding resonant modes are also compared in figure 6.8. Figure 6.8a shows the group velocities of the positively dispersing resonant modes in the stacked NB-SRR and HNB-SRR stacks, respectively. It was shown in figure 6.3 that the FBW of the resonant mode in the HNB-SRR stack was reduced compared to that in the NB-SRR stack owing to weakened resonance strength and consequently reduced inter-element interaction strength. This weakened interaction strength is also reflected as reduced group velocity in the HNB-SRR stack at the small wavevectors.

Figure 6.8b shows the group velocities of the negatively dispersing modes in the truncated hole and the HNB-SRR stacks. Similar to the group velocity plot of figure

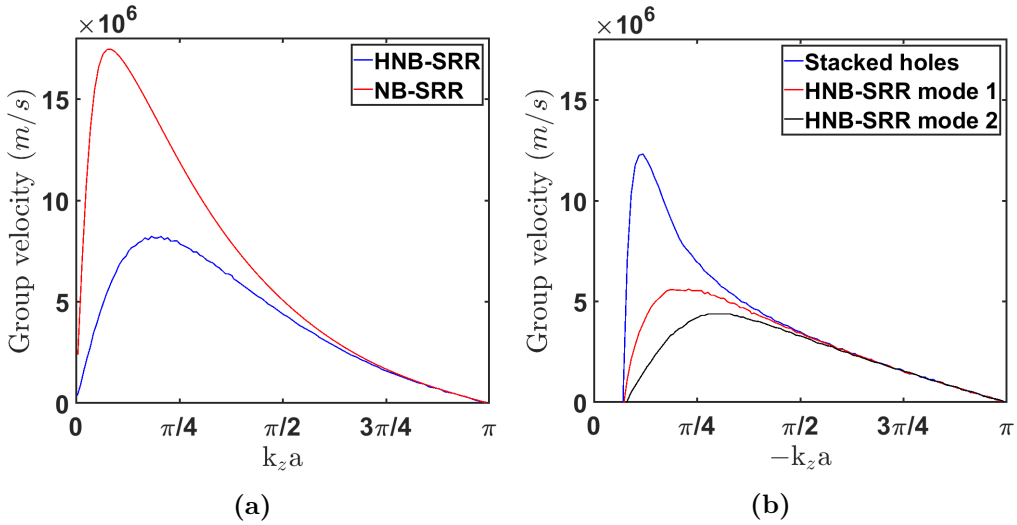

Figure 6.8: (a) The group velocity for the positively dispersive modes of the NB-SRR (red curve) and HNB-CSRR (blue curve) 1D stacks as a function of wavevector in the stacking direction. (b) The group velocity for the negatively dispersive mode of the truncated hole resonator 1D stack (blue curve) and the two orthogonal negatively dispersing modes of the HNB-CSRR 1D stack (blue and black curves) as a function of wavevector in the stacking direction. The group and phase velocities represented in (b) are oppositely directed and hence the negative scale on the wavevector axis.

5.4 in chapter 5, the group velocity and the wavevector axes have opposite signs for the negatively dispersing modes. Like in figure 6.8a, it can be seen that the FBW of the modes and hence the inter-element interaction strength have a direct relationship to the group velocity. As one might expect, the group velocities of the two orthogonal negative dispersive modes of the HNB-SRR stack are smaller than that in the stacked hole metamaterial. Comparing these to the group velocity of the positive dispersing mode of the HNB-SRR in figure 6.8a, it is observed that the group velocity of the signals that could propagate forwards and backwards in the waveguide would do so with different group velocities. They can be tuned to be equal by appropriate adjustments to the design parameters.

The attenuation of the positive and negative dispersing modes were calculated using the same procedure as in chapter 5, for a periodicity of 3 mm. The results are shown in figure 6.9. It is clearly visible that the band of attenuation is directly related to the observed bandwidth of the corresponding modes. The attenuation corresponding to the magnetic mode (shown by the blue data points) is lower than that we observed for the MNB-CSRR metamaterial stack of the last chapter, with a minimum attenuation of 1.12 dB/m observed at 1.23 GHz. The attenuation is below 3 dB/m (50%) for the frequency range of 1 GHz to 1.61 GHz. Such a low attenuation is not surprising given the

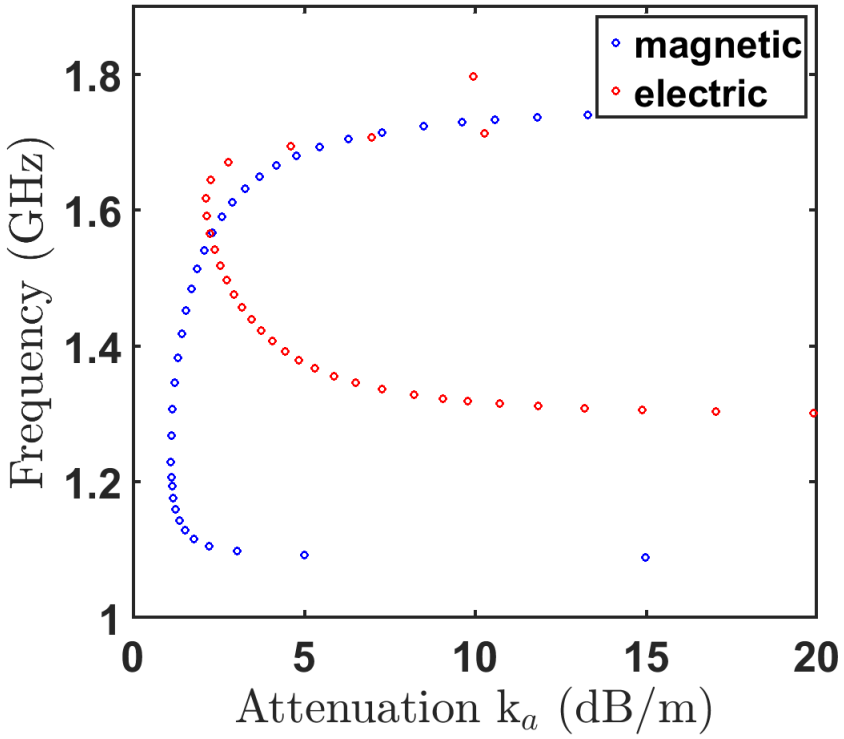

Figure 6.9: The attenuation of the HNB-SRR metamaterial waveguide with period $a = 3$ mm. The blue dots represent the attenuation of the magnetic mode and the red dots that of the electric mode, both calculated from the numerically computed dispersion shown in figure 6.7 and the corresponding group velocities shown in figure 6.8. The lowest attenuation of 1.12 dB/m is observed at the frequency of 1.23 GHz for the magnetic mode. The electric mode is more lossy with a minimum attenuation of 2.15 dB/m observed at the frequency of 1.62 GHz.

fact that the magnetic mode due to the NB-SRR's resonance is localised to the centre of the waveguide,a long which it propagates. The periodicity for the experiment had to be set at 3 mm to deliberately increase field leakage at the sides of the metamaterial stack and pick it up with a near-field magnetic probe. It can be confidently stated that reducing the periodicity of the metamaterial stack further will greatly reduce the attenuation of the HNB-SRR's magnetic mode.

Attenuation is calculated for only the electric mode that was characterised in the experiment along with the magnetic mode. The corresponding attenuation data points are shown in red in figure 6.9. It is not surprising that the attenuation of this mode is compared to that of the magnetic mode, because 1) the truncated hole resonator being positioned on the outer portion of the waveguide would lose more energy than the NB-SRR components at the centre, and 2) the resonant mode of the truncated

hole resonator as we saw in the first section easily couples to free-space radiation and therefore has a radiative loss channel along the direction of the stack. Given all these reasons, the lowest attenuation observed for the electric mode is 2.15 dB/m at the frequency of 1.62 GHz. The low loss propagation band is also narrower for this mode. Just like for the magnetic mode, reducing the longitudinal periodicity will result in reduced attenuation and increased bandwidth for the mode.

Similar to the observation in chapter 5, the attenuation of the two modes at their respective band edges is unrealistically high which is unavoidable in computation, as discussed already. Given the frequency overlap of the two modes as is, the frequency points at which either of their lowest attenuation occurs is separated. By appropriate tuning of the design parameters, if both the modes are shifted such that their lowest attenuations occur at the same frequency, then low-loss bidirectional waveguiding can be improved. The results from this study offer a new recipe for the creation of wideband metamaterial waveguides that support simultaneous bidirectional guiding of non-interfering waves, which maybe of assistance in bidirectional power transfer applications in an overlapping frequency range.

6.5 Sensitivity to change in longitudinal periodicity

As a last study on the HNB-SRR metamaterial stack, the change in behaviour of the resonant modes as a function of changing longitudinal/stacking periodicity was computed numerically. The positive dispersing mode and the specific negative dispersive mode that was excited along with the positive dispersing mode in the experiment were studied by setting the period values to 'a' = 1.5 mm, 3 mm, 6 mm, and 10 mm. The results of the study are plotted in figure 6.10.

The pair of the positive and negative dispersing resonant modes studied always have the same crossing point of 1.5 GHz. This frequency will change only if the positive or the negative dispersing mode's resonance frequency is tuned by manipulating the design parameters. It is seen from figure 6.10 that increasing the periodicity naturally decreases the interaction strength among meta-atoms in the 1D stack resulting in a reduction in their fractional bandwidths. Besides tuning the bandwidths of the resonant modes, the wavevector at which both the resonant modes become degenerate (the crossing point) is also tuned. At a periodicity of 10 mm, the frequency overlap is avoided and a bandgap is opened.

Though we experimentally demonstrated the simultaneous excitation of both the

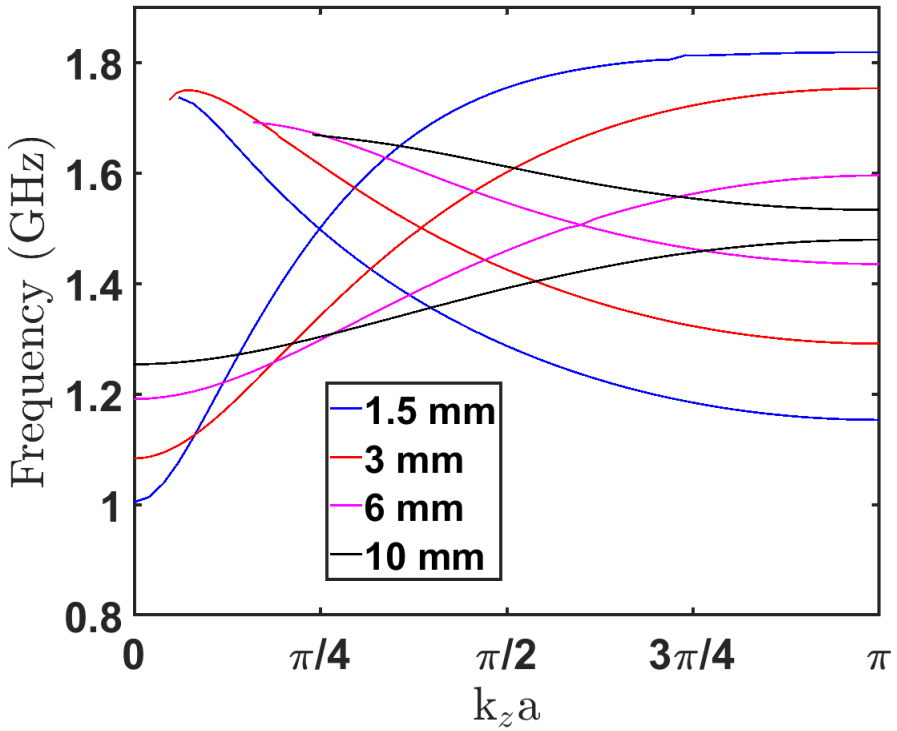

Figure 6.10: Numerically computed dispersion relations for the 1D metamaterial stack built from HNB-SRR meta-atoms, as a function of changing longitudinal periodicity. The dispersion relations were computed for periods 'a'=1.5 mm, 3 mm, 6 mm and 10 mm.

resonant modes at a periodicity of 3 mm for convenience of field detection, it is seen that by reducing the periodicity to 1.5 mm improves the fractional bandwidth of the modes and thereby increases the frequency overlap of operation. This section of the study will be valuable to understand how tuning the longitudinal periodicity can help tune the operational characteristics of the HNB-SRR metamaterial waveguide.

6.6 Summary

The resonances of non-bianisotropic meta-atoms exhibiting isolated in-plane and out-of-plane dipole moments were analysed. Following this, a hybrid meta-atom (HNB-SRR) was created by combining a non-bianisotropic SRR (NB-SRR) meta-atom with a truncated metallic hole resonator. The resonant modes exhibited by the 1D stacked metamaterial constructed from HNB-SRR meta-atoms had narrower fractional bandwidths compared to the corresponding resonances in just the stacked hole metamaterial and the stacked NB-SRR metamaterial. The reason was found to be the weakening of the resonances in the HNB-SRR resulting from its hybrid geometry. The NB-SRR and HNB-SRR stacks were experimentally realised and characterised. The HNB-SRR

stack was found to simultaneously accommodate both positive and negative dispersing modes in an overlapping frequency band. The two resonant modes show no sign of coupling to each other (no anti-crossing), which may make the design suitable for realising bidirectional wireless power transfer applications. The magnetic mode associated with the NB-SRR components of the waveguide exhibits very low propagation loss owing to localisation to the centre of the waveguide. The electric mode on the other hand is more lossy, but can be controlled by tuning the longitudinal periodicity. Tuning the design parameters should also enable tuning the frequency of lowest attenuation in each resonance to coincide, to achieve low loss propagation in both resonances simultaneously. Finally, the sensitivity of the HNB-SRR stack with respect to changing longitudinal periodicity was studied. Tuning the period helps change the wavevector at which both the modes become degenerate, while maintaining the frequency. This tuning also simultaneously controls the operational bands and consequently the frequency overlap between the two resonant modes.

Chapter 7

Conclusions and future work

7.1 Conclusions

The work in the initial part of this thesis presented a full characterisation and detailed analysis of electromagnetic interactions in bianisotropic split-ring resonator dimers, which had not been provided in literature. The subsequent work in the thesis built on the understanding of electromagnetic interactions between meta-atoms to propose design modifications and new hybrid designs of meta-atoms. These meta-atoms were employed to build 1D metamaterial stacks with novel electromagnetic responses that either improve over the limitations of metamaterial structures proposed in literature or are the first to be observed. The metamaterial designs proposed in this thesis could be of valuable assistance in developing novel metamaterials in magneto- and electro-inductive waveguiding, and wireless power transfer applications.

In chapter 4, the nature of electromagnetic interactions between two identical bianisotropic split-ring resonators were analysed experimentally and analytically, as a function of changing separation and relative rotation angle. While, a simple coupled-dipole model suffices to explain the resonant behaviour of the coupled SRRs at separations comparable to the resonant wavelength, it starts to fall apart at sub-wavelength separations because of its failure to account for near-field effects. The developed analytical model's results agree well with that of the experiments and help explain the rich coupling behaviour exhibited due to the competition or concert between electric and magnetic interactions in the dimer. The work in this chapter adds to the currently existing knowledge on bianisotropy by showing that it is a highly disadvantageous feature that limits inter-element interaction strength in metamaterial systems and will help inform the design of more complex metamaterials with densely packed arrays where the strength of inter-resonator coupling becomes significant.

In chapter 5, a modified non-bianisotropic complementary SRR design was proposed, to overcome the limitations imposed by bianisotropy and to widen the maximum achievable bandwidth of negatively dispersing metamaterials. The comparison of bandwidths between 1D axially stacked metamaterial waveguides constructed from the bianisotropic CSRR and the modified non-bianisotropic CSRR (MNB-CSRR) meta-atoms showed that the modified design indeed sustains stronger inter-element interactions. The MNB-CSRR metamaterial exhibited a fractional bandwidth of 56.3% (ultra wideband) which is wider than that of the CSRR metamaterial (41.5%) for the same lattice periodicity and that of any report that could be found in the literature. The MNB-CSRR metamaterial stack also showed less sensitivity to changing lattice period. A simple toy coupled-dipole model was employed to explain the origin of negative dispersion in the stacked CSRR based metamaterials and to demonstrate the limiting effects of bianisotropy on a metamaterial's operational bandwidth. It will add to prior knowledge obtained through equivalent circuit modelling. The results from this study should be of assistance in the design of broadband metamaterial devices in such applications as wireless power transfer.

In chapter 6, a 1D metamaterial waveguide that supports the simultaneous existence of positive and negative dispersing modes in an overlapping frequency band was successfully designed and experimentally demonstrated. The waveguide is constructed by axially stacking a newly designed hybrid meta-atom, composed of a non-bianisotropic SRR (NB-SRR) and a truncated hole resonator, both combined in the same plane. The positive and negative dispersing modes of the metamaterial showed no sign of coupling to each other, which may make the design suitable for realising bidirectional wireless power transfer applications. The hybrid geometry's drawback was that the individual components (the truncated hole resonator and the NB-SRR) of the hybrid meta-atom weakened each others' resonances, which resulted in a reduced bandwidth of the modes compared to those in just a 1D stacked hole waveguide or a 1D stacked NB-SRR waveguide. Alternative strategies need to be adopted to counter this in future designs.

7.2 Future Work

1. **Further development of the analytical model:** The analytical model developed in chapter 4 accurately calculates the resonance frequencies of the SRR dimer's coupled modes and the coupling coefficients. The real parts of the coupling coefficients were used to quantify the strength of electric and magnetic

interactions in the SRR dimer and to analyse its changing resonant response. The imaginary parts of the coupling coefficients represent damping and are important for predicting the lineshapes of the resonant modes. While the prediction of resonance lineshapes could easily be achieved using finite element modelling, developing the analytical model further to include damping would increase its applicability, which could be the subject of a future study. The analytical model could also be extended to predict the resonant modes of 1D periodic, biperiodic and quasi-disordered N-resonator systems.

2. **Boosting the operational bandwidth of the hybrid metamaterial waveguide:** The hybrid metamaterial waveguide designed and demonstrated in chapter 6 was the first of its kind, supporting the simultaneous existence of forward-propagating and backward-propagating resonances that do not couple to each other, in an overlapping wide frequency band. However, this bidirectional metamaterial waveguide suffered from a shortcoming. The generation of counter-propagating electric currents in one of the meta-atoms' components in response to the resonance excited in the other, weakened the inter-element interaction strength and narrowed the operational bandwidth over which the bidirectional guiding occurs. Since the generation of counter-propagating currents is an inductive effect, an immediate solution to this issue may be to establish a conductive (metallic) contact between the stacked hole and the NB-SRR components of the hybrid meta-atom. The conductive contact between the components would be made so as to maintain the polarisations of the individual resonances and avoid interaction between the modes. However, the existence of counter-propagating electric currents would be prohibited.

3. **Modifying the properties of the hybrid metamaterial waveguide:** The simultaneous non-interacting propagation of positive and negative dispersing modes in the hybrid metamaterial waveguide was by itself a novel feature. By suitably modifying the hybrid meta-atom's geometry, the hybrid waveguide can also be turned into a slow-wave structure. As it was showed in chapter 6, the two non-interacting resonances arise from the individual non-bianisotropic components of the waveguide. A direct approach to achieve this may be by breaking the inversion symmetry of the meta-atom and deliberately introducing bianisotropy. For example, by shifting the splits of the split-ring to make it asymmetric along a single direction in its plane, the previously purely magnetic resonance could be made to have an additional in-plane electric dipole moment as a consequence of cross-polarisation. When the positive and negative dispersing modes interact as a consequence and anti-cross in the dispersion, regions of flat dispersion

could be observed in the anti-crossing region at low wavevectors, where standing waves would be set up in the medium. Zero gradient is a common observation at the Brillouin zone boundary of the dispersion diagram as a consequence of field localisation and a lack of interaction between meta-atoms. But, setting up a standing wave via interaction of counter-propagating forward and backward dispersing waves in the medium, could be a unique feature of the modified hybrid metamaterial waveguide.

4. **Design of graded-index metamaterial profiles:** The general theme of the study in this thesis has been periodic and symmetric designs of meta-atoms used to construct metamaterial waveguides. A periodic medium's dispersion relation maybe used to determine the mode index profile of the medium, which is the frequency dependent refractive index arising from the medium's dispersive nature. A step ahead, in moving away from the periodic design, would be to take building blocks out of several periodic media and skillfully assemble them in such a way to synthesise a graded index 1D metamaterial. An example application could be to design a reflectionless metamaterial based on the so-called Poschl-Teller [155] or $sech^2$ [156] refractive index profiles that exhibits 100% transmission for a design frequency. The success of such a metamaterial medium requires in-depth analysis of several key factors - the number of meta-atoms of a kind required per building block for the block itself to act as a local effective medium, the size and periodicity of each building block, and the maximum tolerance in the change of mode index between two adjacent building blocks, to name only a few.

Chapter 8

Publications and Conferences

8.1 Publications

- SEETHARAMAN, S. S., KING, C. G., HOOPER, I. R., and BARNES, W. L., Electromagnetic interactions in a pair of coupled split-ring resonators, *Physical Review B* **96**, 085426 (2017)

- SEETHARAMAN, S. S., TREMAIN, B. J., BARNES, W. L., and HOOPER, I. R., Realizing an ultra-wideband backward-wave metamaterial waveguide, Submitted June 2018, *Physical Review B*

8.2 Presentation and Conferences

8.2.1 Oral Presentations

- Talk at CIMTEC international congress, SEETHARAMAN, S. S., HOOPER, I. R., and BARNES, W. L., Exploring the interactions in systems of densely packed split-ring resonators, Perugia, Italy, June 2016

8.2.2 Poster Presentations

- Royal Society Conference - New horizons in nanophotonics, SEETHARAMAN, S. S., HOOPER, I. R., and BARNES, W. L., Electromagnetic interactions in a pair of coupled split-ring resonators, Chicheley Hall, Buckinghamshire, May 2016

- Metamaterials Winter School, SEETHARAMAN, S. S., HOOPER, I. R., and BARNES, W. L., Electromagnetic interactions in a pair of coupled split-ring resonators, Ruka, Finland, December 2016

- Exeter Oversight Board Poster Session, SEETHARAMAN, S. S., TREMAIN, B. J., BARNES, W. L., and HOOPER, I. R., Realizing an ultra-wideband backward-wave metamaterial waveguide, Exeter, February 2018

References

[1] Woodyard, J.R. *Nonlinear circuit device utilizing Germanium*, United States Patent Office, US2530110A (1944). 6

[2] Lamb, H. On Group-Velocity. *Proceedings of the London Mathematical Society*, **s2-1**, 473 (1904). 6

[3] Pocklington, H.C. Growth of a Wave-group when the Group-velocity is Negative. *Nature*, **71**, 607 (1905). 6

[4] Schuster, A. *An Introduction to the Theory of Optics*. Edward Arnold, London (1904). 6

[5] Veselago, V.G. The electrodynamics of substances with simultaneously negative values of ϵ and μ. *Soviet Physics Uspekhi*, **10**, 509 (1968). v, 6, 7, 9, 81

[6] Abbe, E. VII - On the Estimation of Aperture in the Microscope. *Journal of the Royal Microscopical Society*, **1**, 388 (1881). 7

[7] Bracewell, R.N. Analogues of an ionized medium, applications to the ionosphere. *Wireless Engineer*, **31**, 320 (1954). 7, 9

[8] Rotman, W. Plasma simulation by artificial dielectrics and parallel-plate media. *IRE Transactions on Antennas and Propagation*, **10**, 82 (1962). 7, 9

[9] Pendry, J.B., Holden, A.J., Stewart, W.J., and Youngs, I. Extremely low frequency plasmons in metallic mesostructures. *Phys. Rev. Lett.*, **76**, 4773 (1996). 7

[10] Pendry, J.B., Holden, A.J., Robbins, D.J., and Stewart, W.J. Low frequency plasmons in thin-wire structures. *Journal of Physics: Condensed Matter*, **10**, 4785 (1998). 7

[11] Schneider, H.J. and Dullenkopf, P. Slotted tube resonator: A new NMR probe head at high observing frequencies. *Review of Scientific Instruments*, **48**, 68 (1977). 8, 106

[12] Hardy, W.N. and Whitehead, L.A. Split-ring resonator for use in magnetic resonance from 200-2000 MHz. *Review of Scientific Instruments*, **52**, 213 (1981). 8, 106

[13] Pendry, J.B., Holden, A.J., Robbins, D.J., and Stewart, W.J. Magnetism from conductors and enhanced nonlinear phenomena. *IEEE Trans. Microw. Theory Tech.*, **47**, 2075 (1999). v, vi, 8, 11, 15, 16, 17, 63, 82, 84, 86

[14] Smith, D.R., Vier, D.C., Kroll, N., and Schultz, S. Direct calculation of permeability and permittivity for a left-handed metamaterial. *Applied Physics Letters*, **77**, 2246 (2000). v, 8, 9, 81

[15] Smith, D.R., Padilla, W.J., Vier, D.C., Nemat-Nasser, S.C., and Schultz, S. Composite Medium with Simultaneously Negative Permeability and Permittivity. *Phys. Rev. Lett.*, **84**, 4184 (2000). 9, 17, 18, 63

[16] Shelby, R.A., Smith, D.R., Nemat-Nasser, S.C., and Schultz, S. Microwave transmission through a two-dimensional, isotropic, left-handed metamaterial. *Applied Physics Letters*, **78**, 489 (2001). 9

[17] Shelby, R.A., Smith, D.R., and Schultz, S. Experimental verification of a negative index of refraction. *Science*, **292**, 77 (2001). 63

[18] Parazzoli, C.G., Greegor, R.B., Li, K., Koltenbah, B.E.C., and Tanielian, M. Experimental verification and simulation of negative index of refraction using snell's law. *Phys. Rev. Lett.*, **90**, 107401 (2003).

[19] Ozbay, E., Aydin, K., Cubukcu, E., and Bayindir, M. Transmission and reflection properties of composite double negative metamaterials in free space. *IEEE Transactions on Antennas and Propagation*, **51**, 2592 (2003).

[20] Houck, A.A., Brock, J.B., and Chuang, I.L. Experimental observations of a left-handed material that obeys snell's law. *Phys. Rev. Lett.*, **90**, 137401 (2003). 9

[21] Syms, R.R.A., Shamonina, E., Kalinin, V., and Solymar, L. A theory of metamaterials based on periodically loaded transmission lines: Interaction between magnetoinductive and electromagnetic waves. *Journal of Applied Physics*, **97**, 064909 (2005). 9, 81, 103

[22] Shamonina, E., Kalinin, V., Ringhofer, K.H., and Solymar, L. Magnetoinductive waveguide. *Electronics Letters*, **38**, 371 (2002). 9, 10, 26, 27, 63, 81, 103

[23] Shamonina, E., Kalinin, V.A., Ringhofer, K.H., and Solymar, L. Magnetoinductive waves in one, two, and three dimensions. *Journal of Applied Physics*, **92**, 6252 (2002). 9, 10, 23, 26, 27, 28, 29, 63, 81, 82, 103

[24] Freire, M.J. and Marqués, R. Planar magnetoinductive lens for three-dimensional subwavelength imaging. *Applied Physics Letters*, **86**, 182505 (2005). 9, 10, 82

[25] Sydoruk, O., Shamonin, M., Radkovskaya, A., Zhuromskyy, O., Shamonina, E., Trautner, R., Stevens, C.J., Faulkner, G., Edwards, D.J., and Solymar, L. Mechanism of subwavelength imaging with bilayered magnetic metamaterials: Theory and experiment. *Journal of Applied Physics*, **101**, 073903 (2007). 9, 10, 82, 103

[26] Stevens, C.J. Magnetoinductive waves and wireless power transfer. *IEEE Transactions on Power Electronics*, **30**, 6182 (2015). 9, 10, 26, 82

[27] Leonhardt, U. Optical conformal mapping. *Science*, **312**, 1777 (2006). 10

[28] Leonhardt, U. and Philbin, T.G. General relativity in electrical engineering. *New Journal of Physics*, **8**, 247 (2006).

[29] Schurig, D., Mock, J.J., Justice, B.J., Cummer, S.A., Pendry, J.B., Starr, A.F., and Smith, D.R. Metamaterial electromagnetic cloak at microwave frequencies. *Science*, **314**, 977 (2006). 10

[30] Liu, Z., Fang, N., Yen, T., and Zhang, X. Rapid growth of evanescent wave by a silver superlens. *Applied Physics Letters*, **83**, 5184 (2003). 10

[31] Fang, N. and Zhang, X. Imaging properties of a metamaterial superlens. *Applied Physics Letters*, **82**, 161 (2003).

[32] Grbic, A. and Eleftheriades, G.V. Overcoming the diffraction limit with a planar left-handed transmission-line lens. *Phys. Rev. Lett.*, **92**, 117403 (2004).

[33] Fang, N., Lee, H., Sun, C., and Zhang, X. Sub-diffraction-limited optical imaging with a silver superlens. *Science*, **308**, 534 (2005).

[34] Podolskiy, V.A., Kuhta, N.A., and Milton, G.W. Optimizing the superlens: Manipulating geometry to enhance the resolution. *Applied Physics Letters*, **87**, 231113 (2005).

[35] Wood, B., Pendry, J.B., and Tsai, D.P. Directed subwavelength imaging using a layered metal-dielectric system. *Phys. Rev. B*, **74**, 115116 (2006).

[36] Belov, P.A. and Hao, Y. Subwavelength imaging at optical frequencies using a transmission device formed by a periodic layered metal-dielectric structure operating in the canalization regime. *Phys. Rev. B*, **73**, 113110 (2006). 10

[37] Sample, A.P., Meyer, D.T., and Smith, J.R. Analysis, experimental results, and range adaptation of magnetically coupled resonators for wireless power transfer. *IEEE Transactions on Industrial Electronics*, **58**, 544 (2011). 10

[38] Chen, J.F., Ding, Z., Hu, Z., Wang, S., Cheng, Y., Liu, M., Wei, B., and Wang, S. Metamaterial-Based High-Efficiency Wireless Power Transfer System at 13.56 MHz for Low Power Applications. *Progress In Electromagnetics Research B*, **72**, 17 (2017).

[39] Sun, K., Fan, R., Zhang, X., Zhang, Z., Shi, Z., Wang, N., Xie, P., Wang, Z., Fan, G., Liu, H., Liu, C., Li, T., Yan, C., and Guo, Z. An overview of metamaterials and their achievements in wireless power transfer. *J. Mater. Chem. C*, **6**, 2925 (2018). 10

[40] Shalaev, V.M., Cai, W., Chettiar, U.K., Yuan, H., Sarychev, A.K., Drachev, V.P., and Kildishev, A.V. Negative index of refraction in optical metamaterials. *Opt. Lett.*, **30**, 3356 (2005). 10

[41] Dolling, G., Enkrich, C., Wegener, M., Zhou, J.F., Soukoulis, C.M., and Linden, S. Cut-wire pairs and plate pairs as magnetic atoms for optical metamaterials. *Opt. Lett.*, **30**, 3198 (2005).

[42] Zhou, J., Zhang, L., Tuttle, G., Koschny, T., and Soukoulis, C.M. Negative index materials using simple short wire pairs. *Phys. Rev. B*, **73**, 041101 (2006). 10

[43] Zhang, S., Fan, W., Malloy, K.J., Brueck, S.R.J., Panoiu, N.C., and Osgood, R.M. Near-infrared double negative metamaterials. *Opt. Express*, **13**, 4922 (2005). 10, 106

[44] Dolling, G., Wegener, M., Soukoulis, C.M., and Linden, S. Negative-index metamaterial at 780 nm wavelength. *Opt. Lett.*, **32**, 53 (2007). 106

[45] Kafesaki, M., Tsiapa, I., Katsarakis, N., Koschny, T., Soukoulis, C.M., and Economou, E.N. Left-handed metamaterials: The fishnet structure and its variations. *Phys. Rev. B*, **75**, 235114 (2007).

[46] Alici, K.B. and Ozbay, E. A planar metamaterial: Polarization independent fishnet structure. *Photonics and Nanostructures - Fundamentals and Applications*, **6**, 102 (2008).

[47] Zhang, S., Fan, W., Panoiu, N.C., Malloy, K.J., Osgood, R.M., and Brueck, S.R.J. Experimental demonstration of near-infrared negative-index metamaterials. *Phys. Rev. Lett.*, **95**, 137404 (2005). 106

[48] Beruete, M., Sorolla, M., and Campillo, I. Left-handed extraordinary optical transmission through a photonic crystal of subwavelength hole arrays. *Opt. Express*, **14**, 5445 (2006). 10, 106, 110

[49] Zhou, J., Koschny, T., Zhang, L., Tuttle, G., and Soukoulis, C.M. Experimental demonstration of negative index of refraction. *Applied Physics Letters*, **88**, 221103 (2006). 10

[50] Tretyakov, S.A., Simovski, C.R., and Hudlička, M. Bianisotropic route to the realization and matching of backward-wave metamaterial slabs. *Phys. Rev. B*, **75**, 153104 (2007). 10

[51] Boardman, A.D., King, N., and Velasco, L. Negative refraction in perspective. *Electromagnetics*, **25**, 365 (2005). 10

[52] Ramakrishna, S.A. Physics of negative refractive index materials. *Reports on Progress in Physics*, **68**, 449 (2005).

[53] Lapine, M. and Tretyakov, S. Contemporary notes on metamaterials. *IET Microwaves, Antennas Propagation*, **1**, 3 (2007).

[54] Shamonina, E. Slow waves in magnetic metamaterials: history, fundamentals and applications. *Physica Status Solidi (b)*, **245**, 1471 (2008). 29

[55] Meinzer, N., Barnes, W.L., and Hooper, I.R. Plasmonic meta-atoms and metasurfaces. *Nat. Photon.*, **8**, 889 (2014).

[56] Glybovski, S.B., Tretyakov, S.A., Belov, P.A., Kivshar, Y.S., and Simovski, C.R. Metasurfaces: From microwaves to visible. *Physics Reports*, **634**, 1 (2016). 10

[57] Gay-Balmaz, P. and Martin, O. Electromagnetic resonances in individual and coupled split-ring resonators. *J. Appl. Phys.*, **92**, 2929 (2002). 10, 23, 63, 64

[58] Marqués, R., Medina, F., and Rafii-El-Idrissi, R. Role of bianisotropy in negative permeability and left-handed metamaterials. *Phys. Rev. B*, **65**, 144440 (2002). vi, 11, 17, 18, 64

[59] Allen, J.E. and Segre, S.E. The electric field in single-turn and multi-sector coils. *Il Nuovo Cimento Series 10*, **21**, 980 (1961).

[60] Radkovskaya, A., Shamonin, M., Stevens, C.J., Faulkner, G., Edwards, D.J., Shamonina, E., and Solymar, L. Resonant frequencies of a combination of split rings: Experimental, analytical and numerical study. *Microw. Opt. Technol. Lett.*, **46**, 473 (2005).

[61] Zhou, J., Koschny, T., Kafesaki, M., Economou, E.N., Pendry, J.B., and Soukoulis, C.M. Saturation of the magnetic response of split-ring resonators at optical frequencies. *Phys. Rev. Lett.*, **95**, 223902 (2005). 14, 18

[62] Zhou, L. and Chui, S.T. Eigenmodes of metallic ring systems: A rigorous approach. *Phys. Rev. B*, **74**, 035419 (2006). 18, 85

[63] Du, J., Liu, S., Lin, Z., and Chui, S.T. Magnetic resonance of slotted circular cylinder resonators. *J. Appl. Phys.*, **104**, 014907 (2008). 14

[64] Zhou, L., Huang, X., Zhang, Y., and Chui, S.T. Resonance properties of metallic ring systems. *Mater. Today*, **12**, 52 (2009).

[65] Labidi, M., Tahar, J.B., and Choubani, F. A new proposed analytical model of circular split ring resonator. *J. Mater. Sci. Eng. B*, **1**, 696 (2011). 14

[66] Roglá, L.J., Carbonell, J., and Boria, V.E. Study of equivalent circuits for open-ring and split-ring resonators in coplanar waveguide technology. *IET Microw. Antennas Propag.*, **1**, 170 (2007).

[67] Sydoruk, O., Tatartschuk, E., Shamonina, E., and Solymar, L. Analytical formulation for the resonant frequency of split rings. *J. Appl. Phys.*, **105**, 014903 (2009). v, 11, 13, 14

[68] Solymar, L. *Waves in Metamaterials*. Oxford University Press, Oxford (2008). 11, 64

[69] Grover, F.W. Inductance Calculations: Working Formulas and Tables. *Instrument Society of America, Research Triangle Park, NC* (1981). 13

[70] Aydin, K., Bulu, I., Guven, K., Kafesaki, M., Soukoulis, C.M., and Ozbay, E. Investigation of magnetic resonances for different split-ring resonator parameters and designs. *New Journal of Physics*, **7**, 168 (2005). 14

[71] Powell, D.A., Lapine, M., Gorkunov, M.V., Shadrivov, I.V., and Kivshar, Y.S. Metamaterial tuning by manipulation of near-field interaction. *Phys. Rev. B*, **82**, 155128 (2010). v, 14, 15, 26, 57, 60, 61, 63, 64, 74

[72] Tatartschuk, E., Gneiding, N., Hesmer, F., Radkovskaya, A., and Shamonina, E. Mapping inter-element coupling in metamaterials: Scaling down to infrared. *Journal of Applied Physics*, **111**, 094904 (2012). 15

[73] Shamonin, M., Shamonina, E., Kalinin, V., and Solymar, L. Resonant frequencies of a splitring resonator: Analytical solutions and numerical simulations. *Microwave and Optical Technology Letters*, **44**, 133 (2005). vi, 16

[74] Baena, J.D., Bonache, J., Martín, F., Sillero, R.M., Falcone, F., Lopetegi, T., Laso, M.A.G., García-García, J., Gil, I., Portillo, M.F., and Sorolla, M. Equivalent-circuit models for split-ring resonators and complementary split-ring resonators coupled to planar transmission lines. *IEEE Transactions on Microwave Theory and Techniques*, **53**, 1451 (2005). vi, 16, 19, 20, 31, 41, 43, 67, 84, 86, 87

[75] Sauviac, B., Simovski, C.R., and Tretyakov, S.A. Double Split-Ring Resonators: Analytical Modeling and Numerical Simulations. *Electromagnetics*, **24**, 317 (2004). 16

[76] Lindell, I.V., Sihvola, A.H., Tretyakov, S.A., and Viitanen, A.J. *Electromagnetic Waves in Chrial and Bi-Isotropic Media*. Artech House, London (2002). 17

[77] Noginov, M. and Podolskiy, V. *Tutorials in Metamaterials*. CRC Press (2011). 17, 83

[78] Kriegler, C.., Rill, M.S., Linden, S., and Wegener, M. Bianisotropic photonic metamaterials. *IEEE Journal of Selected Topics in Quantum Electronics*, **16**, 367 (2010). 17, 83

[79] Marqués, R., Mesa, F., Martel, J., and Medina, F. Comparative analysis of edge- and broadside- coupled split ring resonators for metamaterial design - theory and experiments. *IEEE Transactions on Antennas and Propagation*, **51**, 2572 (2003). 18

[80] Katsarakis, N., Koschny, T., Kafesaki, M., Economou, E.N., and Soukoulis, C.M. Electric coupling to the magnetic resonance of split ring resonators. *Applied Physics Letters*, **84**, 2943 (2004). 18

[81] Smith, D.R., Gollub, J., Mock, J.J., Padilla, W.J., and Schurig, D. Calculation and measurement of bianisotropy in a split ring resonator metamaterial. *Journal of Applied Physics*, **100**, 024507 (2006).

[82] Zhou, L. and Chui, S.T. Magnetic resonances in metallic double split rings: Lower frequency limit and bianisotropy. *Applied Physics Letters*, **90**, 041903 (2007). 18

[83] Bulu, I., Caglayan, H., and Ozbay, E. Experimental demonstration of labyrinth-based left-handed metamaterials. *Opt. Express*, **13**, 10238 (2005). vi, 19

[84] Baena, J.D., Marqués, R., Medina, F., and Martel, J. Artificial magnetic metamaterial design by using spiral resonators. *Phys. Rev. B*, **69**, 014402 (2004). 19

[85] Liu, N. and Giessen, H. Coupling effects in optical metamaterials. *Angewandte Chemie International Edition*, **49**, 9838 (2010). 21, 71, 96

[86] Brongersma, M.L., Hartman, J.W., and Atwater, H.A. Electromagnetic energy transfer and switching in nanoparticle chain arrays below the diffraction limit. *Phys. Rev. B*, **62**, R16356 (2000). vi, 21, 22, 103, 104

[87] Weber, W.H. and Ford, G.W. Propagation of optical excitations by dipolar interactions in metal nanoparticle chains. *Phys. Rev. B*, **70**, 125429 (2004). 21, 103, 104

[88] Hesmer, F., Tatartschuk, E., Zhuromskyy, O., Radkovskaya, A.A., Shamonin, M., Hao, T., Stevens, C.J., Faulkner, G., Edwards, D.J., and Shamonina, E. Coupling mechanisms for split ring resonators: Theory and experiment. *Phys. Status Solidi B*, **244**, 1170 (2007). vi, 23, 24, 63, 64

[89] Liu, N., Kaiser, S., and Giessen, H. Magnetoinductive and electroinductive coupling in plasmonic metamaterial molecules. *Advanced Materials*, **20**, 4521 (2008). vi, 24, 25

[90] Feth, N., König, M., Husnik, M., Stannigel, K., Niegemann, J., Busch, K., Wegener, M., and Linden, S. Electromagnetic interaction of split-ring

resonators: The role of separation and relative orientation. *Opt. Express*, **18**, 6545 (2010). 25

[91] Liu, N., Liu, H., Zhu, S., and Giessen, H. Stereometamaterials. *Nat. Photon.*, **3**, 157 (2009). vi, 25, 26

[92] Powell, D.A., Hannam, K., Shadrivov, I.V., and Kivshar, Y.S. Near-field interaction of twisted split-ring resonators. *Phys. Rev. B*, **83**, 235420 (2011). 26

[93] Tang, C., Wang, Q., Liu, F., Chen, Z., and Wang, Z. Optical forces in twisted split-ring-resonator dimer stereometamaterials. *Opt. Express*, **21**, 11783 (2013). 26, 63, 64

[94] Wiltshire, M.C.K., Shamonina, E., Young, I.R., and Solymar, L. Dispersion characteristics of magneto-inductive waves: comparison between theory and experiment. *Electronics Letters*, **39**, 215 (2003). 27

[95] Shamonina, E. and Solymar, L. Magneto-inductive waves supported by metamaterial elements: components for a one-dimensional waveguide. *Journal of Physics D: Applied Physics*, **37**, 362 (2004). 27

[96] Syms, R.R., Shamonina, E., and Solymar, L. Positive and negative refraction of magnetoinductive waves in two dimensions. *The European Physical Journal B - Condensed Matter and Complex Systems*, **46**, 301 (2005). 28, 29

[97] Luo, C., Johnson, S.G., Joannopoulos, J.D., and Pendry, J.B. All-angle negative refraction without negative effective index. *Phys. Rev. B*, **65**, 201104 (2002). 29

[98] Beruete, M., Falcone, F., Freire, M.J., Marqués, R., and Baena, J.D. Electroinductive waves in chains of complementary metamaterial elements. *Applied Physics Letters*, **88**, 083503 (2006). vii, 29, 31, 32, 82

[99] Booker, H.G. Slot aerials and their relation to complementary wire aerials (babinet's principle). *Electrical Engineers - Part IIIA: Radiolocation, Journal of the Institution of*, **93**, 620 (1946). 29

[100] Deschamps, G. Impedance properties of complementary multiterminal planar structures. *IRE Transactions on Antennas and Propagation*, **7**, 371 (1959).

[101] King, R. and Owyang, G.H. Complementarity in the study of transmission lines. *IRE Transactions on Microwave Theory and Techniques*, **8**, 172 (1960). 29

[102] Falcone, F., Lopetegi, T., Laso, M.A.G., Baena, J.D., Bonache, J., Beruete, M., Marqués, R., Martín, F., and Sorolla, M. Babinet principle applied to the design of metasurfaces and metamaterials. *Phys. Rev. Lett.*, **93**, 197401 (2004). 29, 30, 31, 82, 87

[103] Marqués, R., Martín, F., and Sorolla, M. *Metamaterials with Negative Parameters: Theory, Design, and Microwave Applications*. Wiley Publications (2013). 30, 87

[104] Getsinger, W.J. Circuit duals on planar transmission media. In *1983 IEEE MTT-S International Microwave Symposium Digest*, page 154 (1983). 31

[105] Beruete, M., Aznabet, M., Navarro-Cía, M., Mrabet, O.E., Falcone, F., Aknin, N., Essaaidi, M., and Sorolla, M. Electroinductive waves role in left-handed stacked complementary split rings resonators. *Opt. Express*, **17**, 1274 (2009). 32, 82, 96, 99, 100, 103

[106] Gil, I., Bonache, J., Gil, M., García-García, J., Martín, F., and Marqués, R. Accurate circuit analysis of resonant-type left handed transmission lines with inter-resonator coupling. *Journal of Applied Physics*, **100**, 074908 (2006). 32

[107] Gil, M., Bonache, J., Gil, I., García-García, J., and Martín, F. On the transmission properties of lefthanded microstrip lines implemented by complementary split rings resonators. *International Journal of Numerical Modelling: Electronic Networks, Devices and Fields*, **19**, 87 (2006).

[108] Gil, M., Bonache, J., Selga, J., García-García, J., and Martín, F. Broadband resonant-type metamaterial transmission lines. *IEEE Microwave and Wireless Components Letters*, **17**, 97 (2007). 32

[109] Navarro-Cía, M., Beruete, M., Agrafiotis, S., Falcone, F., Sorolla, M., and Maier, S.A. Broadband spoof plasmons and subwavelength electromagnetic energy confinement on ultrathin metafilms. *Opt. Express*, **17**, 18184 (2009). 32

[110] Navarro-Cía, M., Agrafiotis, S., Beruete, M., Falcone, F., Sorolla, M., and Maier, S.A. Planar metamaterial guiding from the perspective of geometrically induced surface plasmons. *Proceedings of the Fourth European Conference on Antennas and Propagation*, page 1 (2010). 32

[111] Navarro-Cía, M., Aznabet, M., Beruete, M., Falcone, F., El Mrabet, O., Sorolla, M., and Essaaidi, M. Stacked complementary metasurfaces for ultraslow microwave metamaterials. *Applied Physics Letters*, **96**, 164103 (2010). 33

[112] Anritsu Vector Network Analyzer - ms4644a data sheet. *Anritsu Corporation* (n.d.). 38

[113] Anritsu Vector Network Analyzer - Primer application note. *Anritsu Corporation* (n.d.). 39

[114] Anritsu LRL/LRM calibration - Theory and methodology. *Anritsu Corporation* (n.d.). 39

[115] Marqués, R., Martel, J., Mesa, F., and Medina, F. Left-handed-media simulation and transmission of EM waves in subwavelength split-ring-resonator-loaded metallic waveguides. *Phys. Rev. Lett.*, **89**, 183901 (2002). 41

[116] Burokur, S.N., Latrach, M., and Toutain, S. Analysis and design of waveguides loaded with split-ring resonators. *Journal of Electromagnetic Waves and Applications*, **19**, 1407 (2005).

[117] Belov, P.A. and Simovski, C.R. Sub-wavelength metallic waveguides loaded by uniaxial resonant scatterers. In *MELECON 2006 - 2006 IEEE Mediterranean Electrotechnical Conference*, page 229 (2006).

[118] Jitha, B., Nimisha, C.S., Aanandan, C.K., Mohanan, P., and Vasudevan, K. SRR loaded waveguide band rejection filter with adjustable bandwidth. *Microwave and Optical Technology Letters*, **48**, 1427 (2006). 41

[119] Srivastava, G.P. and Gupta, V.L. *Microwave Devices and Circuit Design.* PHI Learning Pvt. Ltd. (2006). 42, 43

[120] Jordan, E.P. and Balmain, K.G. *Electromagnetic Waves and Radiating Systems, second edition, page 130.* Prentice-Hall (1968). 47

[121] Parker, M. *Digital Signal Processing 101: Everything you need to know to get started.* Newnes (2010). 54

[122] Antoniou, A. *Digital Signal Processing.* McGraw-Hill Toronto, Canada (2006). 54

[123] Tatartschuk, E., Gneiding, N., Hesmer, F., Radkovskaya, A., and Shamonina, E. Mapping inter-element coupling in metamaterials: Scaling down to infrared. *J. Appl. Phys.*, **111**, 094904 (2012). 57, 60, 61

[124] Liu, M., Powell, D.A., Shadrivov, I.V., and Kivshar, Y.S. Optical activity and coupling in twisted dimer meta-atoms. *Appl. Phys. Lett.*, **100**, 111114 (2012). 60

[125] Pendry, J.B. Negative refraction makes a perfect lens. *Phys. Rev. Lett.*, **85**, 3966 (2000). 63

[126] Li, T.Q., Liu, H., Li, T., Wang, S.M., Cao, J.X., Zhu, Z.H., Dong, Z.G., Zhu, S.N., and Zhang, X. Suppression of radiation loss by hybridization effect in two coupled split-ring resonators. *Phys. Rev. B*, **80**, 115113 (2009). 63, 64

[127] Hein, S.M. and Giessen, H. Retardation-induced phase singularities in coupled plasmonic oscillators. *Phys. Rev. B*, **91**, 205402 (2015).

[128] Wu, P.C., Hsu, W., Chen, W.T., Huang, Y., Liao, C.Y., Liu, A.Q., Zheludev, N.I., Sun, G., and Tsai, D.P. Plasmon coupling in vertical split-ring resonator metamolecules. *Sci. Rep.*, **5**, 9726 (2015). 63, 64

[129] Shadrivov, I.V., Reznik, A.N., and Kivshar, Y.S. Magnetoinductive waves in arrays of split-ring resonators. *Physica B Condens. Matter*, **394**, 180 (2007). 63

[130] Radkovskaya, A., Sydoruk, O., Shamonin, M., Shamonina, E., Stevens, C.J., Faulkner, G., Edwards, D.J., and Solymar, L. Experimental study of a bi-periodic magnetoinductive waveguide: comparison with theory. *IET Microwaves, Antennas Propagation*, **1**, 80 (2007). 63

[131] Liu, H., Genov, D.A., Wu, D.M., Liu, Y.M., Liu, Z.W., Sun, C., Zhu, S.N., and Zhang, X. Magnetic plasmon hybridization and optical activity at optical frequencies in metallic nanostructures. *Phys. Rev. B*, **76**, 073101 (2007). 63

[132] Liu, N. and Giessen, H. Three-dimensional optical metamaterials as model systems for longitudinal and transverse magnetic coupling. *Opt. Express*, **16**, 21233 (2008).

[133] Sersic, I., Frimmer, M., Verhagen, E., and Koenderink, A.F. Electric and magnetic dipole coupling in near-infrared split-ring metamaterial arrays. *Phys. Rev. Lett.*, **103**, 213902 (2009).

[134] Lapine, M., Powell, D., Gorkunov, M., Shadrivov, I., Marqués, R., and Kivshar, Y. Structural tunability in metamaterials. *Appl. Phys. Lett.*, **95**, 084105 (2009).

[135] Decker, M., Linden, S., and Wegener, M. Coupling effects in low-symmetry planar split-ring resonator arrays. *Opt. Lett.*, **34**, 1579 (2009). 63

[136] Zhang, F., Zhao, Q., Sun, J., Zhou, J., and Lippens, D. Coupling effect of split ring resonator and its mirror image. *Progress in electromagnetics research*, **124**, 233 (2012). 68

[137] Shapiro, M.A., Trendafilov, S., Urzhumov, Y., Alù, A., Temkin, R.J., and Shvets, G. Active negative-index metamaterial powered by an electron beam. *Phys. Rev. B*, **86**, 085132 (2012). 82

[138] Prosvirnin, S. and Zouhdi, S. *Advances in Electromagnetics of Complex Media and Metamaterials*. Springer (2000). 84, 85

[139] Debus, C. and Bolivar, P.H. Frequency selective surfaces for high sensitivity terahertz sensing. *Applied Physics Letters*, **91**, 184102 (2007).

[140] Lahiri, B., Khokhar, A.Z., De La Rue, R.M., McMeekin, S.G., and Johnson, N.P. Asymmetric split ring resonators for optical sensing of organic materials. *Opt. Express*, **17**, 1107 (2009).

[141] Aydin, K., Pryce, I.M., and Atwater, H. Symmetry breaking and strong coupling in planar optical metamaterials. *Optics express*, **18**, 13407 (2010).

[142] Lahiri, B., McMeekin, S.G., De La Rue, R.M., and Johnson, N.P. Enhanced fano resonance of organic material films deposited on arrays of asymmetric split-ring resonators (A-SRRs). *Opt. Express*, **21**, 9343 (2013).

[143] Fedotov, V.A., Rose, M., Prosvirnin, S.L., Papasimakis, N., and Zheludev, N.I. Sharp trapped-mode resonances in planar metamaterials with a broken structural symmetry. *Phys. Rev. Lett.*, **99**, 147401 (2007).

[144] Papasimakis, N., Fedotov, V.A., Fu, Y.H., Tsai, D.P., and Zheludev, N.I. Coherent and incoherent metamaterials and order-disorder transitions. *Phys. Rev. B*, **80**, 041102 (2009).

[145] Fedotov, V.A., Papasimakis, N., Plum, E., Bitzer, A., Walther, M., Kuo, P., Tsai, D.P., and Zheludev, N.I. Spectral collapse in ensembles of metamolecules. *Phys. Rev. Lett.*, **104**, 223901 (2010). 84, 85

[146] Naqui, J. *Symmetry Properties in Transmission Lines Loaded with Electrically Small Resonators*. Ph.D. thesis, Universitat Autònòma de Barcelona (2014). 87

[147] Syms, R.R.A., Solymar, L., Young, I.R., and Floume, T. Thin-film magneto-inductive cables. *Journal of Physics D: Applied Physics*, **43**, 055102 (2010). 94

[148] Stevens, C.J., Li, Y., and Chan, C.W. Forward magneto-inductive wave propagation in planar magnetically coupled capacitor grids. *Journal of Electromagnetic Waves and Applications*, **29**, 753 (2015). 94

[149] Beruete, M., Sorolla, M., and Campillo, I. Left-handed extraordinary optical transmission through a photonic crystal of subwavelength hole arrays. *Opt. Express*, **14**, 5445 (2006). 106, 107

[150] Beruete, M., Campillo, I., Navarro-Cía, M., Falcone, F., and Sorolla, M. Molding left- or right-handed metamaterials by stacked cutoff metallic hole arrays. *IEEE Transactions on Antennas and Propagation*, **55**, 1514 (2007). 106

[151] Beruete, M., Sorolla, M., and Campillo, I. Inhibiting left-handed wave propagation by a band gap of stacked cut-off metallic hole arrays. *IEEE Microwave and Wireless Components Letters*, **17**, 16 (2007). 106, 107

[152] Beruete, M., Navarro-Cía, M., Sorolla, M., and Campillo, I. Polarization selection with stacked hole array metamaterial. *Journal of Applied Physics*, **103**, 053102 (2008). 118

[153] Navarro-Cía, M., Beruete, M., Falcone, F., Sorolla, M., and Campillo, I. Polarization-tunable negative or positive refraction in self-complementariness-based extraordinary transmission prism. *Progress In Electromagnetics Research*, **103**, 101 (2010).

[154] Beruete, M., Navarro-Cía, M., Falcone, F., Campillo, I., and Sorolla, M. Single negative birefringence in stacked spoof plasmon metasurfaces by prism experiment. *Optics Letters*, **35**, 643 (2010). 118

[155] Pöschl, G. and Teller, E. Bemerkungen zur quantenmechanik des anharmonischen oszillators. *Zeitschrift für Physik*, **83**, 143 (1933). 128

[156] Lekner, J. Reflectionless eigenstates of the sech2 potential. *American Journal of Physics*, **75**, 1151 (2007). 128